EFFECTS OF FORWARD- AND BACKWARD-FACING STEPS ON BOUNDARY-LAYER TRANSITION AT MACH 6

by

Christopher Yam

A Thesis

Submitted to the Faculty of Purdue University

In Partial Fulfillment of the Requirements for the degree of

Master of Science in Aeronautics and Astronautics

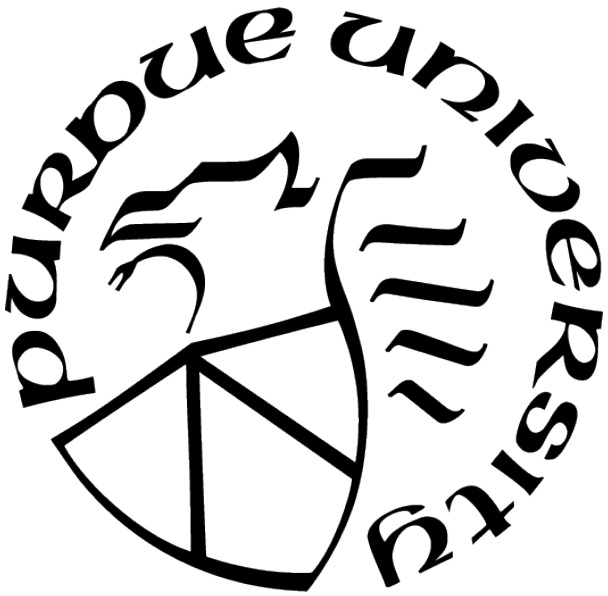

School of Aeronautics and Astronautics

West Lafayette, Indiana

May 2022

THE PURDUE UNIVERSITY GRADUATE SCHOOL
STATEMENT OF COMMITTEE APPROVAL

Dr. Steven P. Schneider, Co-Chair

School of Aeronautics and Astronautics

Dr. Joseph S. Jewell, Co-Chair

School of Aeronautics and Astronautics

Dr. Bradley M. Wheaton

Johns Hopkins University Applied Physics Laboratory

Approved by:

Dr. Gregory A. Blaisdell

To Alyson, Mom, Dad, and Luna

ACKNOWLEDGMENTS

I would like to firstly acknowledge and thank Dr. Steven Schneider for his guidance, support, and effort on this research. I would also like to thank Dr. Joseph Jewell and Dr. Brad Wheaton for their help and advice as members on the committee. Thank you to the entire BOLT team for sharing their work. Funding for this project was provided by the Air Force Office of Scientific Research under grant FA-9550-17-1-0149.

The machinists in ASL were instrumental in fabrication of parts for this research. Thank you to Jerry Hahn, Robin Snodgrass, and Jim Younts for providing advice and building additional inserts that were used in this experiment. I'd also like to thank John Phillips for his support on electrical issues that arose in the facility.

Lastly, I'd like to thank all the past and current lab members of the BAM6QT: Brandon Chynoweth, Liz Benitez, Greg McKiernan, Drew Turbeville, Josh Edelman, Katie Gray, Carson Lay, Phil Portoni, Varun Viswanathan, Mark Noftz, Lauren Wagner, Derek Mamrol, Sam Overpeck, Nate Lavery, Zachary McDaniel, Bethany Price, Sam Miller, and Cassandra Butler. Your help and support have gone a long way to the completion of this work.

TABLE OF CONTENTS

LIST OF TABLES

LIST OF FIGURES

LIST OF SYMBOLS

α	Angle of Attack
β	Yaw Angle
k	Step Height
p_0	Stagnation Pressure in freestream
$p_{0,init}$	Initial stagnation pressure before a run
T_0	Stagnation Temperature in freestream
$T_{0,init}$	Initial stagnation temperature before a run
T_w	Model wall temperature
$T_{w,init}$	Model wall temperature before a run
Q	Heat Flux
Re	Reynolds Number per unit length in freestream
Re_m	Freestream Unit Reynolds Number (per meter)
St	Stanton Number
X	Streamwise distance from the model nosetip
L	Model length
X/L	Nondimensional distance from the model nosetip
M	Mach Number
c_p	Specific heat capacity
δ	Boundary-layer thickness, defined as 99.5% of the freestream enthalpy
γ	Ratio of Specific Heats
ρ	Density
μ	Dynamic Viscosity in freestream

ABBREVIATIONS

ACE	Texas A&M Mach-6 Actively Controlled Expansion Tunnel
AFOSR	Air Force Office of Scientific Research
ASL	Aerospace Sciences Laboratory
BAM6QT	Boeing / AFOSR Mach-6 Quiet Tunnel
BOLT	Boundary Layer Transition Flight Experiment
CaF_2	Calcium Fluoride
CMM	Coordinate Measurement Machine
CFD	Computational Fluid Dynamics
DAQ	Data Acquisition System
DNS	Direct Numerical Simulation
IR	Infrared
JHU / APL	Johns Hopkins University Applied Physics Laboratory
PSE	Parabolised Stability Equations
LE	Leading Edge
LPSE	Linearized Parabolised Stability Equations
LST	Linear Stability Theory
M6QT	Texas A&M Mach-6 Quiet Tunnel
NASA	National Aeronautics and Space Administration
PEEK	Polyether ether ketone
PIRANHA	Purdue Infrared Registration ANd Heat transfer App
PSD	Power Spectral Density
RMS	Root-Mean-Square
STABL	Stability and Transition Analysis for Hypersonic Boundary Layers
TAMU	Texas A&M University
TM	Taylor-Maccoll
TW	Tangent-Wedge
TPS	Thermal Protection System
TSP	Temperature Sensitive Paint

ABSTRACT

Wind-tunnel experiments with a sharp 7-degree half-angle cone and a 33% scale Boundary Layer Transition (BOLT) model were performed in the Boeing/AFOSR Mach 6 Quiet Tunnel to investigate the effects of forward- and backward-facing steps on boundary-layer instability and transition. Each model was modified to include intentional steps just downstream of the nosetip. Experiments were performed at different freestream Reynolds numbers and varying step sizes. Infrared thermography was used to calculate surface heat transfer, and high-frequency pressure sensors were used to measure pressure fluctuations. A replica measurement technique was used to accurately measure step heights on the BOLT flight vehicle and the wind tunnel model.

A 7-degree half-angle cone was tested at 0-degree and 6-degree angles of attack. Step heights ranged from 0.610 mm to 1.219 mm. At a 0-degree angle of attack, no significant increases in heat transfer were observed with any of the forward- or backward-facing steps. However, a 250 kHz instability was measured with the forward-facing steps. Growth of the instability was similar to a second-mode. At a 6-degree angle of attack, an increase in heat transfer was observed on the windward ray with the forward-facing steps. Sharp increases in heating rates and increased pressure fluctuations were indications of boundary-layer transition. Elevated heating rates and pressure fluctuations were not measured with the backward-facing steps.

The BOLT model was tested at 0-degree, 2-degree, and 4-degree angles of attack and 2-degree and 4-degree yaw angles. Step heights ranged from 0.076 mm to 1.016 mm. At a 0-degree angle of attack and 0-degree yaw angle, thin wedges of heating were observed with the backward-facing steps. Instabilities were measured near these wedges of heating and are thought to be caused by a secondary instability. The effects of the steps were magnified on the windward side of the BOLT model at angles of attack. Wedges of heating were wider and more intense. At higher angles of attack, the onset of heating was further upstream. Sensors near and directly underneath the wedges of heating measured pressure fluctuations that were indicative of a turbulent flow. Wedges of heating were also observed at a 4-degree yaw angle, but only with the 1.016 mm backward-facing step.

1. INTRODUCTION AND BACKGROUND

1.1 Hypersonic Laminar-Turbulent Transition

The state of the boundary layer is an important aerodynamic characteristic to consider when designing a hypersonic vehicle. A laminar boundary layer generates a low amount of skin friction but is prone to separation. Conversely, a turbulent boundary layer generates a higher amount of skin friction, drag, and surface heating due to increased vorticity and mixing near the wall. At hypersonic speeds, a turbulent boundary layer can introduce heating rates that are 3 times or greater when compared to a laminar one [1]. This increase in heating was demonstrated in the Reentry F flight experiment, shown in Figure 1.1. At the front of the vehicle between x/L = 0.0 and 0.5, a relatively low heating rate was measured where the boundary layer was laminar. Between x/L = 0.6 and 0.8, a sharp increase in heating rates was measured. This represents the onset of transition to a turbulent boundary layer. The increased heating rates can cause damage to a vehicle if not designed with an adequate thermal protection system. Because of this, it is important to accurately predict the boundary-layer state on a hypersonic vehicle if it will be traveling at these speeds for an extended duration.

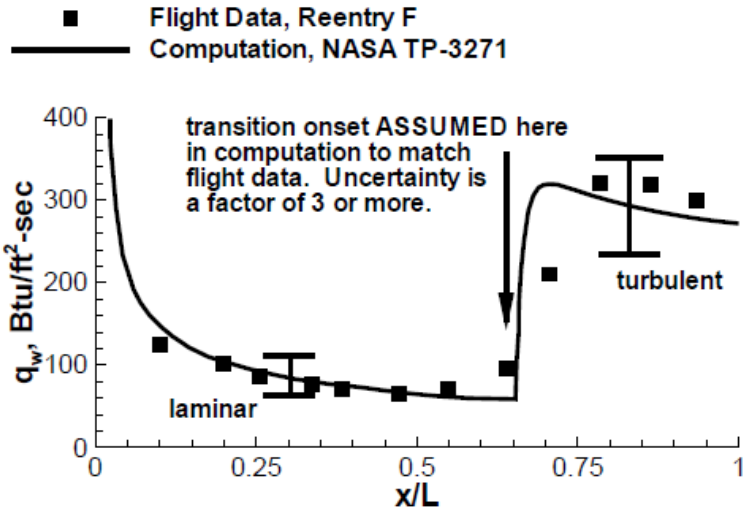

Figure 1.1. Heating-rate distribution along cone from the Reentry F flight showing the increase in heating due to laminar-turbulent transition. Taken from Figure 2 of [1] which was adapted from Figure 8 of [2].

The transition process begins when a disturbance enters the boundary layer. Many factors can introduce significant disturbances into the flow, such a surface roughness or acoustic noise in the freestream. The disturbances can induce instabilities in the boundary layer, which grow and eventually break down into turbulence. Instabilities in the boundary layer have been identified, classified, and studied extensively at low and supersonic speeds. Studying these instabilities at hypersonic speeds is more challenging.

An accurate and cost-effective method to predict transition is sought for use in engineering-level design. Computational tools such as direct numerical simulation (DNS) and parabolized stability equations (PSE) can be used to simulate the physical growth of instabilities but are computationally expensive. The e^N method is a semi-empirical relationship that uses linear stability theory (LST) to predict transition. The N factor represents the amplitude ratio of an instability and is used to predict the linear growth rate of the instability. This method is still commonly used today. Reed et al. provides a review of linear stability theory and its use in different speed regimes [3]. At hypersonic speeds ($M > 5$), the second (Mack) mode instability has been found to be the dominant instability. The instability is tuned to the boundary-layer thickness and is often described as an acoustic wave that reflects between the wall and the sonic line of the boundary layer [4]. The relation between the dominant frequency of the second-mode instability and the boundary-layer thickness have been demonstrated in many experiments, such as those performed by Estorf et al. [5]. Good agreement is seen between the e^N method and wind-tunnel measurements of the second mode instability.

Many limitations exist when using the e^N method to predict transition. The method does not consider the effect of surface roughness, freestream noise, or non-linear growth. At a sufficiently high amplitudes, secondary instabilities arise and are three-dimensional and non-linear in nature. Herbert provides a review of secondary instability in Reference [6]. These instabilities can form in the shear layer of a three-dimensional flow structure and may have a significant contribution to the breakdown of the boundary layer. Data from experimental tests can be used to better understand the growth and breakdown of instabilities. This information can also help develop existing and newer methods to predicting transition.

1.2 Effects of Steps on Laminar-Turbulent Transition

A step can form between two surfaces due to an assembly tolerance or to a thermal-differential expansion between two parts. If the step is large enough, the disturbances introduced into the boundary layer can cause an early onset of transition. Protrusions in the flow have been shown to introduce disturbances and instabilities into the flow. However, the exact mechanisms that cause the disturbances are not well understood. Wheaton et al. tested a 10.2 mm cylindrical protrusion in a Mach-6 flow and measured the perturbations in the wake [7]. An instability with a frequency peak near 21 kHz was measured in the wake of the protrusion. Computations with the protrusion in the flow detected a similar 18 kHz instability. It was thought that the instability occurred in the shear layer of the wake. However, it is also possible that a protrusion in the flow would interact with and modulate an existing instability mechanism, such as a crossflow-type or a second-mode instability. A review and discussion of the physical interaction between different types of surface roughness and the boundary layer can be found in [8].

1.3 Boundary Layer Transition Flight Experiment (BOLT)

The purpose of the Boundary Layer Transition (BOLT) Flight Experiment was to study and better understand the transition mechanisms that occur on highly 3-D geometries. An image of the instrumented flight vehicle is shown in Figure 1.2. The geometry features a cylindrical nosetip that transforms into four swept leading edges that extend to the back of the geometry. Two concave experiment surfaces are the primary regions of interest. To isolate the flow between them, concave gutters on either side of the geometry entrain the flow. Detailed overviews of the flight vehicle and its intended flight conditions are provided in [9] and [10]. The vehicle was instrumented with 140 Medtherm thermocouples to enable heat-transfer calculations. Surface-mounted pressure sensors were also installed to detect boundary-layer transition and measure instabilities. Computations and wind tunnel experiments were performed as part of a pre-flight test campaign. These analyses would assist with the interpretation of flight data, and also to better understand the flow characteristics and transition mechanisms that would occur during the flight. The flight was launched in June

2021 but encountered an unexpected aerodynamic coning motion at relatively high angles of attack. This prevented the vehicle from reaching its intended Mach 5 to 7 flight condition [11]. Data from the flight experiment are currently being analyzed and are to be published in 2022.

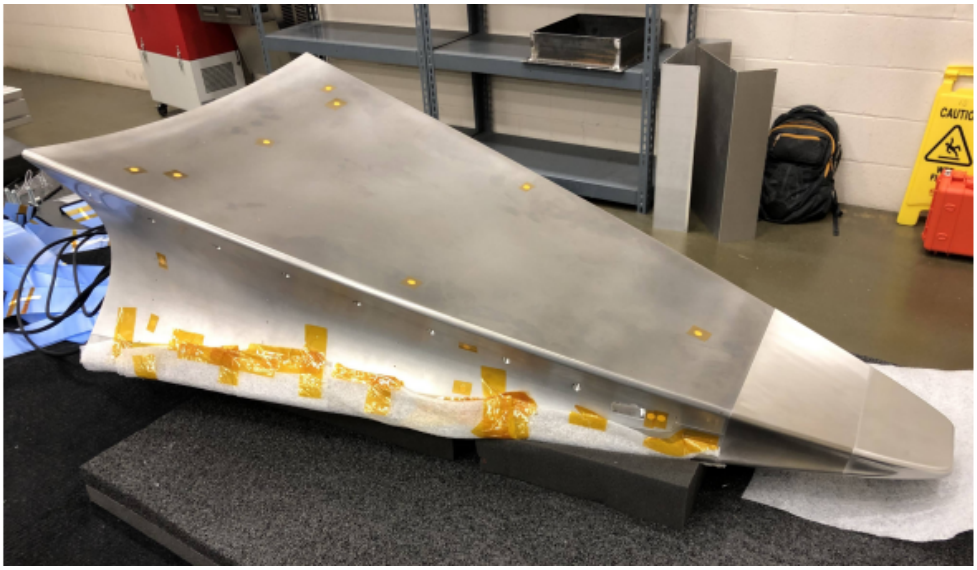

Figure 1.2. Final assembly of the BOLT Flight Geometry. Taken from Figure 13b of [10].

The BOLT flight geometry was comprised of three parts: the nosetip, isolator, and frustum. Each part was fabricated from a different material, and a thermal differential expansion between them was expected during the flight. Because of this, steps were expected to form at the joints between the parts. A nominally-smooth wall was desired during the latter part of the descent trajectory. To achieve this, backward-facing steps were designed into the geometry. This design choice resulted in a backward-facing step during the ascent trajectory, which could result in an early onset of transition. To further study the effect of these steps, the secondary side of the vehicle was designed with step heights that were three times as large. A discussion of the sizing of these steps and potential effects on the flow can be found in [12].

1.3.1 BOLT Computations

Computations on the BOLT geometry were performed to gain a better understanding of the flowfield and also to demonstrate the ability of computations to predict flow characteristics on a highly 3-D geometry. The steady flow properties, such as heat flux and mean surface pressure, can be compared to measurements from wind-tunnel tests and to the measurements from the flight experiment. Boundary-layer instabilities can also be computed and compared to the wind-tunnel and flight data, however this is still an active area of research. A comparison to the wind tunnel experiments and the flight data can validate and further develop the computational tools.

Li et al. performed computations on the BOLT flight geometry and a 33% scale BOLT model [13]. The mean flow was computed with VULCAN, and then a DNS-WENO code was used to analyze instabilities in the boundary layer. Four unstable modes were identified near the centerline of the experiment surface. Three of the unstable modes were classified as shear layer modes and were concentrated within a vortex-like structure. On the 33% scale BOLT model, the peak frequencies of the shear layer modes were between 30 kHz and 150 kHz. The most prominent instability, Mode Family I, grew along a vortex-like structure in the streamwise direction. Similar unstable modes were also identified on the flight geometry. However, the peak frequencies of the modes were much higher due to the higher freestream Reynolds numbers along the intended flight trajectory.

Thome et al. also performed steady and unsteady computations on a 33% scale BOLT model using DNS [14]. Vortex-like structures near the centerline were identified in the steady computations and are in good agreement with the computations by Li et al. Velocity perturbations in the unsteady computation were identified near the vortex-like structures. The frequencies of the perturbations were between 37 kHz and 47 kHz. A second-mode instability was also identified in the unsteady computation. The most amplified second-mode frequencies were between 300 kHz and 400 kHz and were located between 20 mm and 50 mm from the centerline. The second-mode frequencies are dependent on the boundary-layer thickness, which increased in the streamwise direction and varied in the spanwise direction.

Mullen et al. performed stability computations on a 33% scale BOLT model using a linear PSE (LPSE) analysis [15]. The mean flow was computed using DPLR. The vortical structures near the centerline of the geometry were identified. Inviscid streamlines were extracted from the mean flow and analyzed using LPSE to identify instabilities. A second-mode instability was identified between the centerline and the leading edge. However, the amplification rates were low and were not expected to be measured in wind tunnel experiments. The most-amplified region of the instability was located in a small wedge-like region at the aft end of the model, approximately 50 mm from the centerline. Stationary and traveling crossflow instabilities were also identified in the LPSE analysis. The crossflow-type instabilities were most amplified near the centerline.

1.3.2 BOLT Wind Tunnel Experiments

Several wind tunnel experiments have been performed in different hypersonic facilities to support the flight campaign. Data from the experiments were also compared with the computations. Surface heat transfer was used to compare with the mean flow computations. Various instability measurements from high-frequency sensors were used to measure instabilities and compared with the stability analyses.

Kostak et al. demonstrated the effects of freestream acoustic noise on the 33% scale BOLT model [16] [17]. Experiments were performed at Texas A&M University (TAMU) in the Mach-6 Actively Controlled Expansion (ACE) tunnel and the Mach-6 Quiet Tunnel (M6QT). The ACE tunnel is a conventional noise tunnel with approximate freestream noise levels of 1.5%, and the M6QT is a quiet facility with freestream noise levels that are less than 0.1% [18]. Surface heat transfer was computed from IR thermography measurements in both wind tunnels. A comparison of the surface heat transfer is shown in Figure 1.3, taken from Figures 10 and 11 of [17]. In the low-noise environment of the M6QT, a relatively low heating magnitude was measured near the centerline of the model. In Figure 1.3b, two streaks of heating near the centerline are thought to represent a laminar, vortical structure. These streaks were also measured in other quiet tunnel measurements such as in Figure 1.5a and in the present experiments. The outboard region of the BOLT model was outside the

quiet core of the M6QT, which contains a higher magnitude of disturbances [19]. This likely causes the increased heating that was observed along the outboard region of the model as the freestream Reynolds number increased. In the higher noise environment of the ACE, higher heating magnitudes were measured. The two wedges of heating on the surface of the model were likely representative of a turbulent boundary layer.

Pressure fluctuations were also measured in the TAMU experiments with surface-mounted Kulite sensors and a hot wire. A vortical structure was identified in the hot-wire measurements above the laminar streak approximately 9 mm from the centerline. This was similar to the mean-flow computations and suggests that the laminar streaks were the effect of a vortical structure. A 37 kHz instability was identified in the vortical structure near the centerline. A 35 kHz instability was also identified in the Kulite pressure fluctuations. The peak frequencies of the instability were in good agreement with computations of an unstable mode in the vortical structure.

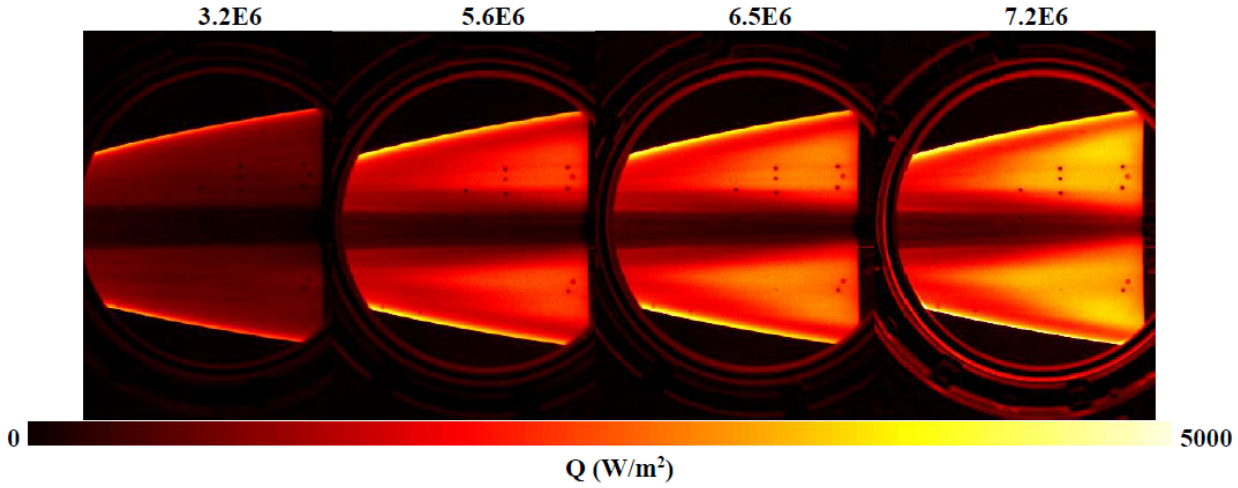

(a) Heat transfer images in the ACE wind tunnel.

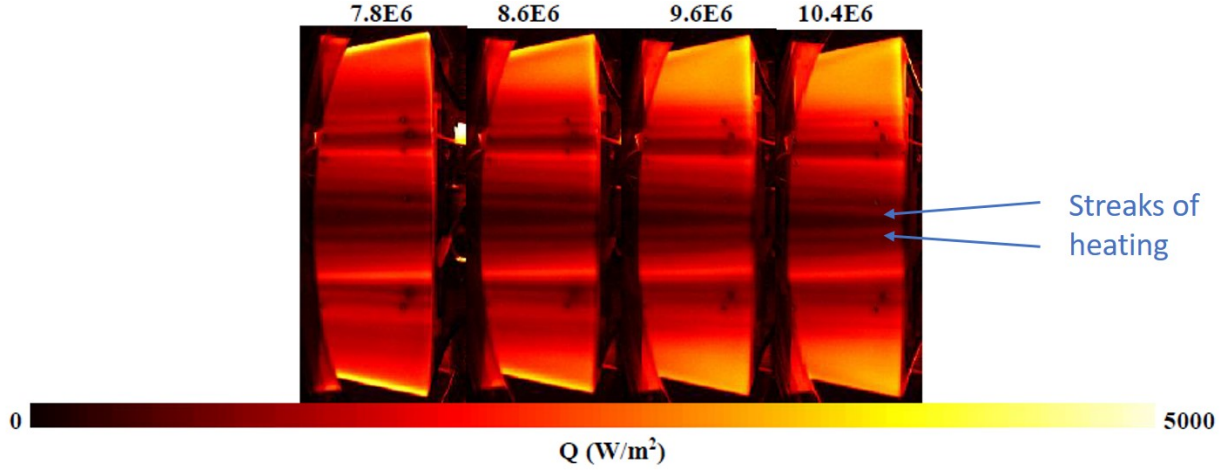

(b) Heat transfer images in the M6QT.

Figure 1.3. Images of heat transfer from Texas A&M University experiments, taken from Figures 10 and 11 of [17] with permission. The freestream Reynolds number per meter is labeled above each image.

Berry et al. demonstrated the effect of surface roughness by placing a strip of Kapton tape on the 33% scale BOLT model [20]. The experiments were performed in the NASA Langley 20-Inch Mach-6 Air Tunnel. Freestream noise levels in the facility were between 1% and 1.5% [21]. The Kapton tape was placed 60.7 mm downstream of the nosetip to emulate the position of the isolator-frustum joint on the flight vehicle. The largest tape height was 0.635 mm (0.025 in.). IR thermography measurements of the BOLT model with and without the Kapton tape installed at a freestream Reynolds number of 8.21×10^6 /m are taken from Figure 16 of [20] and shown in Figure 1.4. Without any tape, two wedges were observed in the IR thermography. The wedges are qualitatively similar to the results in the TAMU ACE tunnel and are likely the effect of a noisy freestream flow. The streaks of heating are less visible in Figure 1.4a when compared to the M6QT measurements, also due to the higher freestream noise of the Langley Mach-6 facility. With the Kapton tape installed, two streaks of heating were observed. The streaks emanate from the intersection between the tape and the leading edge.

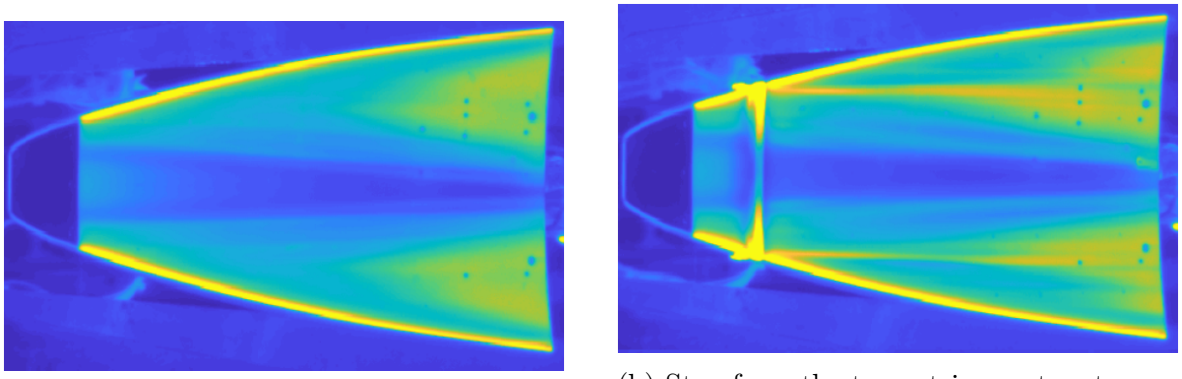

(a) Two wedges were observed in the surface heating with no step.

(b) Step from the tape strip creates streamwise streaks emanating from the leading edges.

Figure 1.4. IR images of the BOLT model with and without the 0.635 mm tape strip in the NASA Langley 20-inch Mach 6 Air Tunnel. Re = 8.21×10^6 /m. Taken from Figure 16 of [20] with permission.

Berridge et al. tested the 33% BOLT model in the Boeing / AFOSR Mach-6 Quiet Tunnel (BAM6QT), where freestream noise levels were below 0.05% [20] [22]. At a 0° angle of attack and at a freestream Reynolds number of 11.4×10^6 /m, many streaks were observed in the IR thermography measurements and were thought to represent x'laminar, vortical structures.

Examples of the laminar streaks are shown and identified in Figure 1.5a. Some Kulite sensors near the laminar streaks measured a 40 kHz instability, but some did not. IR thermography measurements and the power spectra of Kulite sensors near a laminar streak are taken from Figure 18 of [20] and shown in Figure 1.5. A clear relation between the laminar streak and the 40 kHz instability could not be established.

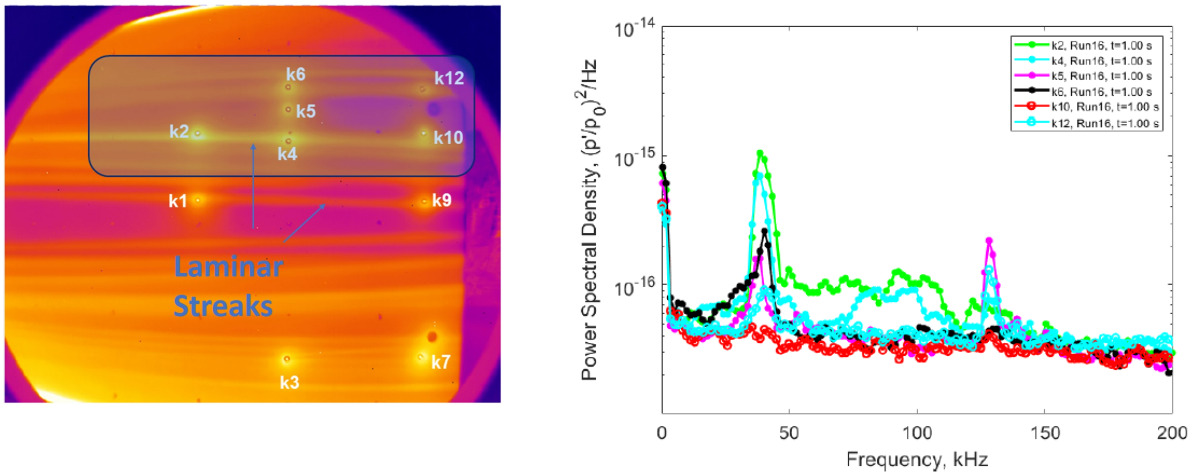

(a) IR image.

(b) Kulite PSD.

Figure 1.5. IR image and Kulite PSD of the 33% scale BOLT model in the BAM6QT at Re $= 11.4 \times 10^6$ /m. Taken from Figure 18 of [20] with permission.

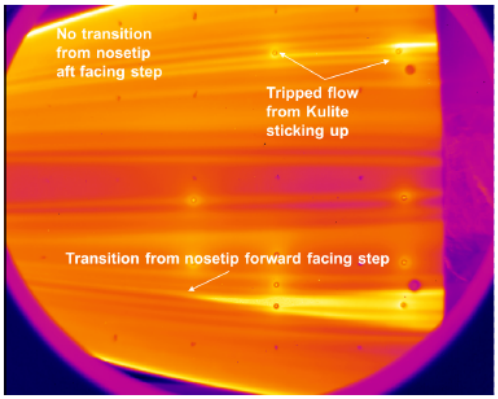

Figure 1.6. An asymmetric turbulent wedge was observed on the BOLT model at a 4° angle of attack in the BAM6QT. Re $= 11.5 \times 10^6$ /m. Taken from Figure 27 of [20] with permission.

When the model was pitched at a 4° angle of attack, an asymmetric wedge of heating was observed on the windward-facing surface. An IR thermography measurement at a freestream Reynolds number of 11.5 $\times$ 10^6 /m was taken from Figure 27 of [20] and shown in Figure 1.6. The wedge of heating was only observed on the port side of the experiment surface and did not appear to be tripped by a protruding sensor. It was unclear if the wedge was representative of natural transition or whether it was caused by an imperfection in the model geometry. Upon further inspection of the model, a 0.127 mm (0.005 in.) forward-facing step was measured on the port side of the model. The step was measured at the leading edge of the joint between the nosetip and the experiment surface. It was thought to be the cause of the asymmetric wedge of heating.

Chynoweth et al. performed follow-up experiments to investigate the effect of steps on the 33% BOLT model [23]. The experiments were also performed in the BAM6QT. Several new nosetips were fabricated with intentional forward- and backward-facing steps, with heights ranging from 0.076 mm (0.003 in.) to 0.508 mm (0.020 in.). A nominally-smooth nosetip was also fabricated for baseline measurements. Experiments were performed at a 0° and 4° angle of attack. IR measurements at angles of attack were obtained on the windward-facing experiment surface. At a 4° angle of attack and at a freestream Reynolds number of 11.3 $\times$ 10^6 /m, an asymmetric wedge of heating was observed on the port side of the experiment surface with the smooth-wall nosetip. The asymmetric wedge of heating was also observed on the port side with 0.076 mm, 0.152 mm, and 0.254 mm backward-facing steps. With the largest 0.508 mm backward-facing step, the wedge of heating appeared to flip to the starboard side of the experiment surface. IR thermography images with the 0.254 mm and 0.508 mm backward-facing steps were taken from Figures 14a and 14b of [23] and shown in Figure 1.7. The nosetips and model were inspected for potential causes of this asymmetry. Some uncertainty was attributed to the PEEK experiment surface, which was susceptible to warping after repeated use in the different wind tunnel experiments. Some uncertainty was also attributed to the flaws in the alignment of the nosetip, which could lead to inconsistencies in the step heights.

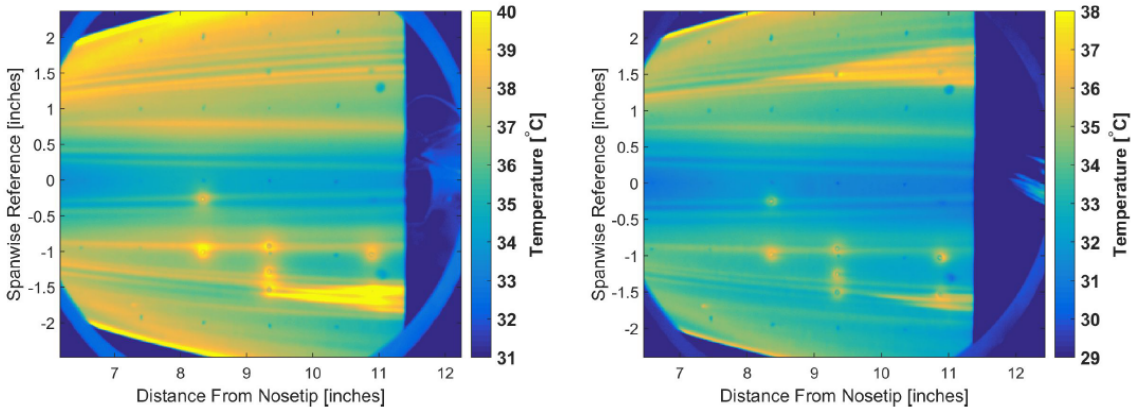

(a) 0.254 mm backward-facing step.

(b) 0.508 mm backward-facing step.

Figure 1.7. IR images with the 0.254 mm and 0.508 mm backward-facing steps installed. Re = 11.3×10^6 /m. Taken from Figure 14 of [23] with permission.

1.4 Scope of the Current Work

The present research was to continue the investigation of steps on the 33% scale BOLT model. The BOLT model was modified to address the asymmetries that were measured in previous work. The modifications would improve the alignment of the nosetips and better secure the nosetips to the rest of the model. Additionally, new nosetips with different-sized steps were fabricated to accompany the modified design. A comprehensive set of experiments was performed to identify the effects of the forward- and backward-facing steps. The BOLT model was tested at 0°, 2°, and 4° angles of attack and 2° and 4° yaw angles. Experiments were performed at a range of freestream Reynolds numbers to observe the development of any heating patterns and to detect the growth of any instabilities. Heat transfer was calculated from IR thermography measurements. The processed data are archived to enable comparisons to future computations or experiments.

2. TEST FACILITY, INSTRUMENTATION, AND DATA PROCESSING

2.1 Boeing / AFOSR Mach 6 Quiet Tunnel (BAM6QT)

The Boeing / AFOSR Mach-6 Quiet Tunnel (BAM6QT) resides at Purdue University. It is a Ludweig tube design. A long driver tube and test section are pressurized with filtered air, and the downstream dump tank is pulled to a near-vacuum pressure. The pressure difference between the two sections is held by two burst diaphragms. After the upstream section is filled to the desired pressure, the air is given 10 minutes to equilibrate. The diaphragms are burst to initiate the flow. The long converging-diverging nozzle accelerates the flow to Mach 6. A typical run lasts 3 to 5 seconds. A schematic of the wind tunnel is provided in Figure 2.1.

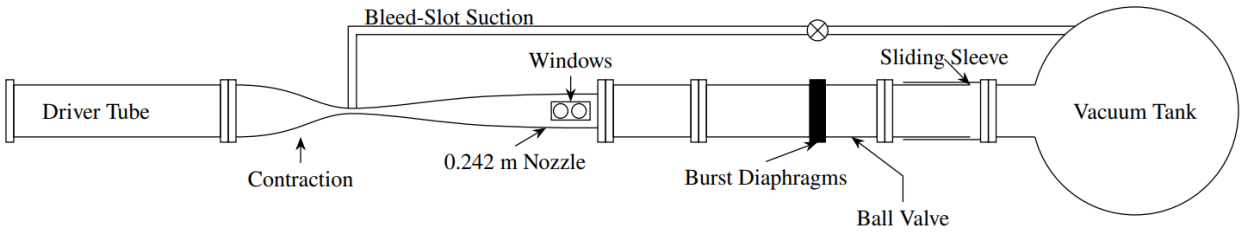

Figure 2.1. Boeing / AFOSR Mach 6 Quiet Tunnel (BAM6QT) schematic.

When the diaphragms are burst, an expansion wave travels upstream and through the nozzle. As the expansion wave passes through the throat, the Mach-6 flow starts. The expansion wave continues to travel upstream through the driver tube and reflects between the end of the driver tube and the throat. The reflections take about 200 ms to traverse the length of the driver tube and cause a slight drop in the stagnation pressure. Several features have been implemented in the BAM6QT to maintain a laminar nozzle-wall boundary layer. The throat and nozzle are polished to a mirror finish to reduce the effects of roughness-induced transition. The nozzle has a large radius of curvature to minimize the Görtler instability. A bleed slot located just upstream of the throat is connected to the vacuum tank and can remove the incoming boundary layer. This allows for a fresh boundary layer to develop at the beginning of the nozzle. When the bleed slot is activated, freestream noise

levels are less than 0.05% of the mean pitot pressure [24]. Without the bleed slot activated, freestream noise levels rise to about 1% to 2%. This is comparable to conventional hypersonic wind tunnels. The bleed slots can be used to study the effect of freestream noise levels. However, in the noisy flow configuration, the thicker boundary layer at the throat decreases the freestream Mach number to 5.8.

2.1.1 Determining Test Conditions

Before each run, the initial stagnation pressure ($p_{o,init}$) and stagnation temperature ($T_{o,init}$) are recorded. A Paroscientific Model 740 Digiquartz pressure sensor is used to measure the stagnation pressure just upstream of the burst diaphragms. A thermocouple is used to measure the stagnation temperature at the upstream end of the driver tube and typically measures some variation between runs. Air in the driver tube is heated to maintain a nominal stagnation temperature of 433 K. A 30 kW circulation heater heats the incoming air, and the driver tube is resistively heated with 2000 A. The heating system is not perfect and some run-to-run variation in the stagnation temperature is expected. The recorded stagnation temperature just before a run is typically between 423 K and 433 K. Turbeville tracked the recorded stagnation temperature over 892 runs and found a mean temperature of 427.7 K with a standard deviation of 2.7 K [25]. After the run is initiated, the stagnation pressure (p_o) is measured with a Kulite XTEL-190-500A pressure transducer located at the entrance to the contraction section. The stagnation pressure decreases in a stair-step pattern due to the reflecting expansion wave in the driver tube. As the expansion wave passes over the sensor face, the stagnation pressure drops by 1% to 2%. A plot of the stagnation pressure is shown in Figure 2.2, illustrating the stair-step pattern during a typical quiet-flow run.

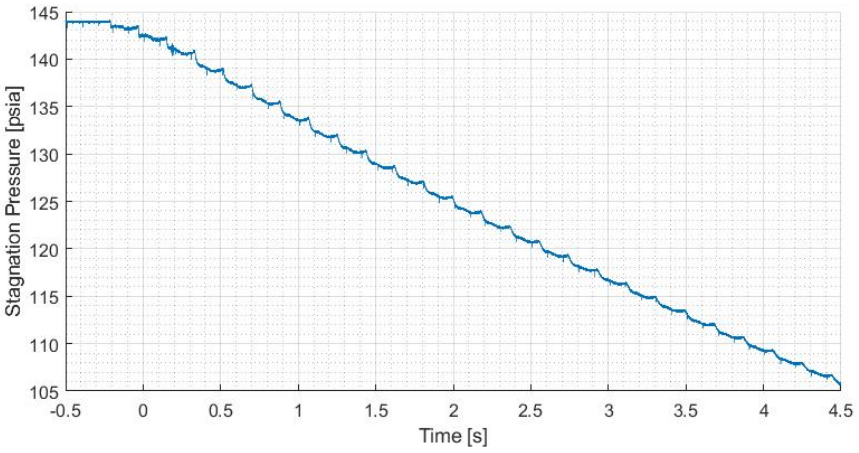

Figure 2.2. An example of the stagnation pressure during a typical quiet-flow run.

The stagnation temperature (T_o) during a run is calculated using the isentropic relation shown in Equation 2.1. The freestream static temperature and pressure are also calculated using isentropic flow relations, shown in Equations 2.2 and 2.3. The calculated freestream conditions are used to calculate the freestream Reynolds number per meter with Equation 2.4. Sutherland's Law is used to approximate the viscosity (μ).

$$T_0 = T_{0,init} \cdot (\frac{p_0}{p_{0,init}})^{\frac{\gamma-1}{\gamma}} \tag{2.1}$$

$$T = T_0 \cdot \frac{1}{1 + \frac{1}{2}(\gamma - 1)M^2} \tag{2.2}$$

$$p = p_0 \cdot [\frac{1}{1 + \frac{1}{2}(\gamma - 1)M^2}]^{\frac{\gamma}{\gamma-1}} \tag{2.3}$$

where γ is the ratio of specific heats.

$$Re_m = \frac{pM}{\mu} \cdot \sqrt{\frac{\gamma}{RT}} \tag{2.4}$$

where R is the individual gas constant.

A Kulite ETL-79-HA-DC-190 pressure transducer and a Dantec 55R45 hot-film are installed on the nozzle wall, just upstream of the nozzle exit. They are used to detect the

start of hypersonic flow and to determine if the flow is quiet or noisy. The Kulite ETL-79-HA-DC-190 has an operational pressure range between 0 to 5 psia and is mechanically stopped at 5 psia. When hypersonic flow is started, the freestream pressure drops sharply. A sharp decrease in the Kulite output signal is used as an indicator of the start of the run. The hot-film measures shear and heat transfer fluctuations on the tunnel wall, which are distinctively higher at tunnel start-up and also approximately 3 to 4 seconds into a run due to unstart. An example of the nozzle-wall Kulite and hot-film signals during a typical quiet-flow run are shown in Figure 2.3. The sharp decrease in the Kulite signal at t = 0 s indicates the start of the run. Large fluctuations in the hot film signal can be seen between 0 and 1 seconds into the run as the tunnel starts. After 1 second, the hot-film signal returns to a small fluctuation that is comparable to just before the run. This is an indication of started, quiet flow. After 3.5 seconds, the hot film measures increasingly larger fluctuations and indicates tunnel unstart.

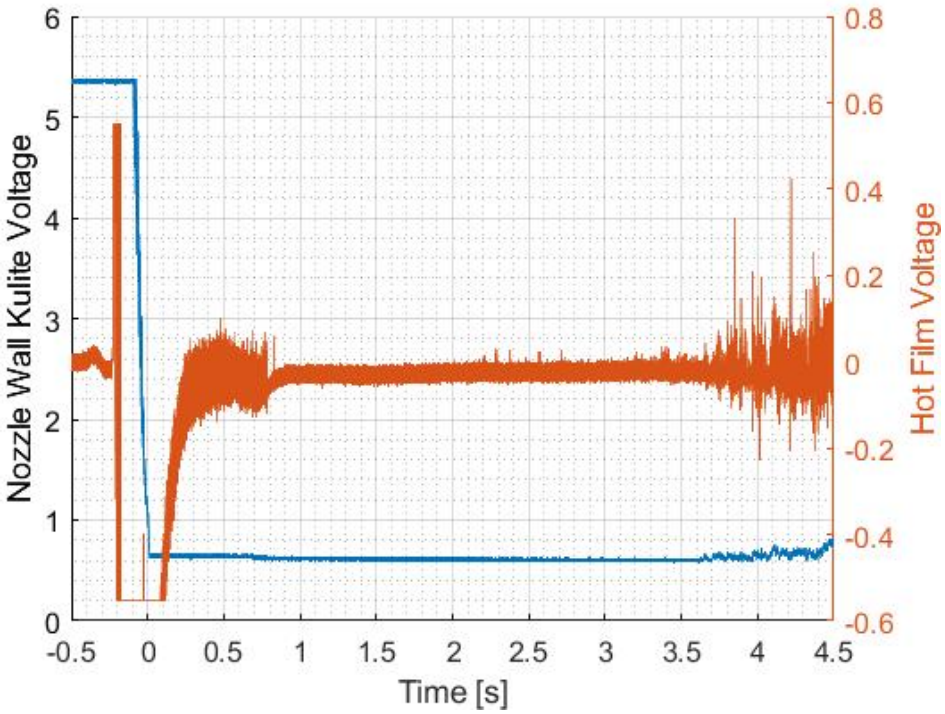

Figure 2.3. An example of the nozzle-wall Kulite and hot-film signals during a run.

2.2 Wind Tunnel Models

For the present work, two wind tunnel models were tested in the BAM6QT. The first was a sharp 7° half-angle cone, called the Modular Cone. The Modular Cone was used for preliminary experiments while the BOLT model was undergoing modification. The modular design and axisymmetric geometry allowed for rapid in-house modifications to incorporate steps into the model. The second was the 33% scale BOLT model. The majority of experiments and analysis were conducted with the 33% scale BOLT model.

The typical model wall temperature prior to a run ($T_{w,init}$) was between 294 K and 303 K. The model temperature depends on the stagnation temperature of the incoming air and the residual temperature of the model. The model temperature can gradually rise after subsequent runs in quick succession and will cool down overnight.

2.2.1 Modular Cone

The Modular Cone was designed by Joshua Edelman in 2016 [26] and is comprised of several modular sections. A schematic of the model is shown in Figure 2.4. It measures 405 mm in length along the centerline and has a 95-mm base diameter. The frustum sections fit along a central rod and are held between the nosetip and the base. The nosetip was fabricated from 17-4 PH stainless steel and threads into the central rod. The tip radius was measured with a calibrated Moticam 3 microscope camera. By comparing images of the nosetip radius

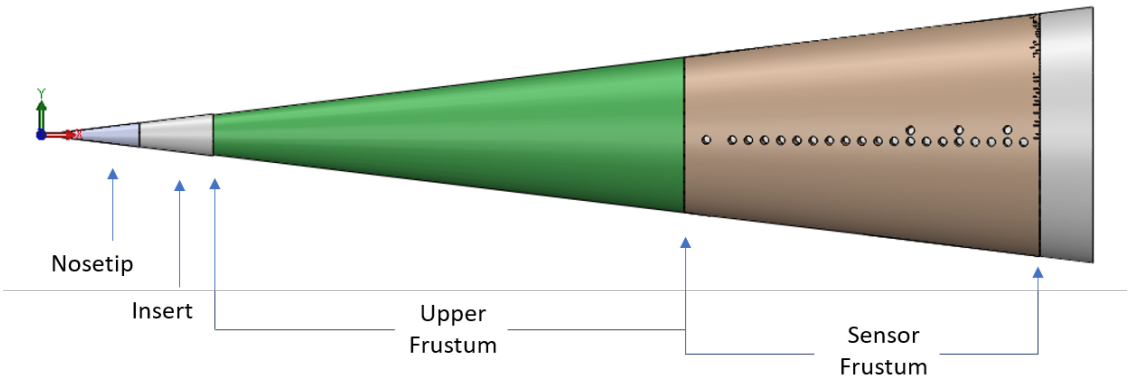

Figure 2.4. Schematic of the 7° half-angle Modular Cone.

and a 50-μm reference circle, the nosetip radius was estimated to be 37 μm. Both the Upper Frustum and Sensor Frustum were fabricated from polyether ether ketone (PEEK) to allow for IR thermography measurements. The sensor frustum contains 20 sensor ports along the primary ray and an additional 3 sensor ports that are offset by 6° azimuthally. The locations of these sensor ports are provided in Figure 2.5. Three additional sensor ports were added to the model, spaced in 90° azimuthal increments from the upstream-most sensor port that is located 255 mm downstream of the nosetip. This enabled a second-mode alignment technique. The insert section is held between the nosetip and Upper Frustum and can be easily interchanged while the model is installed in the BAM6QT.

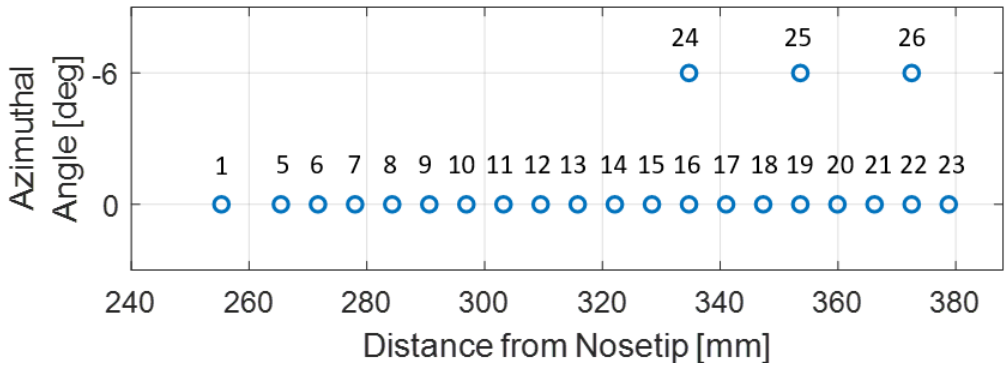

Figure 2.5. Sensor port naming conventions and locations on the Modular Cone.

To create steps in the geometry, the insert section is either shortened or lengthened. This results in a forward- or backward-facing step at the joint between the insert and the Upper Frustum, respectively. The step is uniform around the azimuth of the joint because the model is axisymmetric. Examples of shortened and lengthened inserts that create steps are shown in Figure 2.6. A total of 9 inserts were fabricated for this experiment. The step heights ranged from 0.610 mm to 1.219 mm. An insert with no step height was also fabricated for baseline measurements. Because the length of the insert varies, the location of the step relative to the nosetip is different for each step height. With the smooth-wall insert, the joint is located 63.5 mm from the nosetip. The joint location varies $\pm$ 10 mm with the different step heights. The nominal step height (k) and insert length for each insert are provided in Table 2.1. The boundary-layer thickness (δ), defined as the 99.5% of the total

enthalpy at freestream, was calculated using an in-house Stability and Transition Analysis for Hypersonic Boundary Layers (STABL) code. The computation was performed at T_0 = 433 K, P_0 = 140 psia, T_w = 300 K, and Re = 10×10^6 /m. Note that the computation does not include the step in the geometry. The ratio of the nominal step height to the boundary-layer thickness at the step location (k/δ) is also provided in Table 2.1. The largest step heights are more than two times as large as the boundary-layer thickness and were intended to create a measurable effect in the flow.

(a) A forward-facing step. (b) A backward-facing step.

Figure 2.6. Examples of shortened and lengthened inserts that create steps on the Modular Cone.

Table 2.1. Step heights on the Modular Cone and modified insert lengths

Nominal Step Height (k)	k/δ	**Nominal Insert Length**
− 1.219 mm (0.048 in.)	2.26	15.47 mm
− 1.016 mm (0.040 in.)	1.88	17.12 mm
− 0.813 mm (0.032 in.)	1.51	18.77 mm
− 0.610 mm (0.024 in.)	1.13	20.32 mm
± 0.000 mm (0.000 in.)	0.00	25.40 mm
+ 0.610 mm (0.024 in.)	1.13	30.48 mm
+ 0.813 mm (0.032 in.)	1.51	32.03 mm
+ 1.016 mm (0.040 in.)	1.88	33.68 mm
+ 1.219 mm (0.048 in.)	2.26	35.33 mm

The inserts were re-measured in November 2021 to verify the length of each insert. An error was found and has been corrected. The measurements reported prior to November

2021 erroneously labeled the largest two steps as 1.626 mm and 1.219 mm. The correct step height for the largest two steps should have been 1.219 mm and 1.016 mm, respectively.

2.2.2 33% Scale BOLT Model

The 33% scale BOLT model was originally fabricated at Johns Hopkins University Applied Physics Laboratory (JHU / APL) for use in several wind tunnel experiments. The model measures 288.6 mm in length along the centerline and has a 6.9° half-angle along the centerline of the experiment surface. A CAD rendering of the model is shown in Figure 2.7. The experiment surface that is seen facing upwards was fabricated from PEEK to allow for IR thermography measurements. This was the primary region of interest for the present work. There are 12 sensor ports on the PEEK experiment surface. These were fully instrumented with 10 Kulite and 2 PCB pressure sensors. The sensor naming conventions and coordinates are provided in Figure 2.8 and Table 2.2. The second experiment surface was fabricated from aluminum. Flow between the two experiment surfaces is separated by two gutter regions located on either side of the model. The surfaces are fastened to a central

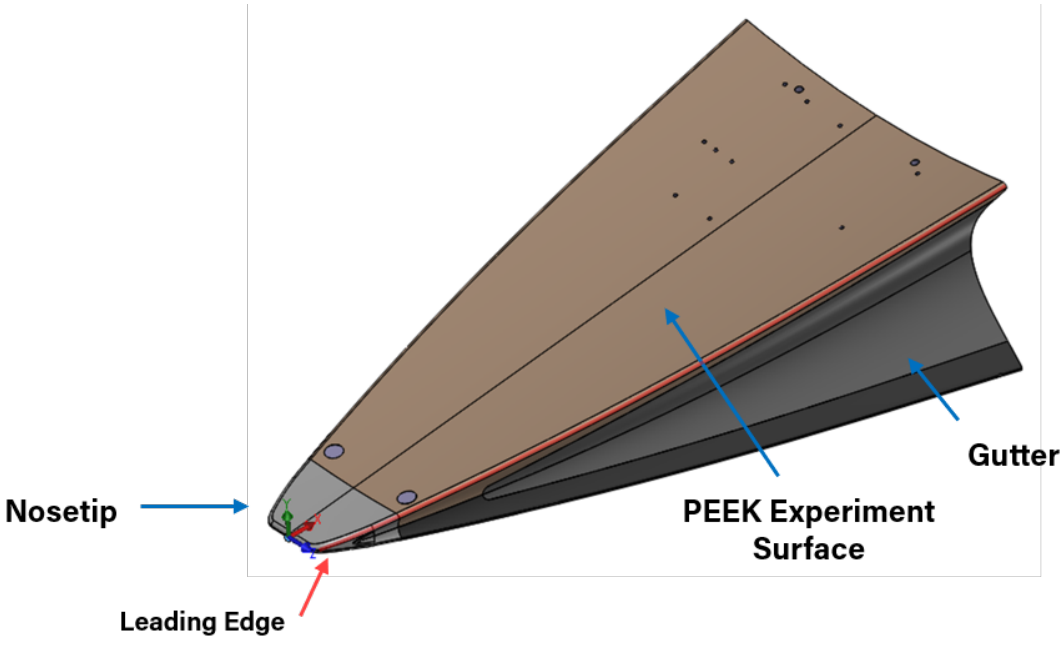

Figure 2.7. Schematic of the 33% scale BOLT model.

aluminum base. The stainless steel nosetip is interchangeable and can be independently removed from the rest of the assembly.

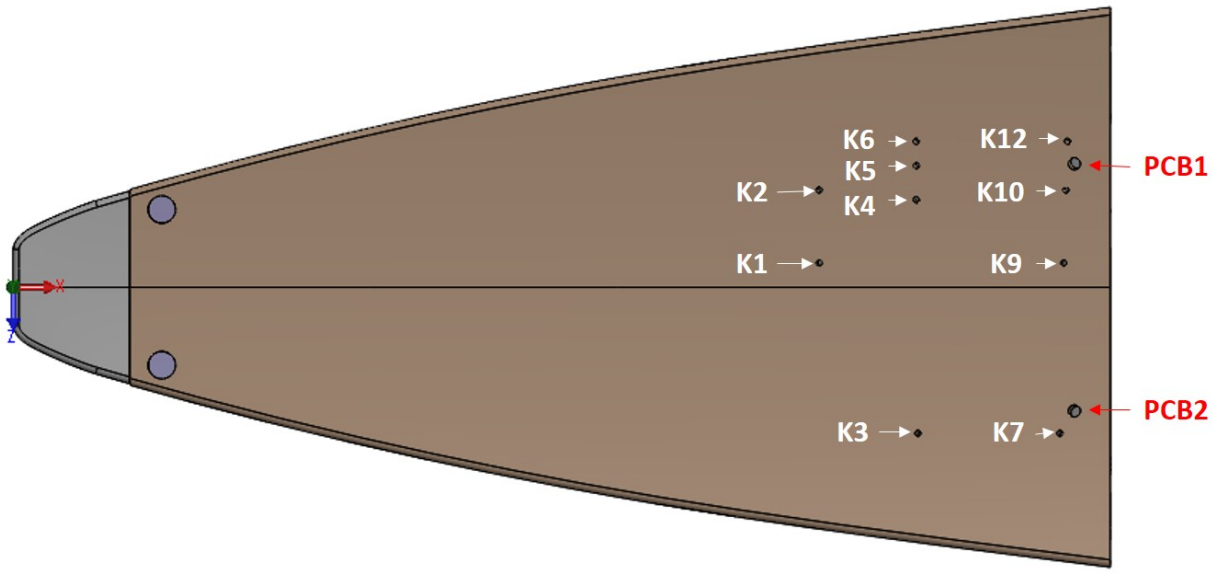

Figure 2.8. Sensor naming conventions and locations on the BOLT model.

Table 2.2. Sensor coordinates on the 33% scale BOLT model

Sensor Name	X	Z
K1	212.4 mm	-6.4 mm
K2	212.4 mm	-25.4 mm
K3	237.8 mm	38.1 mm
K4	237.8 mm	-22.9 mm
K5	237.8 mm	-31.8 mm
K6	237.8 mm	-38.1 mm
K7	275.9 mm	38.1 mm
K9	275.9 mm	-6.4 mm
K10	275.9 mm	-25.4 mm
K12	275.9 mm	-38.1 mm
PCB1	279.1 mm	-32.3 mm
PCB2	279.1 mm	32.3 mm

The model was provided by JHU / APL and modified to improve the alignment between the experiment surfaces and to better secure the nosetip to the aft sections of the model. A gap between the PEEK and aluminum experiment surface was thought to be caused by warping of the PEEK material. To address this, a stainless steel strongback was added to the base of the model. The strongback provides a rigid structure for the upstream portions of the experiment surfaces to fasten against. The nosetips are also better secured to the rigid strongback with four additional fasteners. The additional fasteners were intended to more accurately and repeatably position the nosetip with respect to the PEEK experiment surface. An exploded view of the modified model is shown in Figure 2.9. The upstream portion of the PEEK experiment surface fastens directly to the strongback. Two dowel pins and two screws secure the nosetip to the strongback. The dowel pins and screws are inserted through the aluminum experiment surface and result in a non-smooth experiment surface. Future use of the aluminum experiment surface would require some dental plaster to fill the

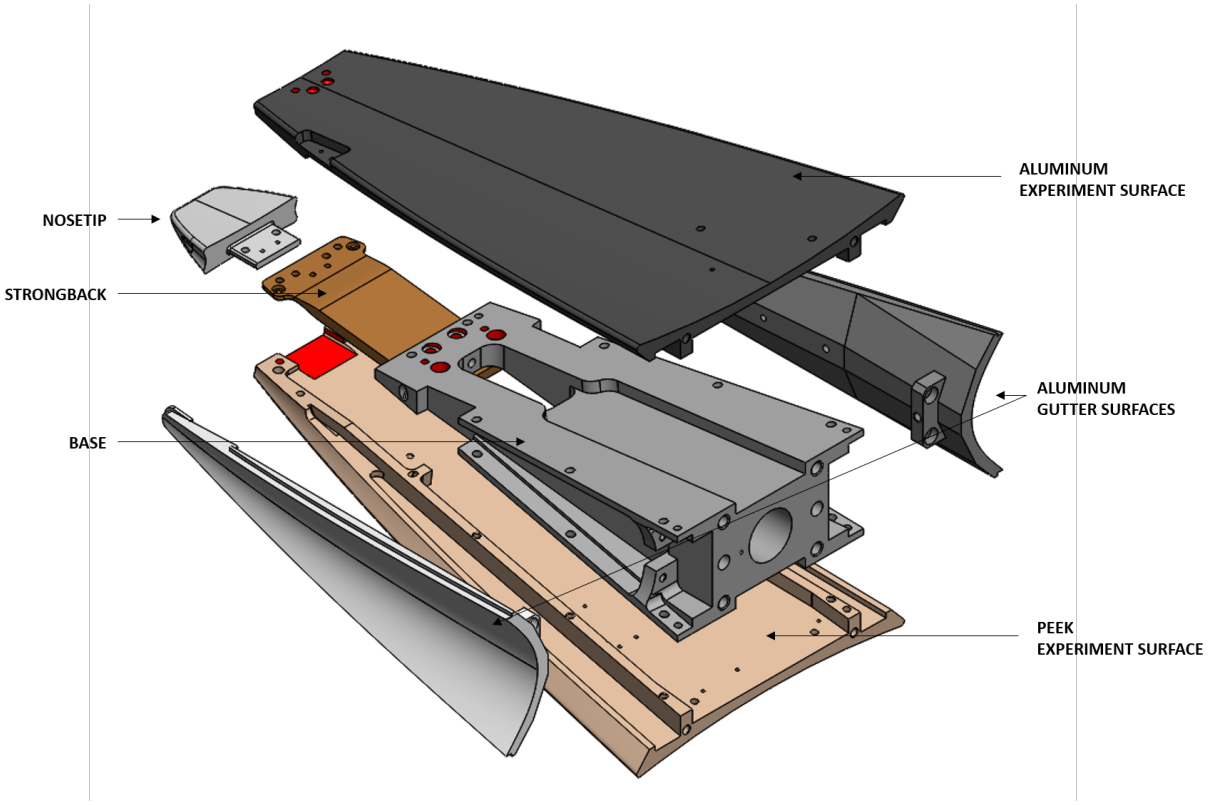

Figure 2.9. An exploded view of the modified BOLT model.

fastener heads. Each fastener was tightened to a specific torque to improve the repeatability of the assembly. The modifications were performed at TriModels in Huntington Beach, CA.

A set of nosetips was fabricated to accompany this new design. Each nosetip was either shortened or lengthened along the outer mold lining to create steps at the joint between the nosetip and the body. This was the same technique that was used in the experiments by Chynoweth et al. [23]. An example of a shortened nosetip that creates a forward-facing step is shown in Figure 2.10a. Because the geometry is three-dimensional, the step across the joint profile is not uniform. The largest step height exists at the leading edge of the joint profile. For the BOLT model, "k" is used to denote the step height at the leading edge joint. The location is illustrated in Figure 2.10b, where profiles of the body and of the shortened nosetip are plotted. The leading-edge location is marked on the upper-right quadrant. A smaller step exists at the centerline of the joint.

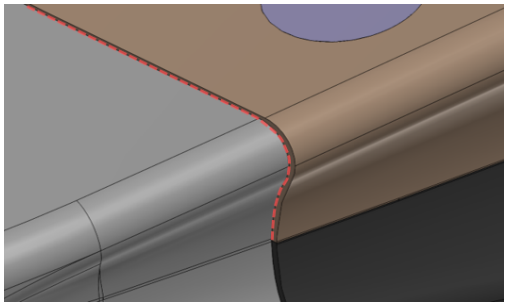

(a) A shortened nosetip on the BOLT model.

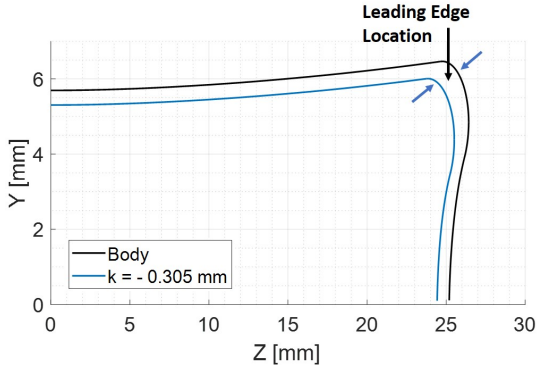

(b) Profiles of the body and shortened nosetip.

Figure 2.10. Example of a shortened nosetip that creates a forward-facing step on the BOLT model.

Seven different nosetips were fabricated for these experiments, five of which create steps. The sizing of the steps was selected with the intent to observe a measurable effect in the flow. These were based on the previous experiments by Chynoweth et al. [23]. The largest forward-facing step was 0.305 mm, and the largest backward-facing step was 1.016 mm. Two nosetips with no steps were fabricated. One was used for baseline measurements, and the other was polished to a mirror finish to investigate the effects of surface roughness. The nominal location of the joint is 31.75 mm downstream of the nosetip. However, the different

nosetip lengths result in different joint locations. The joint location varies by ± 4 mm. The leading-edge step heights (k) and nosetip lengths are provided in Table 2.3. The boundary-layer thickness (δ), defined as 99.5% of the freestream enthalpy, was computed by Wheaton [27] using CFD++. The computations were performed at T_0 = 433 K, P_0 = 140 psia, T_w = 300 K, and Re = 10×10^6 /m. The ratios of the LE step height and boundary-layer thickness (k/δ) are provided in Table 2.3. The majority of steps were larger than the boundary-layer thickness.

Table 2.3. Leading edge step heights on the 33% scale BOLT model and modified nosetip lengths

Nominal LE Step Height (k)	k/δ	**Nominal Nosetip Length**
− 0.305 mm (0.012 in.)	3.90	30.78 mm
− 0.152 mm (0.006 in.)	1.95	31.27 mm
− 0.076 mm (0.003 in.)	0.97	31.52 mm
± 0.000 mm (0.000 in.)	0.00	31.75 mm
+ 0.508 mm (0.020 in.)	6.50	33.35 mm
+ 1.016 mm (0.040 in.)	13.0	34.98 mm

Fabrication and measurement of these steps was difficult due to the small size and the three-dimensional nature of these steps. Additionally, the model is not perfectly symmetric due to fabrication tolerances. During the fabrication process of these nosetips, a coordinate measurement machine (CMM) was used to measure the leading-edge step heights. Locations just upstream and downstream of the joint were probed, and the step height was calculated as the difference between the two probe measurements closest to the leading edge. The nosetips were gradually cut until the probe measurements were within an acceptable tolerance of the nominal step height. A replica measurement technique that was previously used by Chynoweth et al. was also used to measure the leading-edge step heights. The replica measurement technique is discussed in Chapter 3, along with a comparison between the CMM and replica measurements on the BOLT model.

2.3 Instrumentation and Data Processing

2.3.1 Kulite XCE-SL-062-15A Pressure Transducers

Kulite XCE-SL-062-15A pressure transducers were used to measure mean pressure and pressure fluctuations on the surface of the wind-tunnel models. The circular sensor face measures 1.68 mm in diameter. The cylindrical sheath that houses the sensing element is 2.54 mm in length, about four times shorter than the standard Kulite XCE-062. This was necessary to fit within the small gap between the PEEK experiment surface and base of the BOLT model. The pressure-sensing principle of the sensor is a four-arm Wheatstone bridge that measures strain across a silicon diaphragm, which displaces linearly with the pressure forces exerted on the diaphragm. The operational pressure range is between 0 to 15 psia. Above 15 psia, the diaphragm is mechanically stopped to withstand the high stagnation pressures in the BAM6QT. The signal from the Kulite sensor is powered and filtered through an in-house conditioning box. A 100x gain is applied to the DC signal. An additional 100x gain and 840 Hz high-pass filter are applied to the AC signal. Each sensor is calibrated prior to the experiments against the Paroscientific pressure sensor. Because the operational pressure is below atmospheric conditions, the BAM6QT is drawn down to near-vacuum pressures to perform this calibration. The Kulite sensors have a nearly flat response up to about 40% of the resonant frequency, which is typically around 300 kHz [25].

2.3.2 Piezotronics PCB132B38 Pressure Sensors

PCB132B38 sensors were used to measure pressure fluctuations on the surface of both wind tunnel models. PCB sensors have long been used to measure high-frequency instabilities in the BAM6QT. The sensor is housed in a steel tube that measures 3.18 mm in diameter and 7.62 mm in length. Pressure fluctuations on the sensor head are measured with a piezoelectric sensing element. According to the manufacturer, the resolution of the sensor is 0.001 psia. The sensor is powered with a PCB483C05 conditioning box. The output signal is high-pass filtered at 11 kHz. The signal is converted into pressure fluctuations using a

factory calibration, which varies from sensor to sensor. The typical sensitivity is between 100 and 200 mV / psia.

2.3.3 HBM Gen7i Data Acquisition System

An HBM Gen7i data acquisition system (DAQ) was used to record the Kulite and PCB signals, as well as the tunnel conditions. The GN8103B data acquisition cards have a maximum sample rate of 25 MS/s and a 16-bit resolution. Electronic noise from these cards is higher when compared to the Tektronix DPO7054 oscilloscopes that have been used previously at Purdue. To reduce the noise to comparable levels, a real-time Bessel low-pass filter with a 2 MHz cutoff frequency was applied to the Kulite and PCB signals. Both Kulite and PCB sensors were sampled at a 20 MHz sample rate and then downsampled to 2 MHz to reduce the volume of data. The contraction Kulite, hot-film, and nozzle-wall Kulite signals were also recorded on GN8103B cards but at a lower 500 kHz sample rate.

2.3.4 Analysis of Pressure Fluctuations

Kulite and PCB pressure fluctuation measurements were normalized using the tangent-cone and tangent-wedge methods, as described by Anderson [28]. The tangent-cone method approximates the pressure on a conical-like surface using the Taylor-Maccoll solution. The tangent-wedge method approximates the pressure on a wedge-like surface using the oblique shock relation. The wedge half-angle for the BOLT geometry is approximately 6.9°. The ratio between the freestream static pressure and the approximate surface pressure is calculated with Equation 2.5.

$$\frac{p_2}{p_1} = 1 + \frac{2\gamma}{\gamma + 1} \cdot (M_1^2 sin^2(\beta) - 1) \tag{2.5}$$

The spectral content contained within pressure fluctuations was analyzed using power spectral densities (PSD). The PSD are calculated over a 20 ms record using Welch's method. The record was broken into 80 segments with a 50% overlap. A Hamming window was applied to each segment. The root-mean-square (RMS) of the pressure fluctuations was

calculated from the power spectra by taking the square root of the integral of the PSD. Different frequency bands are selected for the different sensor types. For PCB sensors, the frequency band is 11 kHz to 500 kHz. For Kulite sensors, the frequency band is from 0 kHz to 250 kHz.

2.3.5 IR Thermography Measurement System

An IR thermography measurement method has been developed at Purdue University to acquire higher-resolution thermography as compared to temperature-sensitive paint (TSP) [25] [26] [29] [30]. An in-depth discussion of the method can be found in Appendix D of Reference [26]. An Infratec IR hp8300 camera is used to image the wind tunnel models through a CaF_2 porthole window. The camera has a spectral range between 2 and 5 μm, a temperature resolution of 0.02 K, and a 640 $\times$ 512-pixel resolution. The camera can record at a frame rate of 300 Hz, but a frame rate of 200 Hz is typically used to reduce the volume of data. Polyether ether ketone (PEEK) has a high emissivity and low thermal conductivity. It has been demonstrated as a suitable material for wind tunnel models.

The IR thermography measurements are analyzed using the Purdue Infrared ANd Heat Transfer App (PIRANHA). Details on the code can be found in Reference [26]. The processing code accounts for tunnel movement and optical distortions from the camera lens. The 2-D temperature image is then unwrapped into a 3-D representation of the model surface. IR images of the two wind tunnel models and the superimposed meshes are shown in Figure 2.11. The mesh is positioned by using sensor coordinates as reference points.

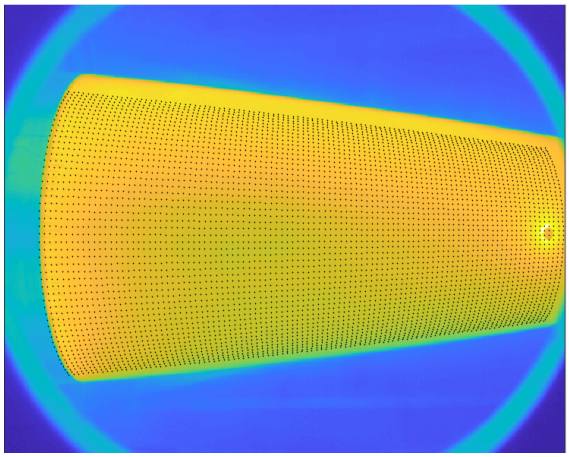

(a) Modular Cone.

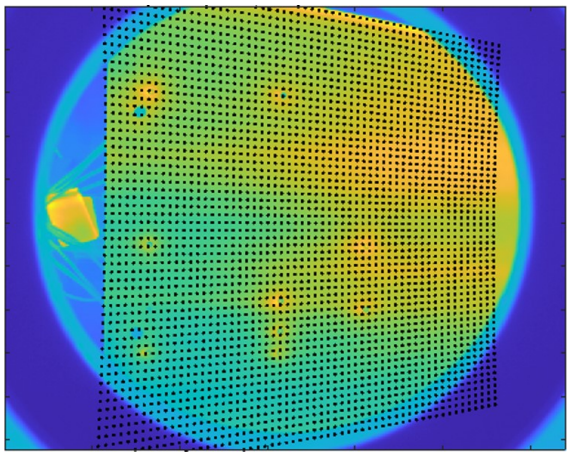

(b) BOLT Model.

Figure 2.11. IR images of the Modular Cone and the BOLT model with a superimposed mesh.

The heat flux and Stanton number are calculated using a 1-D heat transfer method. The accuracy of the heat transfer calculation is within about 10% [25]. The Stanton number formulation that is used by the processing code is provided in Equation 2.6. This formulation was adopted from the PIRANHA processing code, and was similarly used in [26] and [25]. The Stanton number is calculated at each point in the mesh and at each frame of data. For this experiment, heat transfer magnitudes are represented as a scaled Stanton number that is multiplied by the square root of the freestream Reynolds number. This was done to scale the heating magnitude using a method appropriate to a laminar boundary layer.

$$St = \frac{q}{\mu \cdot Re_m \cdot c_p(T_0 - T_w)} \tag{2.6}$$

where μ is the dynamic viscosity in the freestream calculated using Sutherland's law, Re_m is the freestream unit Reynolds number per meter, c_p is the specific heat capacity of air, T_w is the temperature of the model during the run and T_0 is the stagnation temperature of freestream air at the time data was processed. A constant c_p value of 1004.5 $\frac{J}{kg \cdot K}$ was used for this calculation.

3. REPLICA MEASUREMENT TECHNIQUE

The replica measurement technique has been developed and used to measure step heights and surface roughness. First, a high-resolution replica of the surface is created. Then, the replica is measured underneath a Zygo ZeGage optical profiler. This technique has many benefits over a traditional surface profilometer. The creation of the replica is non-destructive and will not scratch the surface. The replica can also be created over a three-dimensional surface, whereas a profilometer has difficulty due to a lack of a flat reference surface. The technique was originally adapted from John Newman of NASA Langley, who used the measurement technique to inspect fractures on the Space Shuttle engines [31]. The technique and replication material, Struers RepliSet-T3, were suggested by Rudy King of NASA Langley.

Struers RepliSet-T3 is a replication system that is non-destructive and can accurately replicate a 2-D or 3-D surface. According to the manufacturer, the material has a 0.004 mil (0.1 μm) resolution. To create a replica, the material is dispensed through a mixing nozzle that activates a curing process. The dispensed material can be spread and molded onto a surface for two minutes before it starts to harden. The low viscosity allows it to seep into small features of a surface, such as a joint from a step or an indent due to a recessed sensor. A sheet of backing paper that bonds to the RepliSet-T3 material is attached for labeling and to remove the replica from the surface. After the replica has fully cured over a 10-minute period, it is removed from the surface and measured. The cured replica can also be stored for future use.

The Zygo ZeGage optical profiler generates a 2-D depth map of a surface and has an optical resolution of 0.04 mil (1 μm) to 0.14 mil (3.6 μm) [32]. The tool uses Coherence Scanning Interferometry (CSI) to determine the relative height of a surface in relation to the objective lens. The scanning turret traverses across different heights above the measurement surface to generate a depth map. Pictures of the Zygo ZeGage and a RepliSet-T3 replica underneath the objective lens are shown in Figure 3.1. With the 2.75x objective lens, a 120 mil x 120 mil (3 mm x 3 mm) area can be scanned.

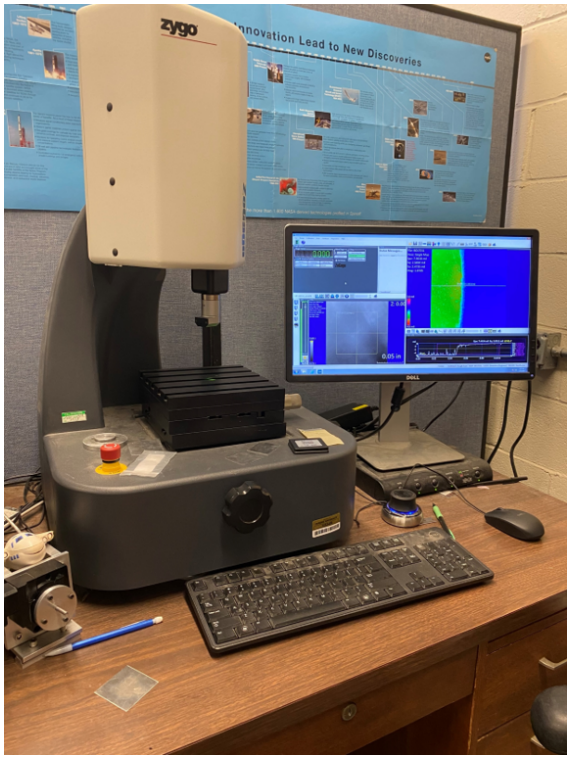

(a) Zygo ZeGage optical profiler.

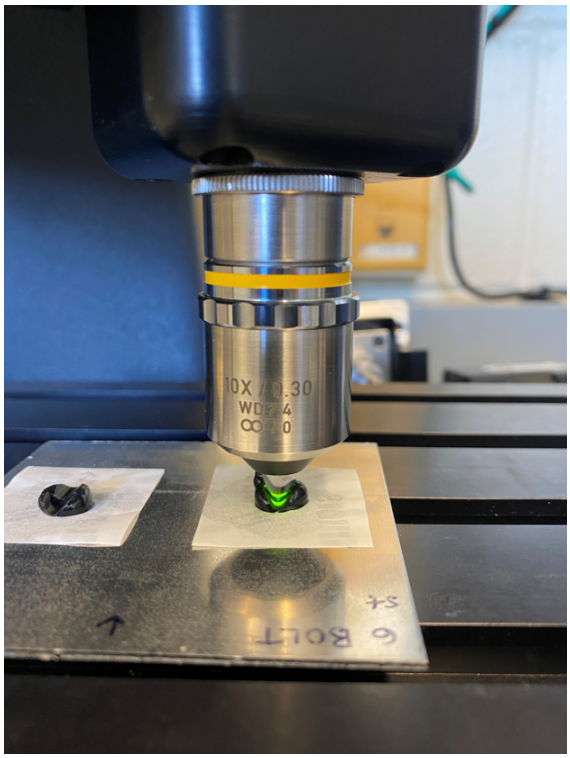

(b) A replica underneath the Zygo lens.

Figure 3.1. The Zygo ZeGage optical profiler and an example of a replica being measured.

3.1 Measurements on a Flat Surface

The primary motivation for use of this measurement technique was to measure the leading-edge step heights on the BOLT flight vehicle and 33% scale BOLT model. These geometries are three-dimensional and highly curved, which are difficult to measure with a surface profilometer. Although the specified resolution of the Zygo and the RepliSet-T3 material is on the order of microns, the accuracy of the measurement technique is likely worse due to human-related error. Application of the replica material and positioning of the replica underneath the Zygo are dependent on the skill of the operator and can affect the accuracy and repeatability of these measurements. To help determine the accuracy of the measurement technique, a test coupon was fabricated. The test coupon was a flat aluminum plate with a nominal 20 mil step. The test coupon was fabricated in-house in the ASL machine shop. A photo of the test coupon is shown in Figure 3.4a. Replicas of the step

were made and measured with the Zygo, and then compared to a direct measurement of the step underneath the Zygo. These measurements were obtained at the marked location in the image. A sharpie mark was used because it transfers onto the replica and can be visually identified under the Zygo. The sharpie mark does not create a significant elevation on the surface, so it is not visible in the depth map. The sharpie mark is identifiable in the visual preview through the lens and is positioned at the center of the scanning area. An image of the replica of the step is shown in Figure 3.2b, along with the depth maps that were measured by the Zygo in Figures 3.2c and 3.2d. A first-order polynomial fit was removed from the surface maps to correct for the tilt of the measurement stand.

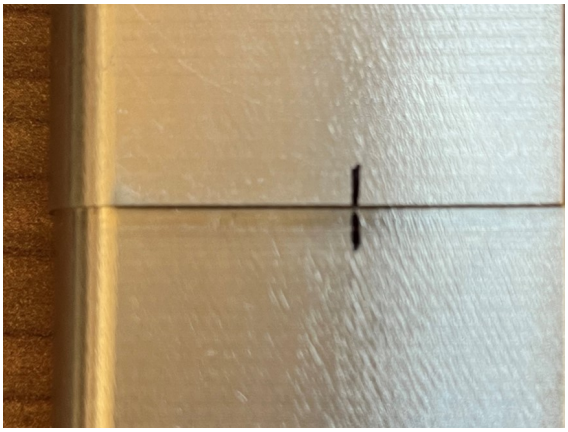

(a) Step on a flat surface.

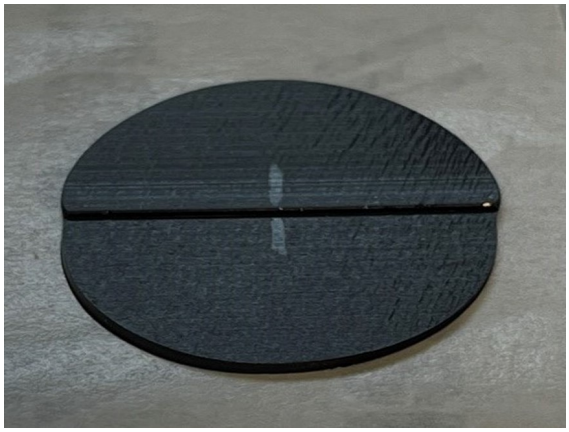

(b) Replica of the step.

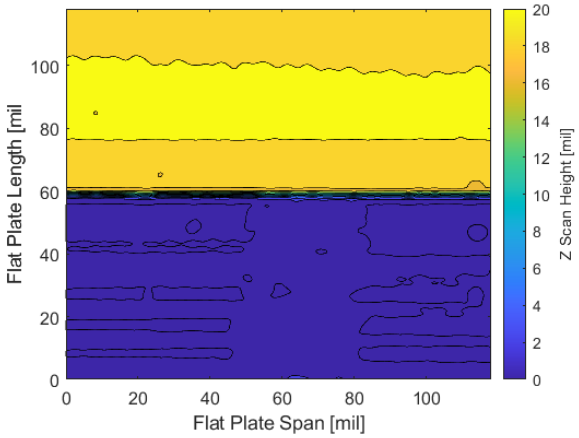

(c) Zygo depth map of the test coupon.

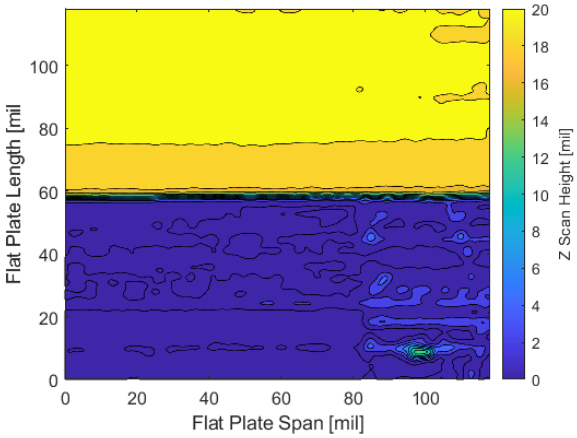

(d) Zygo depth map of the replica.

Figure 3.2. Direct scan and replica measurements of the step on a flat surface.

To calculate the step height from the depth map, a perpendicular profile is first extracted at the marked location. An averaged profile that spans 0.8 mil is extracted from the depth map and shown in Figure 3.3. The 0.8 mil span was selected to match the radius of a profilometer stylus and to reduce noise in the depth map. The step height is calculated as the difference between the heights of the upper and lower surface. With the 2.75x lens, the upper and lower heights were selected at locations 40 mil away from the step. This was selected to avoid slopes near the step and was typically a good representation of the surface. Some depth maps had higher noise and resulted in a less uniform upper and lower height. The locations of the lower and upper heights would be shifted to avoid noisy portions of the data.

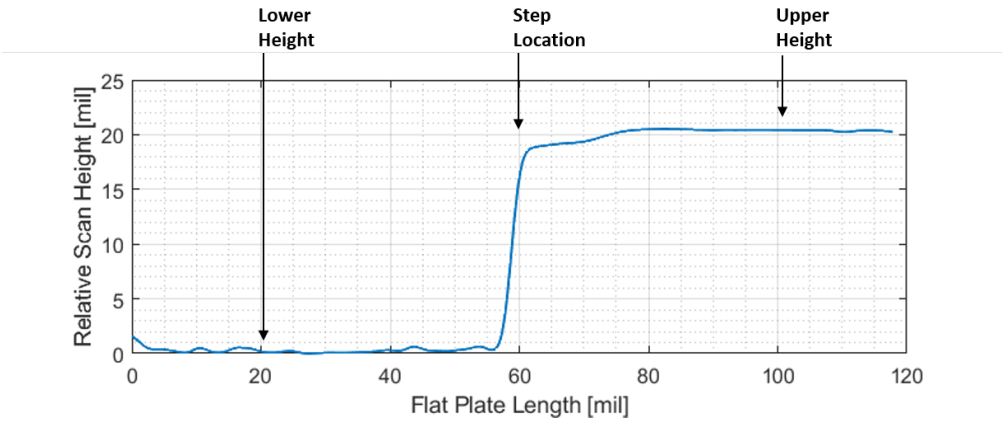

Figure 3.3. Averaged lengthwise profile of Figure 3.2d. Upper and lower heights are positioned 40 mil away from the step location.

Replicas of the test coupon were also created with different replication materials to determine if a better accuracy could be achieved when compared to the RepliSet-T3 material. Some materials were of different colors and were thought to provide a better signal-to-noise ratio underneath the Zygo. The RepliSet-T3, RepliSet-GF1, MicroSet 101TH, and MicroSet 101FF all had a quoted resolution of 0.004 mil (0.1 μm). The MicroSet 101FF was grey, and the others were black. The RepliFix-2 material had a lower 0.020 mil (0.5 μm) resolution but created a rigid replica after the curing process. It was thought that the additional rigidity might create a more accurate replica. The MicroSet 202 material also had a lower 0.5-micron resolution and had a lower cure time of 5 minutes. This faster cure time would increase the

number of replicas that could be made. The direct measurement of the test coupon and measurements with the different replication materials are provided in Table 3.1.

Table 3.1. Measurements of the step on a flat surface

Material	Step Height
Aluminum (Direct)	19.56 mil
MicroSet 101FF	19.46 mil
MicroSet 101TH	19.02 mil
MicroSet 202	18.36 mil
Struers RepliFix-2	18.46 mil
Struers RepliSet-GF1	19.39 mil
Struers RepliSet-T3	19.11 mil

The direct measurement of the test coupon resulted in a step height of 19.56 mil. Measurements with the Struers RepliSet-GF1, RepliSet-T3, MicroSet 101FF, and MicroSet 101TH were all within 0.5 mil of the direct measurement. Only one replica was created, so the variation of the replicas could not be quantified. It was unclear if the grey color of the material had an impact on the accuracy of the measurement or whether the accuracy was due to variations in the replica. The step heights on the MicroSet 202 and RepliFix-2 replicas were approximately 1 mil smaller than the direct measurement.

3.2 Measurements on a Curved Surface

The Zygo cannot reliably measure surfaces that are at a slope relative to the Zygo lens, such as the leading edges of the BOLT geometry. The replicas would be "unwrapped" and glued onto an aluminum sheet to flatten the surface. It was thought that the unwrapping process would introduce distortions into the replica. To test this, a controlled step was machined into a curved surface. The step was cut into a half-cylinder with a 0.25-inch radius to emulate the radius of curvature on the leading edge of the BOLT flight vehicle. For reference, the 33% scale BOLT model has an approximate radius of curvature of 0.06-inch at the leading edge. The nominal 20 mil step was cut along the curved cylinder in the ASL machine shop. The completed part is shown in Figure 3.4.

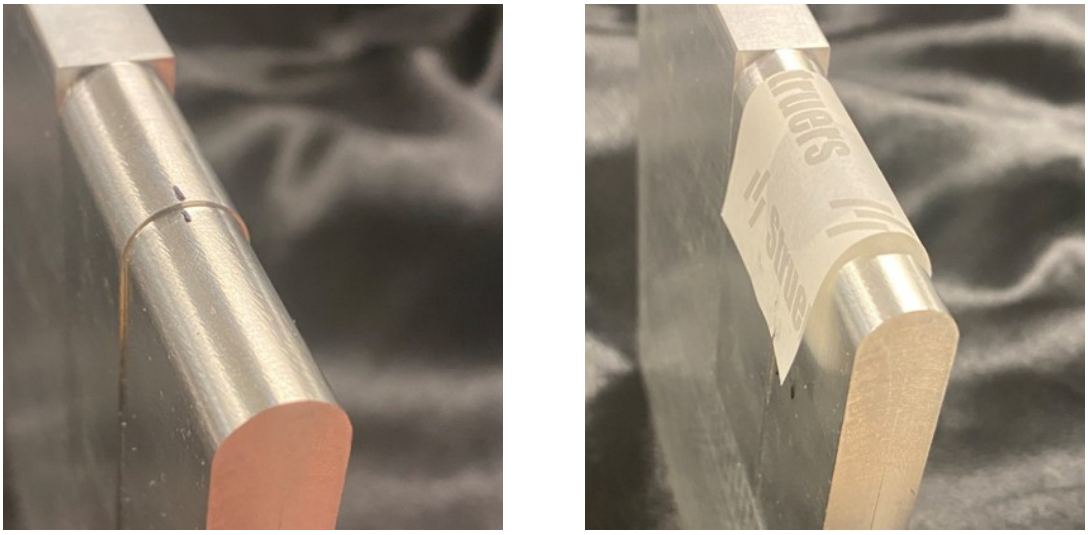

(a) Step on a curved surface. (b) RepliSet-T3 on the curved surface.

Figure 3.4. Step on a curved surface and RepliSet-T3 application.

The replica material was applied to the curved surface and pressed flat against the joint with the backing paper. This was done to create a thin and uniformly-thick replica that is needed to unwrap the profile into a flat surface. During the 10-minute curing period, the replica is held in place. An image of the unwrapped replica that is glued onto an aluminum sheet is shown in Figure 3.5a. The replica has a slight curvature that is difficult to see in the image. However, a slight curvature is likely caused by a non-uniformity in the thickness of

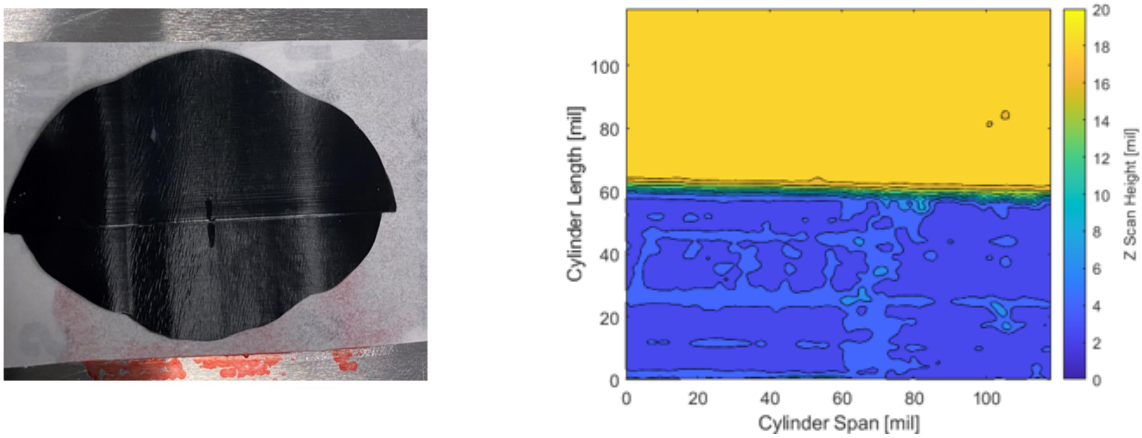

(a) Unwrapped replica of the curved step height. (b) Zygo depth map of the replica.

Figure 3.5. Replica and depth map of a step on a curved surface.

the material. To remove the small curvature in the depth map, a second-order polynomial was removed. The Zygo scan of the marked location is shown in Figure 3.5b.

The test coupon was placed underneath the Zygo to make a direct measurement of the step. The direct measurement of the step height at the marked location was 15.80 mil. The difference between this measurement and the intended 20-mil step height was likely due to fabrication errors. Two replicas with each material were created on this step and unwrapped. The step heights were calculated using the same methodology that was used with the steps on the flat surface. The measurements from each replica are provided in Table 3.2. All of the replicas were within ± 0.7 mil of the direct measurement. This indicates that the replicas were capable of accurate measurements on a curved surface. The differences between the replica measurements and the direct measurement were similar to the differences on the flat surface, which suggests that the unwrapping process does not contribute a significant distortion into the replica for this type of sample. The RepliSet-T3 material was selected for use in the BOLT measurements because it was readily available and to remain consistent with previous measurements.

Table 3.2. Measurements of the step on a curved surface

Material	**Replica 1** [mil]	**Replica 2** [mil]	**Mean** [mil]
MicroSet 101FF	16.00	15.19	15.60
MicroSet 101TH	15.78	15.12	15.45
MicroSet 202	16.28	15.35	15.82
Struers RepliSet-GF1	15.72	16.13	15.93
Struers RepliSet-T3	15.71	15.90	15.81

The repeatability of RepliSet-T3 measurements was also tested on the curved surface. Four additional replicas were created and measured. The measured step heights are provided in Table 3.3, along with the difference between the measured step height and the direct 15.80 mil measurement of the step height. The repeatability of the set of replicas was within 0.48 mil (12 μm) of the direct measurement. The variation between measurements was thought to be caused by the application and handling of the replica material.

Table 3.3. Repeat RepliSet-T3 measurements of the step on a curved surface

Replica #	Measured [mil]	Difference [mil]
1	15.71	0.09
2	15.90	0.10
3	15.90	0.21
4	15.59	0.21
5	16.14	0.34
6	15.32	0.48

3.3 Measurements on the BOLT Flight Vehicle

Replicas were created on the actual BOLT flight vehicle in November 2019. The primary objective was to measure the leading-edge steps between the upstream (nosetip-isolator) and downstream (isolator-frustum) joints. These would be compared to the as-designed values and also to photogrammetry measurements that were performed at APL [27]. By taking high-resolution photos of the step height next to a reference shim of known thickness, the step height can be approximated. The steps along the centerline of the two joints and the surface roughness on each surface were also measured. The locations of the measurement locations are shown in Figure 3.7, where "LE" denotes the leading-edge joint and "CL" denotes the centerline. The vehicle was divided into four quadrants to assist with data organization.

A secondary set of replicas was created in June 2020 to obtain additional measurements of the leading-edge joints. Three additional replicas were created at each location. The intent was to verify the previous set of measurements with additional data points. Some replicas were backed with a rigid RepliFix-2 material to investigate whether the unwrapping of the replicas had a significant effect on the measured step height. This set of replicas was sent to NASA Langley Research Center to be measured.

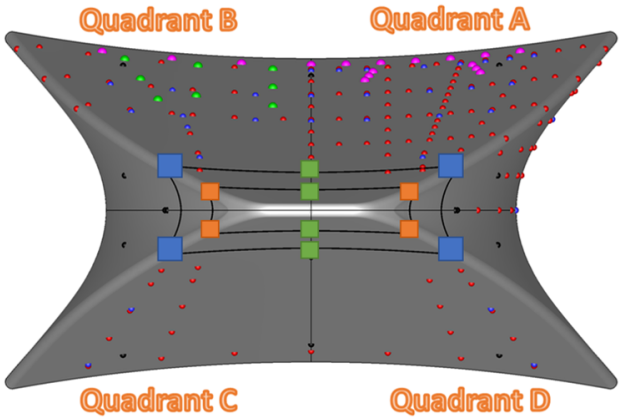

Quad	Joint	Pos.
A	Upstream	LE
B	Upstream	LE
C	Upstream	LE
D	Upstream	LE
A	Downstream	LE
B	Downstream	LE
C	Downstream	LE
D	Downstream	LE
AB	Upstream	CL
CD	Upstream	CL
AB	Downstream	CL
CD	Downstream	CL

Figure 3.6. Locations where replicas were created on the BOLT flight vehicle.

The leading edges on the BOLT vehicle were marked with a sharpie so that a reference location could be identified on the replicas. Similar markings were placed on the centerline. Because the markings were placed by hand, the locations were not exactly representative of the location where the step height was at a maximum. Examples of the marked locations are shown in Figure 3.7.

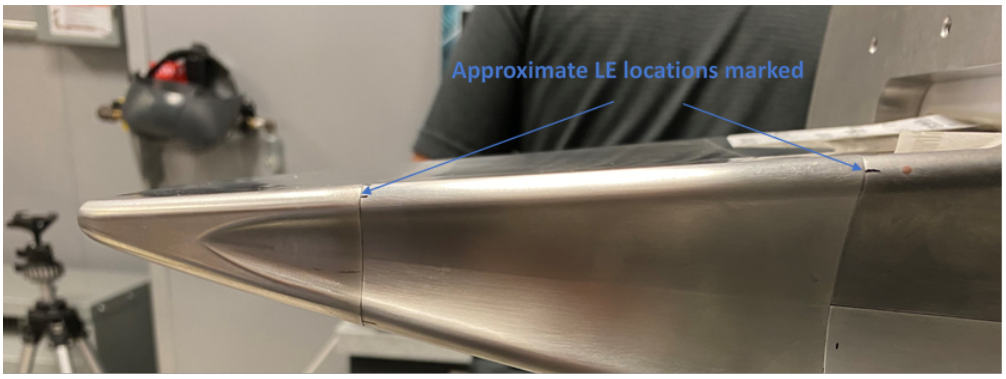

Figure 3.7. Leading-edge markings on the BOLT flight vehicle.

Two replicas were created at each location. The replicas were unwrapped and fixed onto aluminum sheets. An image of the Quadrant A Upstream replica is shown in Figure 3.8a. The replica still retains some curvature due to some non-uniformity in the replica thickness. A second-order polynomial fit was removed from the depth map to filter out the curvature from the replica. The filtered depth map is shown in Figure 3.8b.

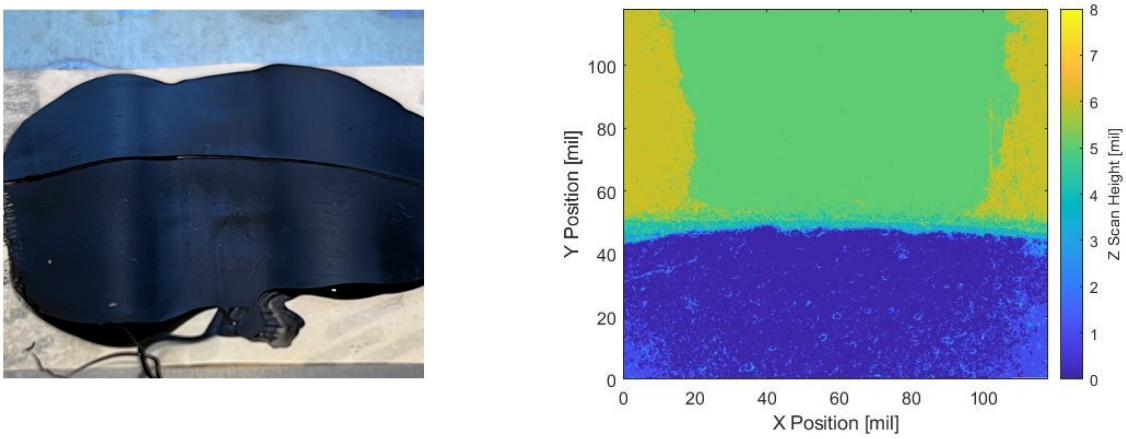

(a) RepliSet-T3 replica.

(b) Zygo depth map.

Figure 3.8. Replica and depth map of the Quadrant A Upstream leading-edge joint on the BOLT flight vehicle.

The leading-edge step heights were calculated from each replica and provided in Table 3.4, along with the as-designed value and photogrammetry measurement. The replica measurements at the upstream (nosetip-isolator) joint were smaller than the as-designed values and the photogrammetry measurements. A smaller step may result in a forward-facing step after thermal differential expansion occurs [27]. Because the steps were calculated at the marked sharpie location, the step may not be representative of the maximum step height. An attempt was made to scan adjacent joint profiles and stitch the depth maps together. This would make it possible to identify the local maximum along the joint. However, good quality scans adjacent to the marked locations could not be obtained. It was thought that the Zygo was limited by the curvature of the replica.

The replica measurements at the downstream (isolator-frustum) and centerline joints were in good agreement with the photogrammetry measurements. The step at the Quadrant C downstream leading edge appears to be larger than the as-designed value, whereas the step height at the Quadrant D leading edge appears to be smaller than the as-designed value.

Table 3.4. Step height measurements on the BOLT flight vehicle.

Quad.	**Joint Pos.**	**Pos.**	**As-Designed** [mil]	**Photogrammetry** [mil]	**Replica** [mil, mil]
A	Upstream	LE	8.0	7.4	4.2, 5.4
B	Upstream	LE	8.0	8.9	4.2, 4.3
C	Upstream	LE	8.0	8.9	4.4, 4.8
D	Upstream	LE	8.0	7.2	6.7, 6.8
A	Downstream	LE	7.1	6.5	6.6, 7.6
B	Downstream	LE	7.1	6.0	8.2, 8.3
C	Downstream	LE	21.1	28.0	27.4, 29.4
D	Downstream	LE	21.1	13.0	15.6, 16.8
AB	Upstream	CL	3.0	4.0	4.3, 4.6
CD	Upstream	CL	3.0	4.0	3.8, 4.1
AB	Downstream	CL	2.9	3.5	3.6, 3.9
CD	Downstream	CL	8.6	8.9	10.0, 12.0

Replicas were also created on the nosetip, isolator, and acreage surface to measure the distributed roughness. A replica was also created on the gutter, where the surface was scratched by a tool. This location was referred to as the "ding" location. The surface roughness is quantified as the RMS of surface roughness along a profile (R_a). Because a 2-D depth map is generated, the R_a metric can be calculated in the streamwise and spanwise directions. Surface roughness measurements at the nosetip leading edge and along the nosetip acreage are compared to profilometer measurements that were performed by Ultramet. Three replicas were created along the nosetip leading-edge: one at the centerline, one approximately 2 inches to the port side, and one approximately 2 inches to the starboard side. Measurements of these replicas are provided in Table 3.5.

The measured surface roughness on the nosetip acreage was in good agreement with the profilometer measurement. The streamwise and spanwise roughness were of similar magnitude, indicating that the surface roughness was evenly distributed. Measurements on the isolator and primary acreage were of similar magnitudes to the nosetip acreage. The surface roughness at the ding location was 2 to 8 times higher than the surface roughness on the primary acreage. Measurements on the nosetip leading edge were similar to the profilometer measurements.

Table 3.5. Surface roughness measurements on the BOLT flight vehicle.

Location	**Profilometer** [μ-in.]	**Spanwise** R_a [μ-in.]	**Streamwise** R_a [μ-in.]
Nosetip Acreage	13 - 27	17.52 - 29.63	23.34 - 25.02
Isolator Acreage	no measurement	3.65 - 9.03	2.56 - 7.41
Frustum Acreage	no measurement	7.98 - 15.96	6.17 - 10.26
Ding Location	no measurement	21.57 - 86.51	17.56 - 37.34
Nosetip LE #1	19	18.31	-
Nosetip LE #2	32	15.09	-
Nosetip LE #3	31	18.53	-

3.4 Measurements on the 33% scale BOLT Model

Steps on the 33% scale BOLT model were also measured using the replica measurement technique. The smaller size of the joint and the higher curvature made it difficult to unwrap the replicas. Because of this, the replicas were left in a curved form. An example of these replicas is shown in Figure 3.9a. The high curvature posed many issues for the Zygo, and measurements could only be obtained with the 10x lens. The 2.75x lens could not get close enough to the step without contacting the replica. Using the 10x lens resulted in a smaller depth map with an area of 34 mil by 34 mil. Similar to the BOLT vehicle measurements, a sharpie mark was drawn on the leading edge to provide a reference location on the replicas.

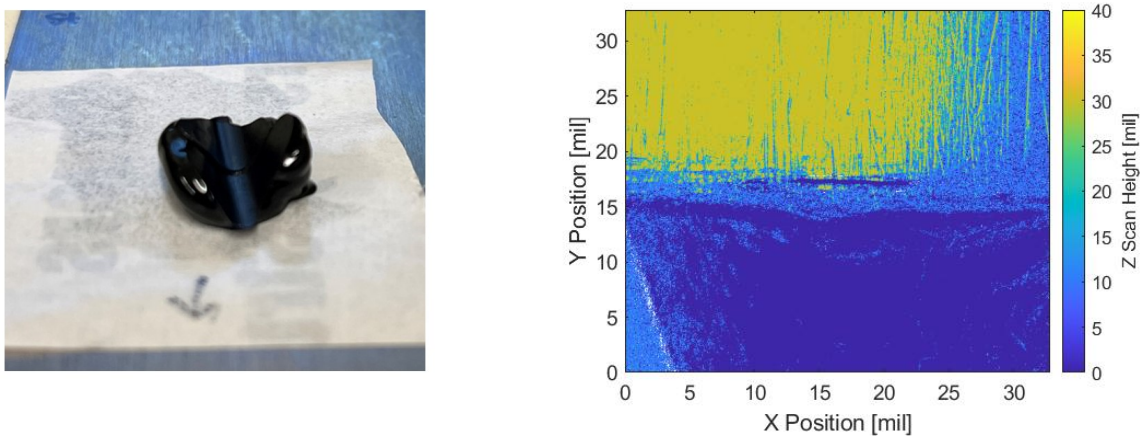

(a) Curved replica. (b) Depth map.

Figure 3.9. Replica and depth map of the 1.016 mm backward-facing step on the 33% scale BOLT model.

Two sets of replica measurements were performed on the model. The first set of replicas was created immediately after the experiments in December 2020 (Entry 3). This was done to reduce any uncertainty that may arise due to the assembly of the model. The second set of replicas was created after the model was disassembled and reassembled. The second set of replicas was created by Cassandra Butler and was intended to verify the first set of measurements. Measurements on the starboard and port side of the model are provided in Tables 3.6 and 3.7, respectively. The CMM measurements from TriModels are also provided and compared to the replica measurements.

Table 3.6. Leading edge step height measurements on the starboard side of the 33% scale BOLT model

Nominal LE Step (k)	**CMM** [mm]	**Replica 1** [mm]	**Replica 2** [mm]
− 0.305 mm (Forward-facing)	− 0.229	− 0.228	− 0.203
− 0.152 mm (Forward-facing)	− 0.102	− 0.127	− 0.102
− 0.076 mm (Forward-facing)	− 0.000	− 0.051	− 0.051
± 0.000 mm (Unpolished)	+ 0.051	+ 0.051	+ 0.051
± 0.000 mm (Polished)	+ 0.051	+ 0.051	+ 0.025
+ 0.508 mm (Backward-facing)	+ 0.660	+ 0.584	+ 0.559
+ 1.016 mm (Backward-facing)	+ 1.067	+ 0.965	+ 1.016

All of the forward-facing steps on the starboard side of the model were smaller than the nominal size. A smaller size was seen in both the CMM and replica measurements, indicating that the difference was likely not attributed to a variance in the measurement method. Measurements on the unpolished and polished smooth-wall nosetips indicate a small backward-facing step. Measurements on the backward-facing steps were slightly larger than the nominal sizes. The two replica measurements are in relatively good agreement, indicating that the removal and reinstallation of the nosetip did not cause a significant change in the step height. Differences between the two replica measurements may also be attributed to variances in the replica application and handling.

Table 3.7. Leading edge step height measurements on the port side of the 33% scale BOLT model

Nominal LE Step (k)	**CMM** [mm]	**Replica 1** [mm]	**Replica 2** [mm]
− 0.305 mm (Forward-facing)	− 0.203	− 0.178	− 0.203
− 0.152 mm (Forward-facing)	− 0.051	− 0.025	− 0.025
− 0.076 mm (Forward-facing)	− 0.000	− 0.000	− 0.000
± 0.000 mm (Unpolished)	− 0.000	− 0.000	− 0.000
± 0.000 mm (Polished)	+ 0.051	+ 0.076	+ 0.076
+ 0.508 mm (Backward-facing)	+ 0.483	+ 0.508	+ 0.533
+ 1.016 mm (Backward-facing)	+ 0.965	+ 1.092	+ 0.813

The forward-facing steps on the port side of the model were also smaller than the nominal sizes. In the CMM and both replica measurements, the nominal 0.152 mm and 0.076 mm forward-facing steps were measured to be much smaller and close to a smooth wall. This may result in a diminished effect of the forward-facing steps on the port side of the experiment surface. A minimal step was measured with the unpolished smooth-wall nosetip, whereas a small backward-facing step was measured with the polished smooth-wall nosetip. The backward-facing steps were measured to be slightly smaller than the nominal sizes.

The measured step heights on the port side and starboard side of the nosetips are different and suggest that there is a slight asymmetry in the geometry. This asymmetry might be caused by small fabrication tolerances in the nosetip geometry or a misalignment between the nosetip and the body. It could also be caused by variances in the measurement techniques. Replica measurements on the controlled, curved step have shown to be repeatable within 0.012 mm (0.48 mil). The differences between the replica and nominal sizes were larger than this. However, the controlled, curved step was two-dimensional and had a higher radius of curvature when compared to the leading edge of the BOLT model. Creating and measuring replicas on a smaller and 3-dimensional step is more challenging and likely introduces more handling-related errors. Because the geometry is small and highly three-dimensional, the exact cause of asymmetry is difficult to pinpoint.

4. EXPERIMENTS WITH THE MODULAR CONE

The majority of cone experiments were performed in June 2020 during Entry 4. The run matrix from this Entry is provided in Appendix A. For each run, the vacuum pressure was below 5 torr. The reported values of stagnation pressure and temperature were calculated during the run at the time where data was processed. The initial wall temperature ($T_{w,init}$) of the cone was between 294 K and 303 K. Figures shown in this section are labeled with the respective run number associated with the data so that the stagnation conditions can be obtained.

4.1 Measurements at $\alpha = 0°$

4.1.1 Aligning to Zero Angle of Attack

A method to align a cone using second-mode frequencies was developed by Willems et al. [33]. If the cone is at 0.0° angle of attack, the second-mode frequencies around the cone at a given streamwise location should be identical. Using this principle, the position of the cone is adjusted in fine increments until the second-mode frequencies are nearly identical. The PCB sensor locations that were used to align the cone were located 255 mm downstream of the nosetip and are spaced in 90° azimuthal increments. These are shown in Figure 4.1a. A second-mode instability was not measured at the maximum quiet pressure of 160 psia, so the alignment technique was performed under noisy flow at a stagnation pressure of 77 psia. This equates to a freestream Reynolds number of 5.66×10^6 /m. The power spectra of the measured pressure fluctuations after adjustments were made are shown in Figure 4.1b. The second-mode peak frequency was approximated as the maximum of a parabolic fit between 200 kHz and 275 kHz. After aligning the cone, the second-mode peak frequencies at the sensor locations were aligned to a 232 kHz peak frequency. The peak frequencies are within ±2 kHz. Stability computations of second-mode peak frequencies on a sharp 7° half-angle cone by Mullen et al. show a sensitivity of 52.7 kHz per degree [25]. Using this, it is estimated that the cone has a residual 0.015° angle of attack.

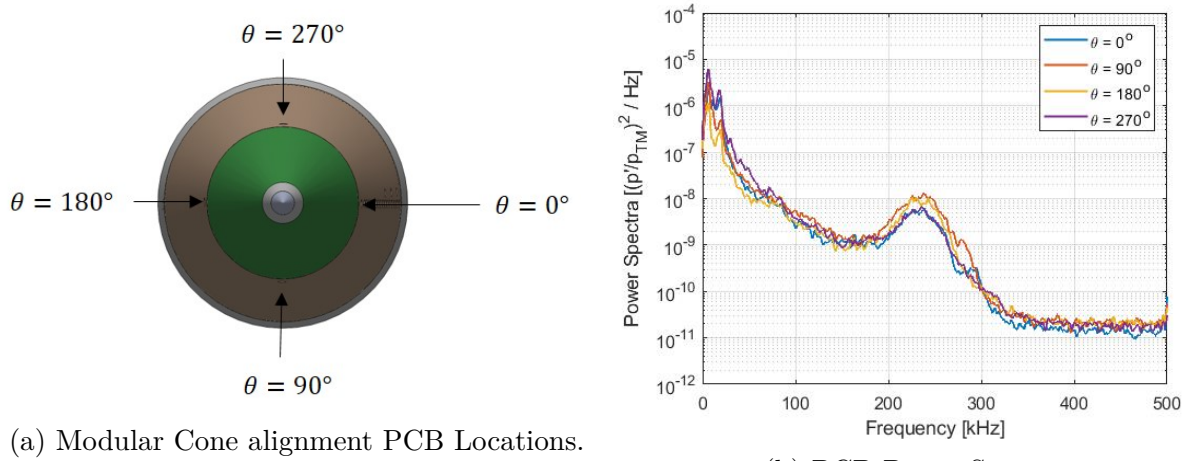

(a) Modular Cone alignment PCB Locations.

(b) PCB Power Spectra.

Figure 4.1. Second-mode alignment technique. After adjustments, each second-mode is aligned about a 232 kHz peak. Re = 5.66 × 10^6 /m.

4.1.2 Baseline Measurements with the Smooth-Wall Geometry

After the cone was aligned, several runs were performed with the smooth-wall insert to establish a baseline flow. The runs were performed in quiet flow and at different initial stagnation pressures to achieve a range of freestream Reynolds numbers. At the time of the experiments, the maximum quiet pressure was equivalent to a freestream Reynolds number of approximately 11 × 10^6 /m. A heating contour that is plotted with the laminar-scaled Stanton number is shown in Figure 4.2a. IR thermography measurements were limited to the aft end of the cone due to the size of the porthole window. The heating magnitudes from the runs at different freestream Reynolds numbers are compared along a streamwise cut of heat transfer. The location of the streamwise cut is shown in Figure 4.2a, and the streamwise cuts from each of these runs are plotted in Figure 4.2b. Between Re = 7.24 × 10^6 /m and 9.87 × 10^6 /m, the heating magnitudes were similar and appeared to slowly decrease along the cone. The heating profiles collapse onto similar values, suggesting that the boundary layer was laminar. An elevated heating magnitude was measured at Re = 11 × 10^6 /m. The streamwise profile does not exhibit any sharp increases that would be indicative of transition. The exact cause of the elevated heating magnitudes is unknown, but could potentially be caused by IR processing errors.

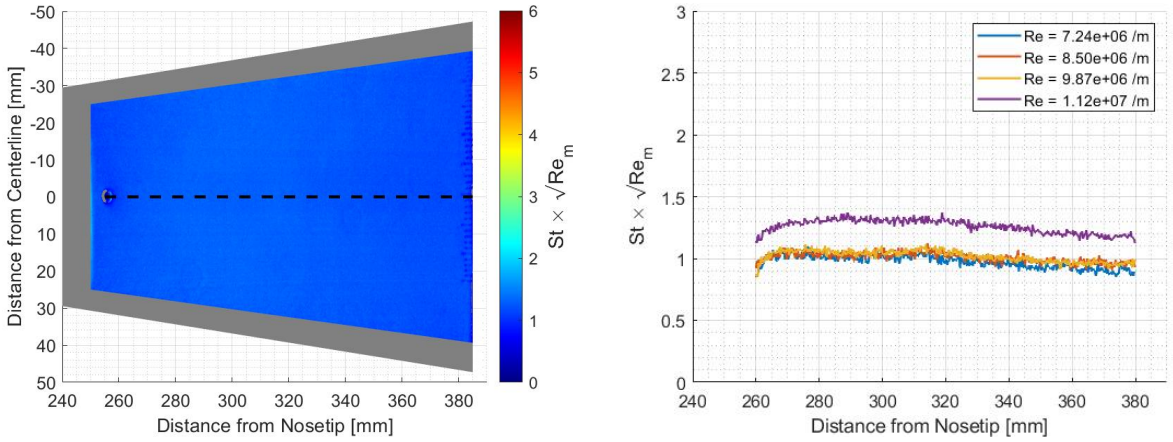

(a) Scaled heating contour at Re = 11 × 10^6 /m. (Run 18)

(b) Streamwise cuts at different Re. (Runs 15 through 18)

Figure 4.2. Baseline heating characteristics on the Modular Cone at $\alpha = 0°$.

Pressure fluctuations along the cone were minimal at the different freestream Reynolds numbers. Power spectra of pressure fluctuations along the cone at the lowest and highest freestream Reynolds numbers that were tested are shown in Figure 4.3. The electronic noise is also plotted in black and was calculated just before the run when there was no flow. Both power spectra show that the measured frequency content was near the electronic noise. Some frequency content was measured at the individual sensor locations, such as the low-frequency hump at x = 353.6 mm in Figure 4.3a and the small 250 kHz peak at x = 378.8 mm in Figure 4.3b. This suggests that there were some small disturbances in the flow. However, there was no clear indication of an instability that was consistently growing along the cone. The minimal pressure fluctuations confirm that the flow is laminar with the smooth-wall insert at these freestream Reynolds numbers.

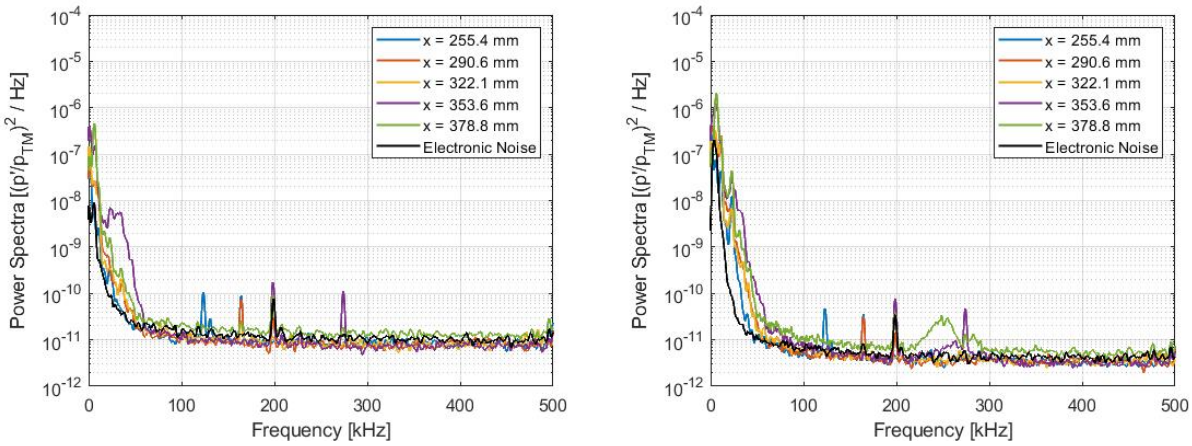

(a) Re = 7.2×10^6 /m. (Run 17) (b) Re = 11.2×10^6 /m. (Run 18)

Figure 4.3. Baseline power spectra along the Modular Cone at $\alpha = 0°$.

4.1.3 Measurements with Forward-Facing Steps

Runs with the forward-facing steps were performed by removing the nosetip and replacing the insert. The model frustum was not adjusted to maintain the nominal 0.0° angle of attack. For each insert, runs were performed at the different freestream Reynolds numbers that were tested with the smooth-wall insert. This was done to enable a comparison of different step heights at different freestream Reynolds numbers, and to identify any changes in the measurements as the freestream Reynolds number changes.

The heating magnitudes from the runs at the maximum quiet pressure are compared along a streamwise profile in Figure 4.4. The streamwise heating profiles with the different-sized forward-facing steps are similar to the baseline smooth-wall measurement. The heating magnitude slowly decreases along the cone, and no sharp increases in heating were observed that would be indicative of transition. This suggests that the forward-facing steps did not trip the flow.

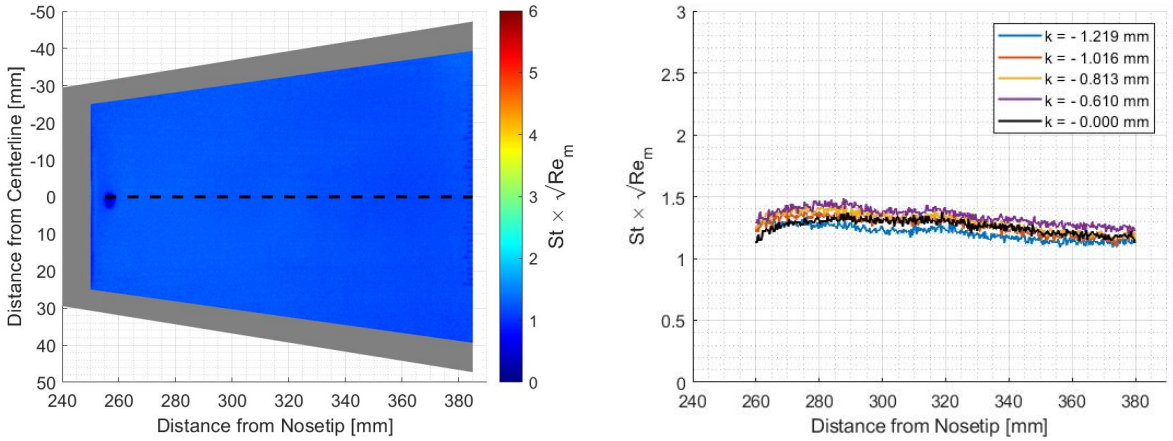

(a) Scaled heating contour. k = - 1.219 mm. (Run 28)

(b) Streamwise heating with the forward-facing steps.

Figure 4.4. Heating along the Modular Cone with forward-facing steps at $\alpha = 0°$ and Re $= 11 \times 10^6$ /m.

Pressure fluctuations along the cone were elevated when the forward-facing steps were present. The power spectra of pressure fluctuations along the cone with each step are plotted in Figure 4.5. In each power spectra, a peak frequency that is centered near 250 kHz can be seen. This peak is representative of an instability in the boundary layer. The amplitude of the peak frequency increases along the cone, and the peak frequency decreases along the cone. The peak frequency and growth along the cone are similar to a second-mode instability.

Additional frequency content can also be seen in the power spectra. With the 1.016 mm step, there is additional frequency content that is concentrated around 75 kHz. With the 1.219 mm step, there is additional frequency content between 400 kHz and 500 kHz. This suggests that there are other instabilities occurring in the boundary layer.

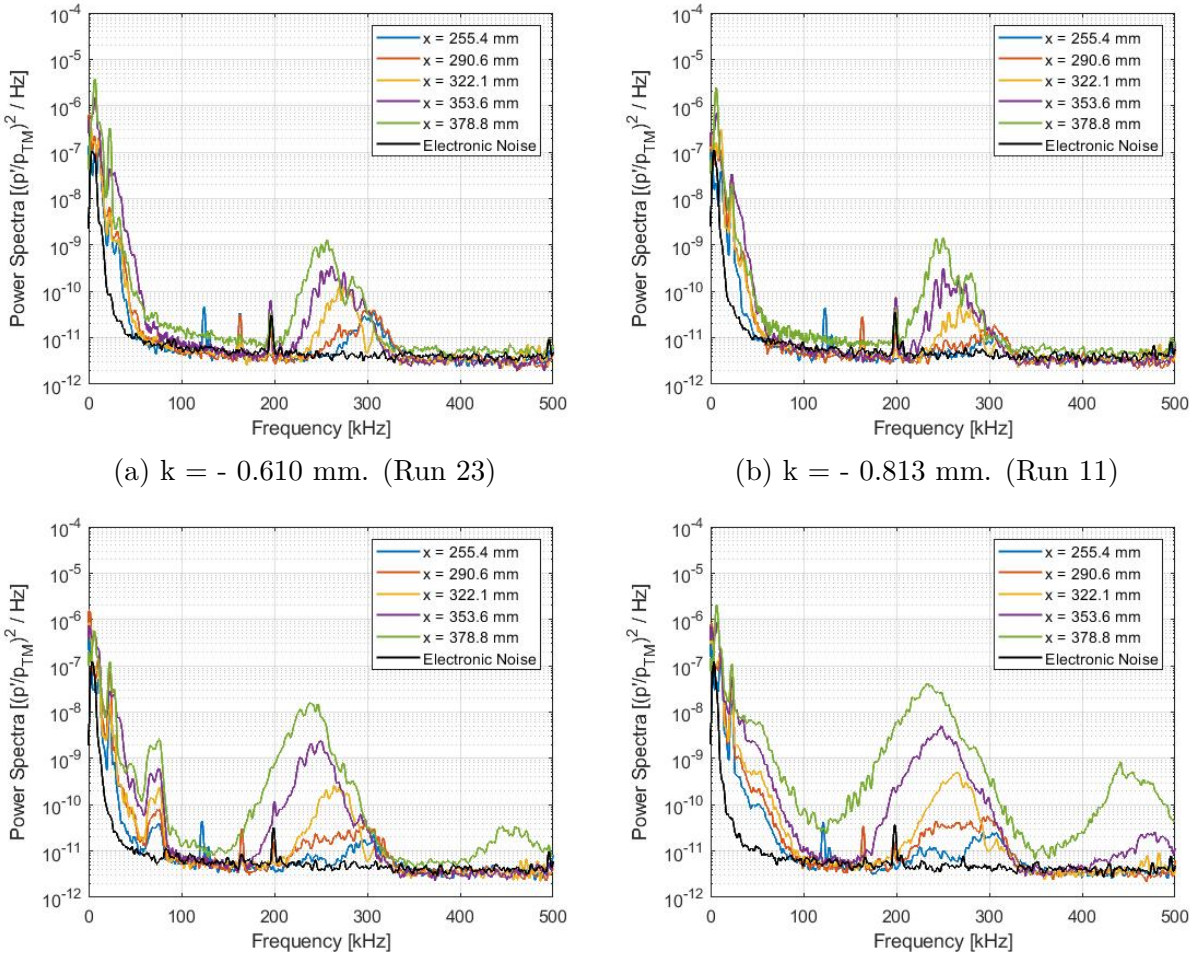

(a) k = - 0.610 mm. (Run 23)

(b) k = - 0.813 mm. (Run 11)

(c) k = - 1.016 mm. (Run 19)

(d) k = - 1.219 mm. (Run 07)

Figure 4.5. PSD along the Modular Cone with forward-facing steps at Re = 11.2×10^6 /m and $\alpha = 0°$.

The magnitude of the instability near 250 kHz can be represented as the RMS of the pressure fluctuations contained between 150 kHz and 350 kHz. These RMS pressure fluctuations were calculated as the square root of the integral of the power spectra. The RMS pressure fluctuations at Re = 11.2×10^6 /m are plotted on a logarithmic scale in Figure 4.6. There appears to be a linear trend between 300 mm and 380 mm for all the steps. This suggests that the instability follows an e^N-type growth. A linear fit is plotted as dotted lines, and the slopes of the linear fits are also provided in Figure 4.6. A higher slope was calculated with the larger step, which indicates that the larger step results in a higher growth rate.

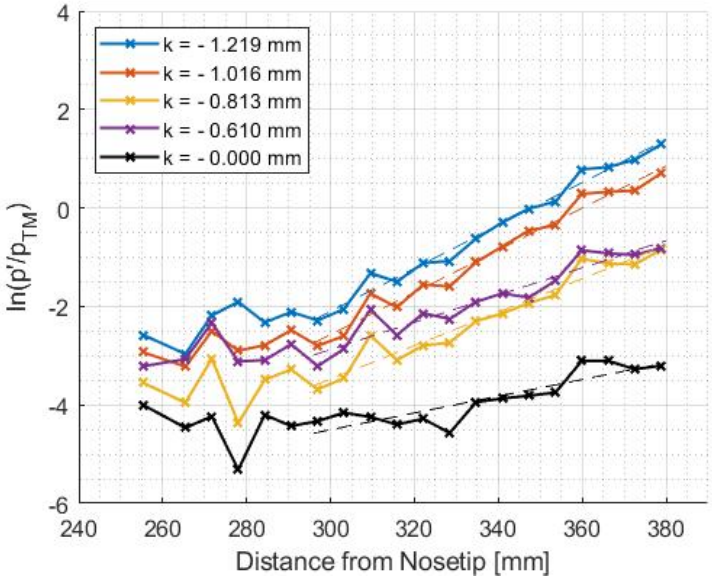

Step Height	Slope
- 1.219 mm	0.0436 mm^{-1}
- 1.016 mm	0.0427 mm^{-1}
- 0.813 mm	0.0340 mm^{-1}
- 0.610 mm	0.0277 mm^{-1}
- 0.000 mm	0.0170 mm^{-1}

Figure 4.6. RMS pressure fluctuations along the Modular Cone at Re = 11.2 $\times$ 10^6 /m and $\alpha = 0°$.

Experiments with the forward-facing steps were also performed at lower Reynolds numbers. Pressure fluctuation data along the cone were obtained at freestream Reynolds numbers of 9.9 $\times$ 10^6 /m, 8.5 $\times$ 10^6 /m, and 7.2 $\times$ 10^6 /m. The 250 kHz instability was still measured, although at a lower amplitude. In general, the lower freestream Reynolds number results in a lower amplitude of the instability. The power spectra from these runs are provided in Figures 4.7, 4.8, and 4.9. The peak frequency decreases along the cone, and the amplitude of the power spectra increases along the cone. At the lowest freestream Reynolds number of 7.2 $\times$ 10^6 /m, the instability is not clearly identifiable in the power spectra.

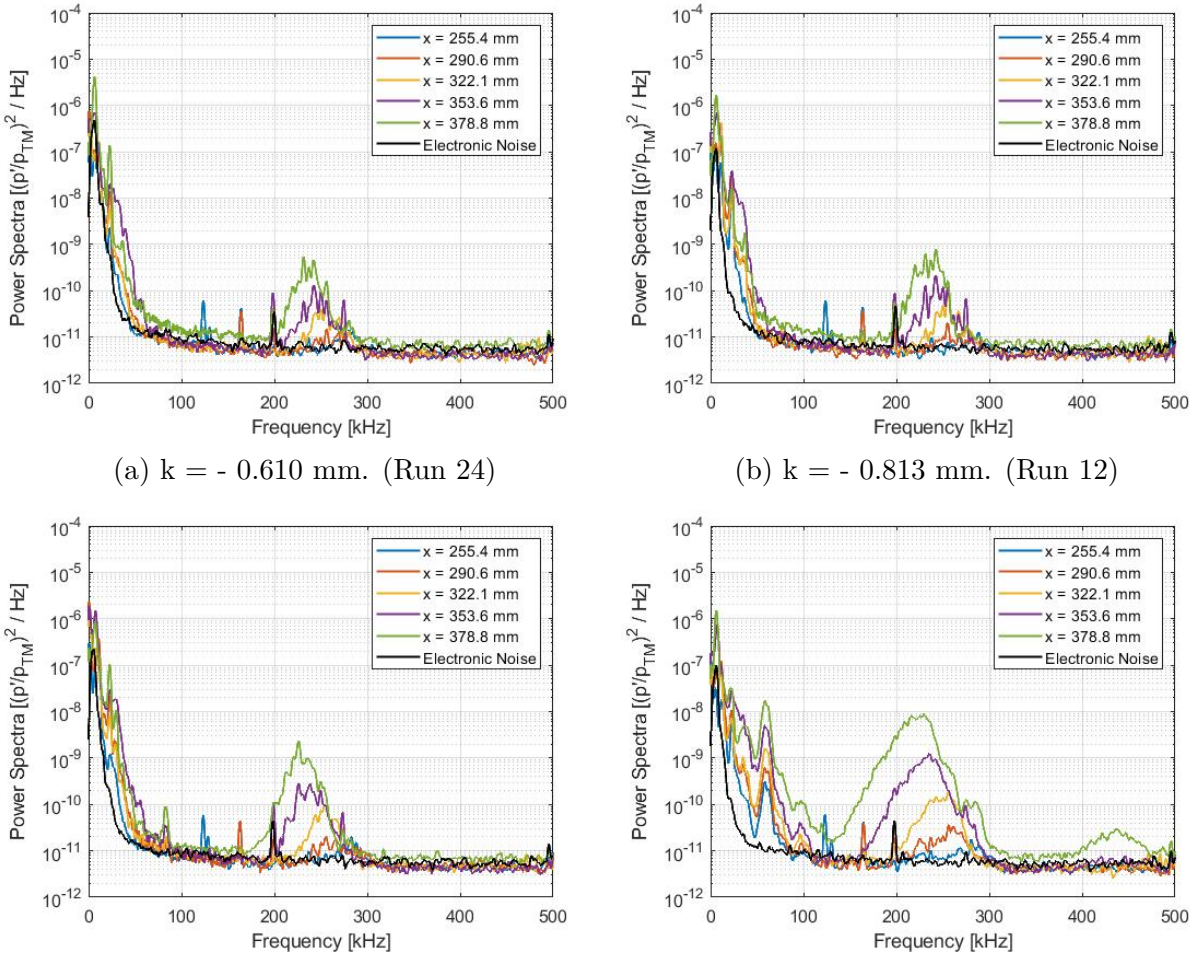

(a) k = - 0.610 mm. (Run 24)

(b) k = - 0.813 mm. (Run 12)

(c) k = - 1.016 mm. (Run 20)

(d) k = - 1.219 mm. (Run 08)

Figure 4.7. PSD along the Modular Cone with forward-facing steps at Re = 9.9×10^6 /m and $\alpha = 0°$.

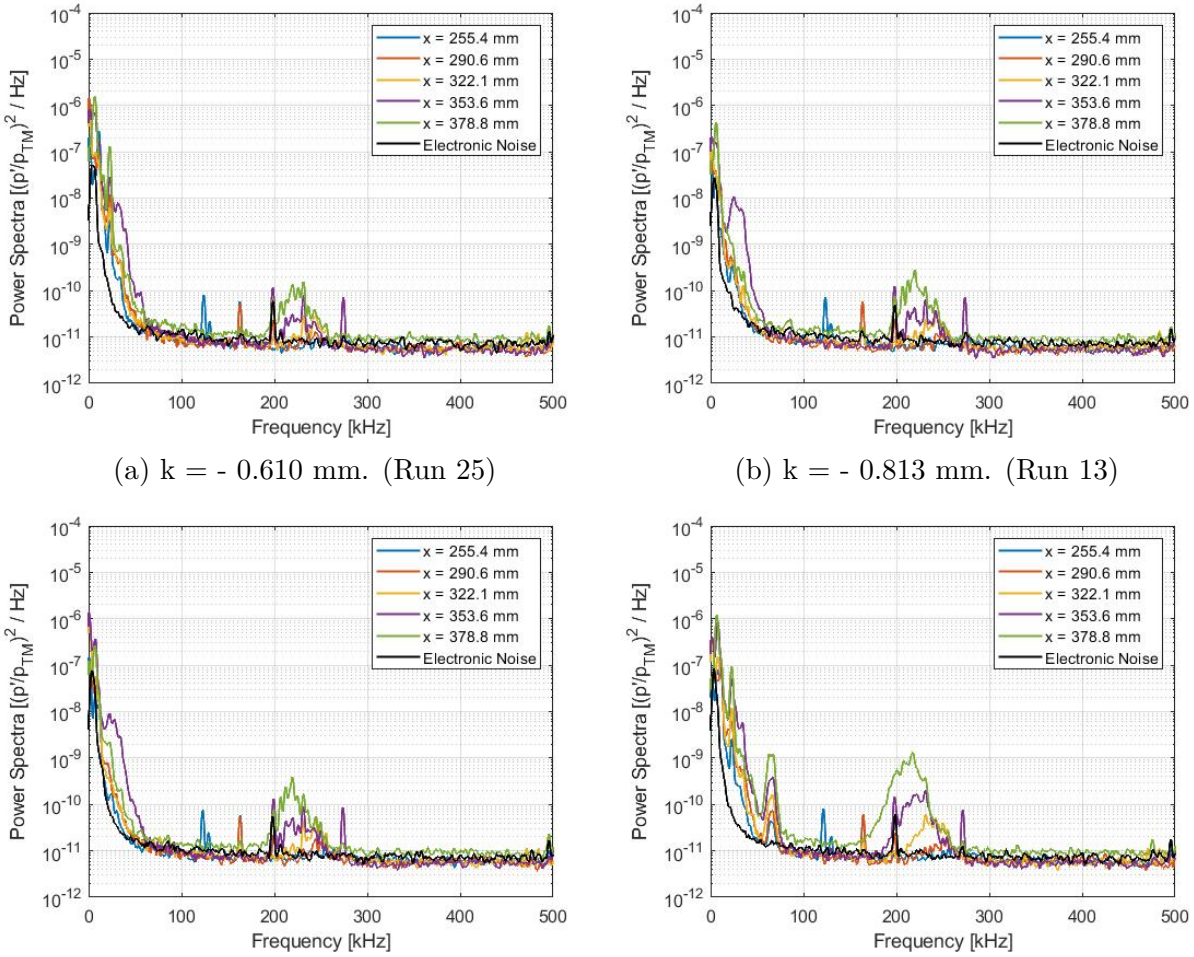

(a) k = - 0.610 mm. (Run 25)

(b) k = - 0.813 mm. (Run 13)

(c) k = - 1.016 mm. (Run 21)

(d) k = - 1.219 mm. (Run 09)

Figure 4.8. PSD along the Modular Cone with forward-facing steps at Re = 8.5×10^6 /m and $\alpha = 0°$.

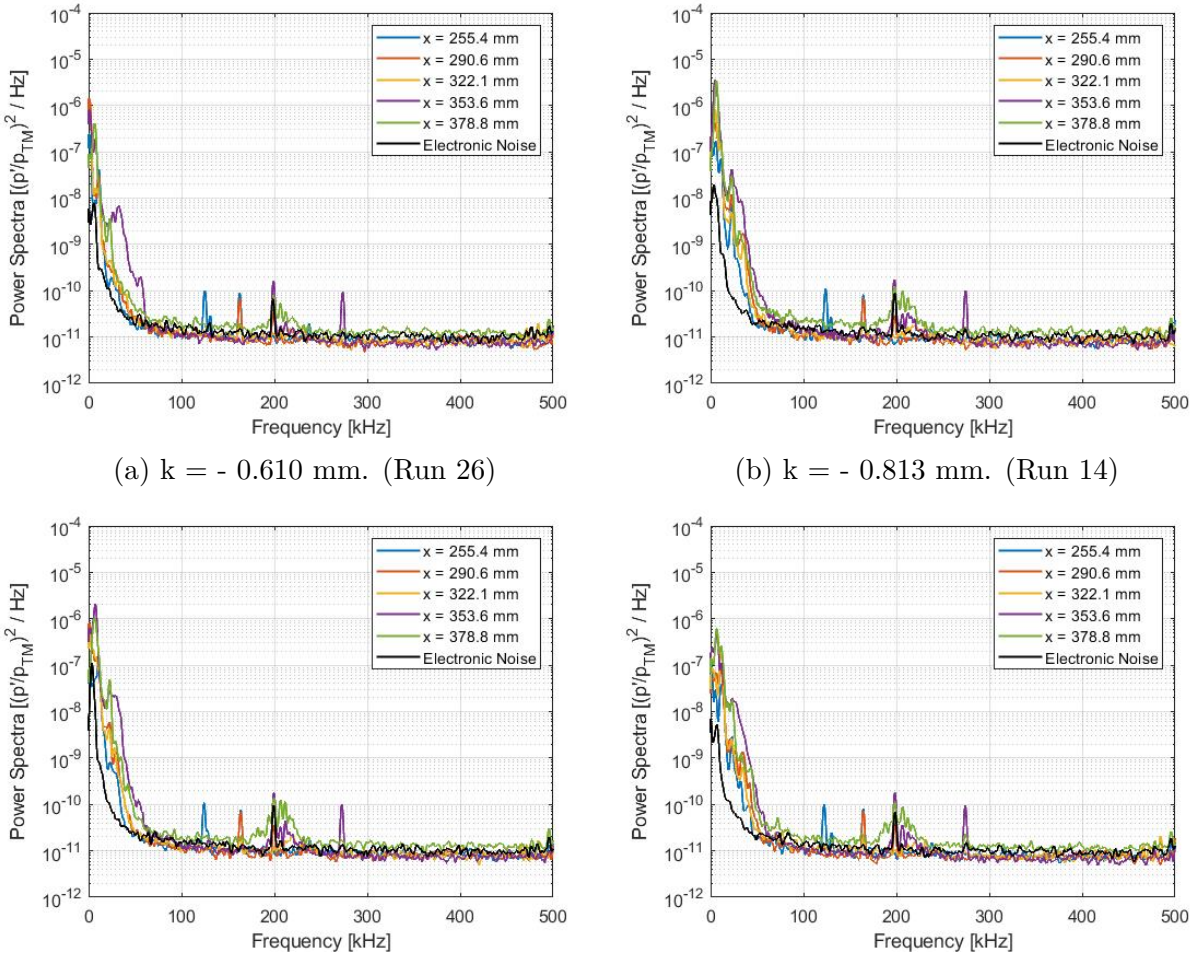

(a) k = - 0.610 mm. (Run 26)

(b) k = - 0.813 mm. (Run 14)

(c) k = - 1.016 mm. (Run 22)

(d) k = - 1.219 mm. (Run 10)

Figure 4.9. PSD along the Modular Cone with forward-facing steps at Re = 7.2×10^6 /m and $\alpha = 0°$.

The RMS pressure fluctuations were calculated from the power spectra at each freestream Reynolds number and plotted in Figures 4.10, 4.11, and 4.12. The linear trend between 300 mm and 380 mm downstream of the nosetip is still apparent at each freestream Reynolds number, but the slope of the linear trend decreases as the freestream Reynolds numbers decrease. At the lowest freestream Reynolds number of 7.2 $\times$ 10^6 /m, the RMS pressure fluctuation magnitudes along the cone depend only slightly on the roughness height and start to collapse onto a profile similar to the measurement with no step.

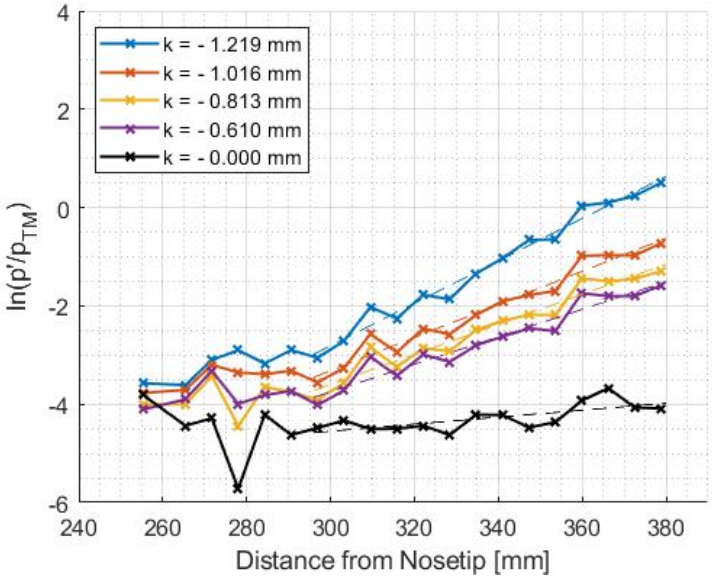

Step Height	Slope
- 1.219 mm	0.0431 mm^{-1}
- 1.016 mm	0.0337 mm^{-1}
- 0.813 mm	0.0306 mm^{-1}
- 0.610 mm	0.0280 mm^{-1}
- 0.000 mm	0.0071 mm^{-1}

Figure 4.10. RMS pressure fluctuations along the Modular Cone at Re = 9.9 $\times$ 10^6 /m and $\alpha = 0°$.

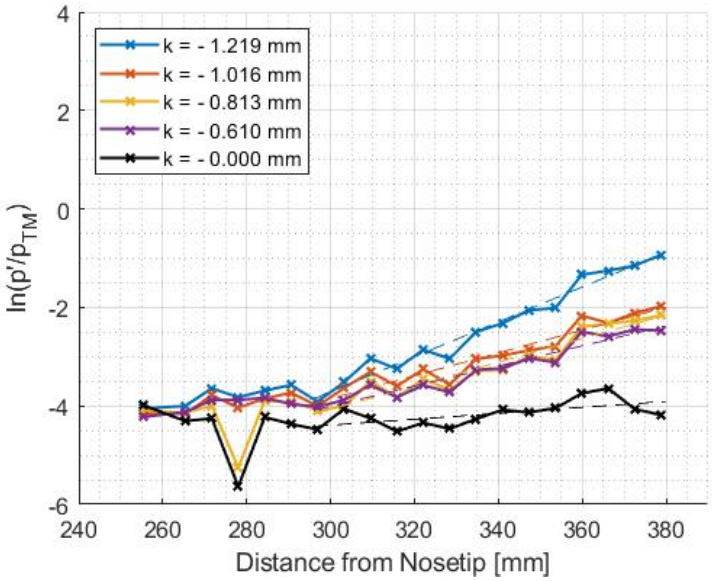

Step Height	Slope
- 1.219 mm	0.0355 mm^{-1}
- 1.016 mm	0.0232 mm^{-1}
- 0.813 mm	0.0240 mm^{-1}
- 0.610 mm	0.0204 mm^{-1}
- 0.000 mm	0.0060 mm^{-1}

Figure 4.11. RMS pressure fluctuations along the Modular Cone at Re = 8.5 $\times$ 10^6 /m and $\alpha = 0°$.

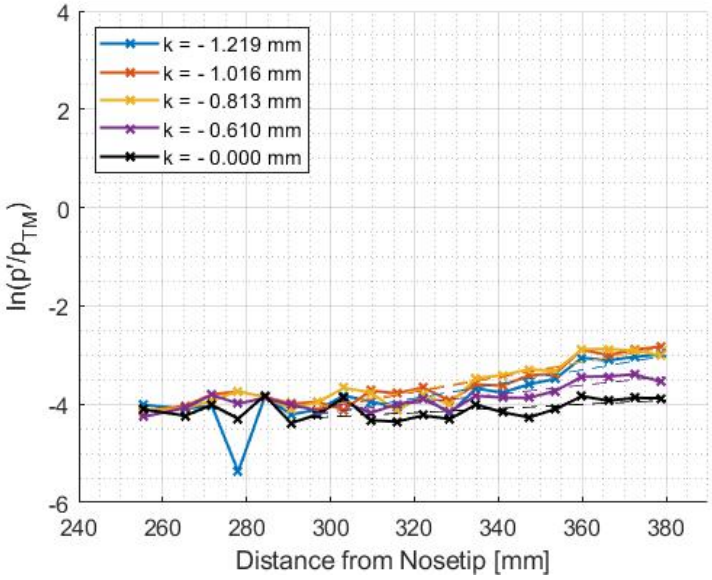

Step Height	Slope
- 1.219 mm	0.0145 mm^{-1}
- 1.016 mm	0.0153 mm^{-1}
- 0.813 mm	0.0147 mm^{-1}
- 0.610 mm	0.0091 mm^{-1}
- 0.000 mm	0.0042 mm^{-1}

Figure 4.12. RMS pressure fluctuations along the Modular Cone at Re = 7.2 $\times$ 10^6 /m and $\alpha = 0°$.

4.1.4 Measurements with Backward-Facing Steps

Only the largest 1.219 mm and 1.016 mm backward-facing steps were tested. Neither resulted in a substantial increase in heating nor elevated pressure fluctuations when compared to the smooth-wall measurement. A comparison along a streamwise slice of heating at the maximum quiet pressure is plotted in Figure 4.13. The power spectra from pressure

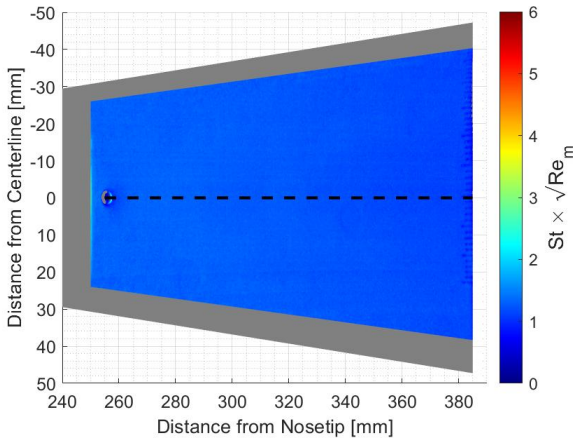

(a) Scaled heating contour. k = + 1.219 mm. (Run 28)

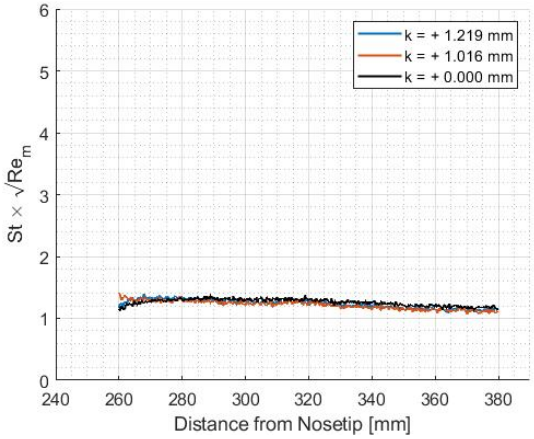

(b) Streamwise cuts of heating.

Figure 4.13. Heating along the Modular Cone with the largest backward-facing steps at Re = 11.2 × 10^6 /m and $\alpha = 0°$.

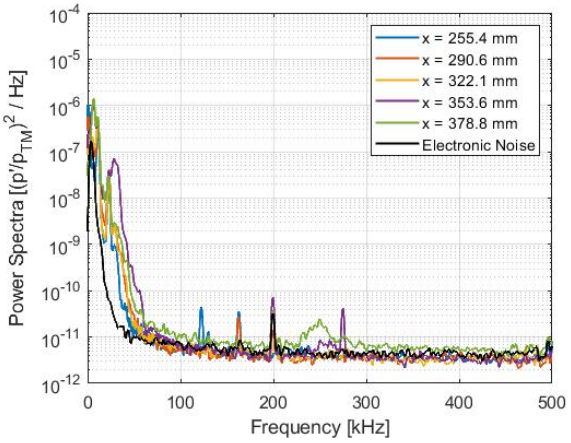

(a) k = + 1.016 mm. (Run 31)

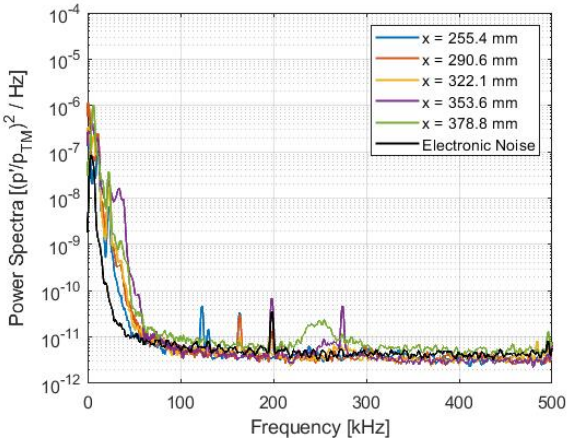

(b) k = + 1.219 mm. (Run 28)

Figure 4.14. Power spectra along the Modular Cone with the largest backward-facing steps at Re = 11.2 × 10^6 /m and $\alpha = 0°$.

fluctuations along the cone with the two backward-facing steps installed are shown in Figure 4.14. The lack of additional frequency content suggests that the backward-facing steps did not introduce a measurable disturbance into the flow at these conditions. Because of this, runs were not performed at the lower freestream Reynolds number or with the smaller backward-facing steps.

4.2 Measurements at $\alpha = 6°$

The cone was pitched at a 6° angle of attack in an attempt to observe an increase in the surface heating magnitudes. A fixed 6° angle-of-attack adapter that was precision machined was used to pitch the model. The same adapter was used in experiments by Edelman, and a drawing of the adapter design can be found in Appendix H of Reference [26]. The adapter is estimated to be accurate within ±0.20°. IR thermography measurements and PCB measurements were obtained on the windward ray, where the boundary layer was the thinnest.

4.2.1 Baseline Measurements with the Smooth-Wall Geometry

A baseline flow was first established on the windward ray of the cone at a 6° angle of attack. Because the flow was no longer axisymmetric, two runs were needed to obtain IR thermography and pressure fluctuation measurements on the windward ray. First, a run was performed with the sensor ray rotated out of view so that the IR thermography image was not contaminated with sensor faces. Then, another run at similar tunnel conditions was performed with the sensor ray rotated onto the windward ray. This results in a small difference between the freestream Reynolds numbers.

Heating magnitudes along the windward ray from several runs at different freestream Reynolds numbers are plotted in Figure 4.15. At the different Reynolds numbers, the heating magnitudes are similar. The heating magnitudes appear to slowly decrease in the downstream direction, suggesting that the boundary layer was laminar on the windward ray. Pressure fluctuation measurements on the windward ray also reflect this. The PSD plots of the pressure fluctuations along the cone at the lowest and highest Reynolds numbers that

were tested are shown in Figure 4.16. At the lowest freestream Reynolds number, frequency content was near the electronic noise. No growth in the power spectra was observed along the cone. At the highest freestream Reynolds number, there was some increase in broadband magnitudes below 150 kHz. This suggests that there were some disturbances growing in the boundary layer.

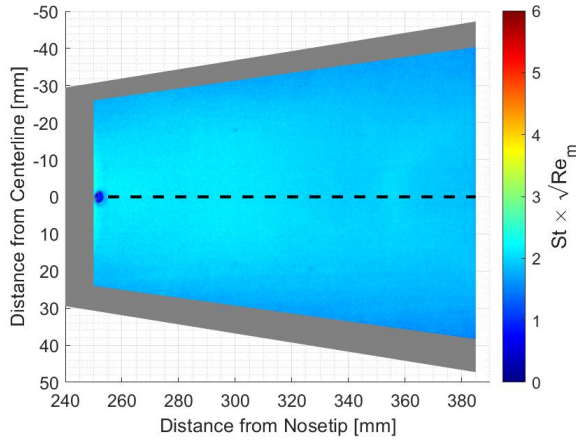

(a) Scaled heating contour at Re = 9.74 × 10^6 /m. (Run 94)

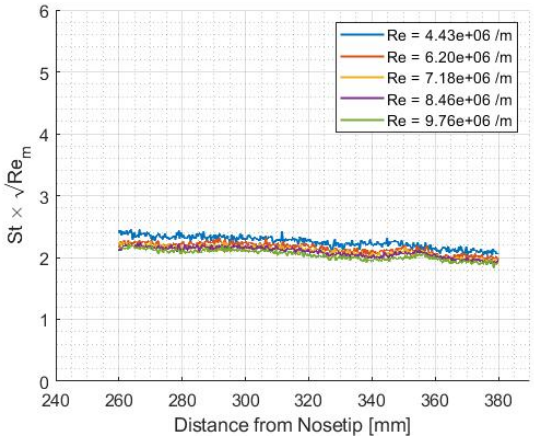

(b) Streamwise cuts at different Re.

Figure 4.15. Heating along the Modular Cone with the smooth-wall insert at $\alpha = 6°$.

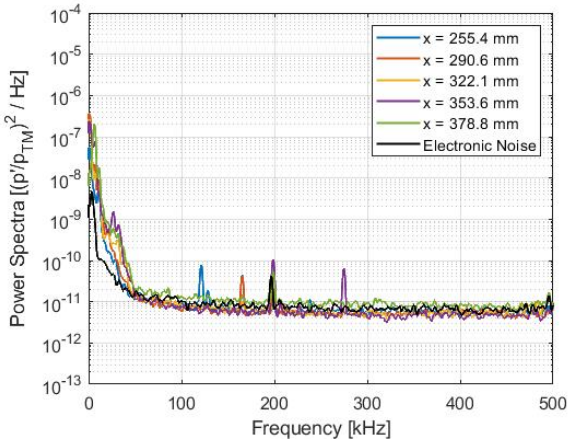

(a) Re = 4.51 × 10^6 /m. (Run 59)

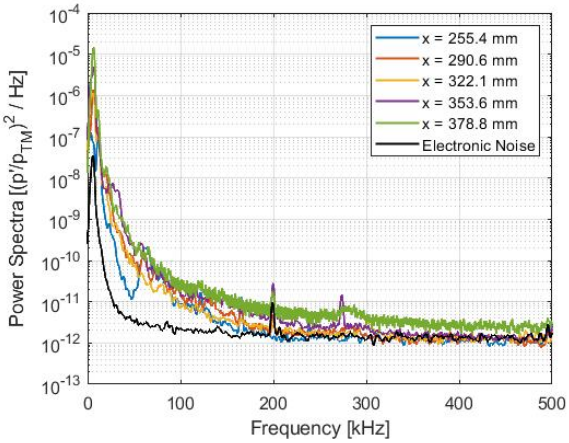

(b) Re = 9.88 × 10^6 /m. (Run 60)

Figure 4.16. Power spectra along the Modular Cone with the smooth-wall insert at $\alpha = 6°$.

4.2.2 Measurements with Forward-Facing Steps

Runs with each forward-facing step were performed at a freestream Reynolds number near 6.2 $\times$ 10^6 /m. Scaled heating contours from these runs are shown in Figure 4.17. A visual increase in heating can be seen with the largest two forward-facing steps. Streamwise cuts of heating were extracted from each contour and plotted in Figure 4.18 to quantitatively compare the heating magnitudes along the windward ray. The 0.813 mm step results in a heat transfer profile that is nearly identical to the smooth-wall measurement. With the 1.016 mm step, the heating magnitude begins to increase above the smooth-wall measurement somewhere between x = 280 mm and x = 300 mm. With the largest 1.219 mm step, heating magnitudes are well above the smooth-wall measurement and continues to increase in the downstream direction.

A similar set of runs was performed at a higher freestream Reynolds number of 7.2 $\times$ 10^6 /m. Plots of the scaled heating contours and streamwise cuts of heating are shown in Figures 4.19 and 4.20, respectively. The effect of the steps on the heating magnitudes is magnified. The 0.813 mm step now results in an increase in heating, which departs from the smooth-wall measurement somewhere between x = 280 mm and x = 300 mm. The heating magnitudes with the 1.016 mm step is well above the smooth-wall measurement and increase to a maximum near x = 355 mm. A similar maximum was measured with the largest 1.219 mm step. This might indicate that the boundary layer is fully turbulent.

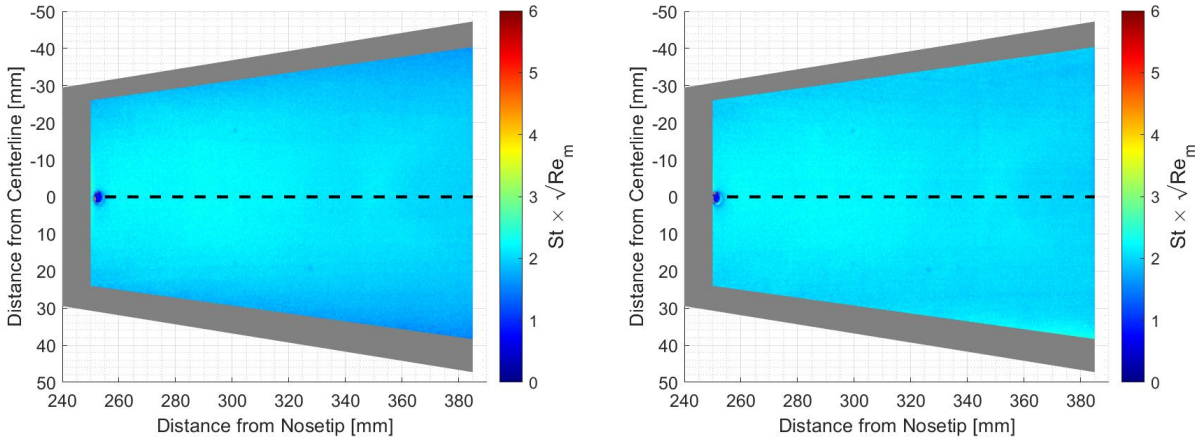

(a) k = - 0.000 mm. (Run 91)

(b) k = - 0.813 mm. (Run 83)

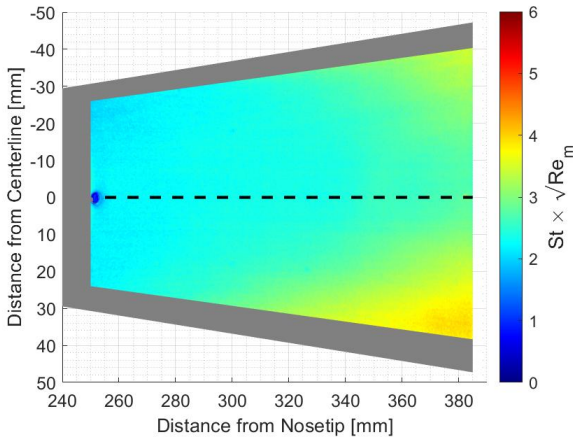

(c) k = - 1.016 mm. (Run 76)

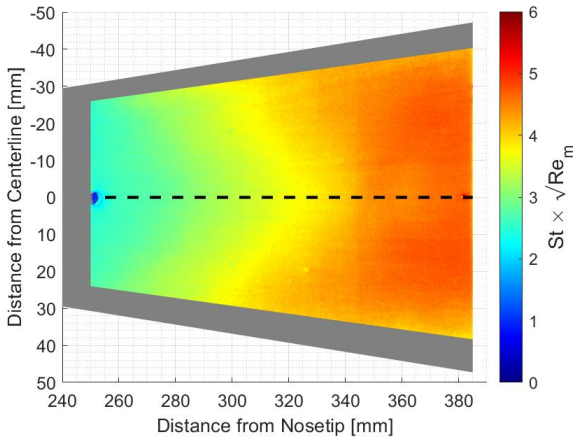

(d) k = - 1.219 mm. (Run 81)

Figure 4.17. Scaled heating contours with the forward-facing steps. Re = 6.2 × 10^6 /m.

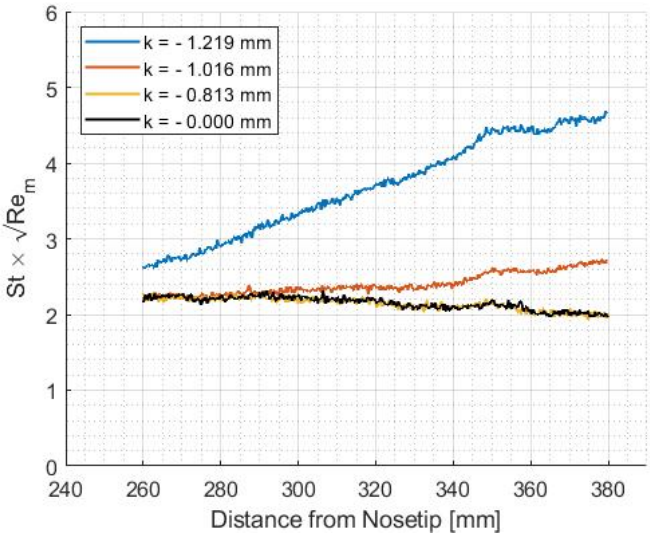

Figure 4.18. Heating along the windward ray of the Modular Cone with forward-facing steps installed at Re = 6.2 × 10^6 /m.

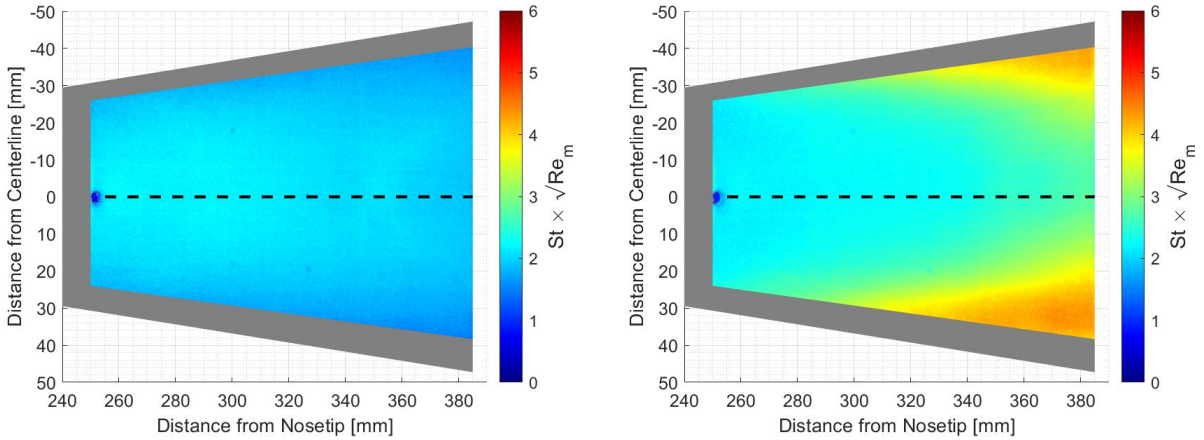

(a) k = - 0.000 mm. (Run 92)

(b) k = - 0.813 mm. (Run 84)

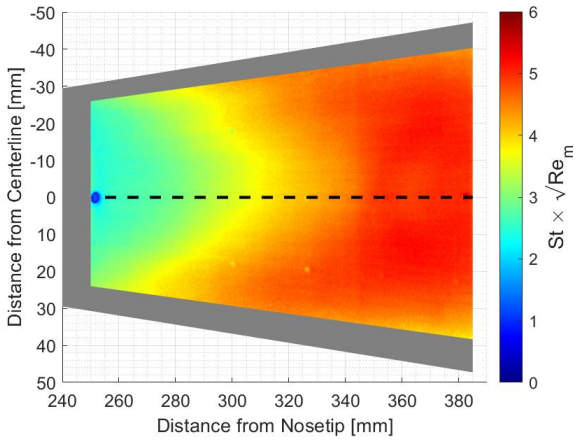

(c) k = - 1.016 mm. (Run 77)

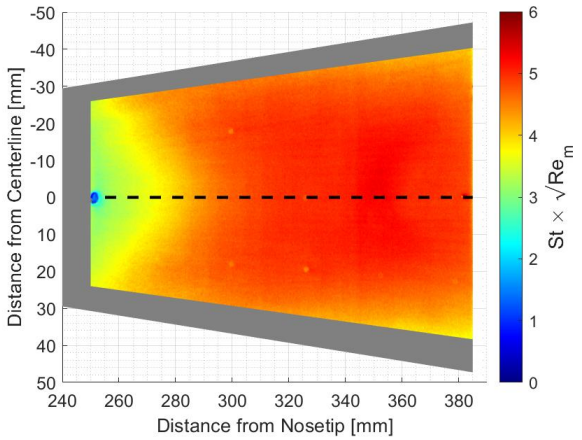

(d) k = - 1.219 mm. (Run 82)

Figure 4.19. Scaled heating contours with the forward-facing steps. Re = 7.2 × 10^6 /m.

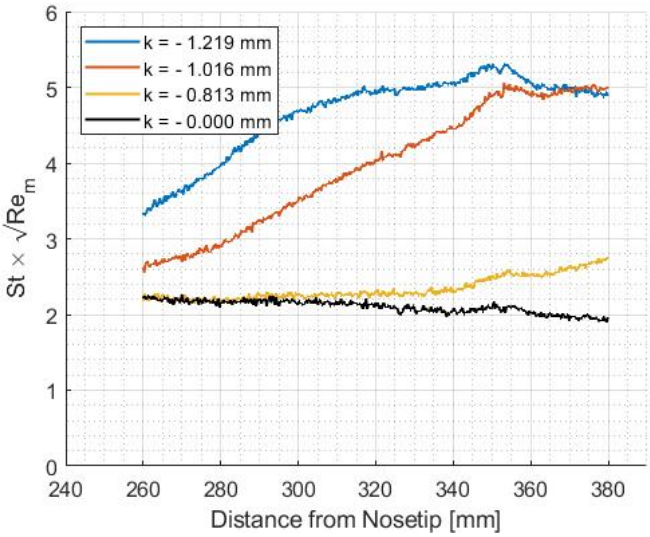

Figure 4.20. Heating along the windward ray of the Modular Cone with forward-facing steps at Re = 7.2 × 10^6 /m.

Increased pressure fluctuations were measured along the windward ray of the cone, however no instabilities were identified. The power spectra along the cone with each of the steps are shown in Figure 4.21 and Figure 4.22 at freestream Reynolds numbers of 6.2×10^6 /m and 7.2×10^6 /m, respectively.

At Re $= 6.2 \times 10^6$ /m, there is additional frequency content between 0 and 150 kHz that was not measured with the smooth-wall geometry. In the power spectra with the 0.813 mm step, Figure 4.21b, the amplitude of frequency content between 0 and 150 kHz does not vary much along the cone. A small amount of frequency content that is centered around a 300 kHz peak was measured at the aft end of the cone. This might represent an instability in the boundary layer, but there was no clear growth of the peak frequency along the cone. A broadband increase in frequency content was measured along the cone with the 1.016 mm and 1.219 mm steps. The RMS pressure fluctuation magnitudes are calculated between 11 kHz and 500 kHz and are shown in the legend. With the 1.016 mm and 1.219 steps, RMS pressure fluctuation magnitudes increase from about 4% to over 10% along the cone.

At Re $= 7.2 \times 10^6$ /m, the additional frequency content between 0 and 150 kHz was still measured with the steps. The 0.813 mm step now causes a measurable increase in pressure fluctuations, represented as the broadband increase in frequency content along the cone. Some peaks around 300 kHz are seen in the power spectra and could potentially represent an instability. RMS pressure fluctuation magnitudes with the 0.813 mm step rise to about 5% at the end of the cone. A higher amplitude and broadband power spectra were measured with the 1.016 mm and 1.219 mm steps. RMS pressure fluctuation magnitudes are between 10% and 12% at the end of the cone, likely representative of a turbulent flow.

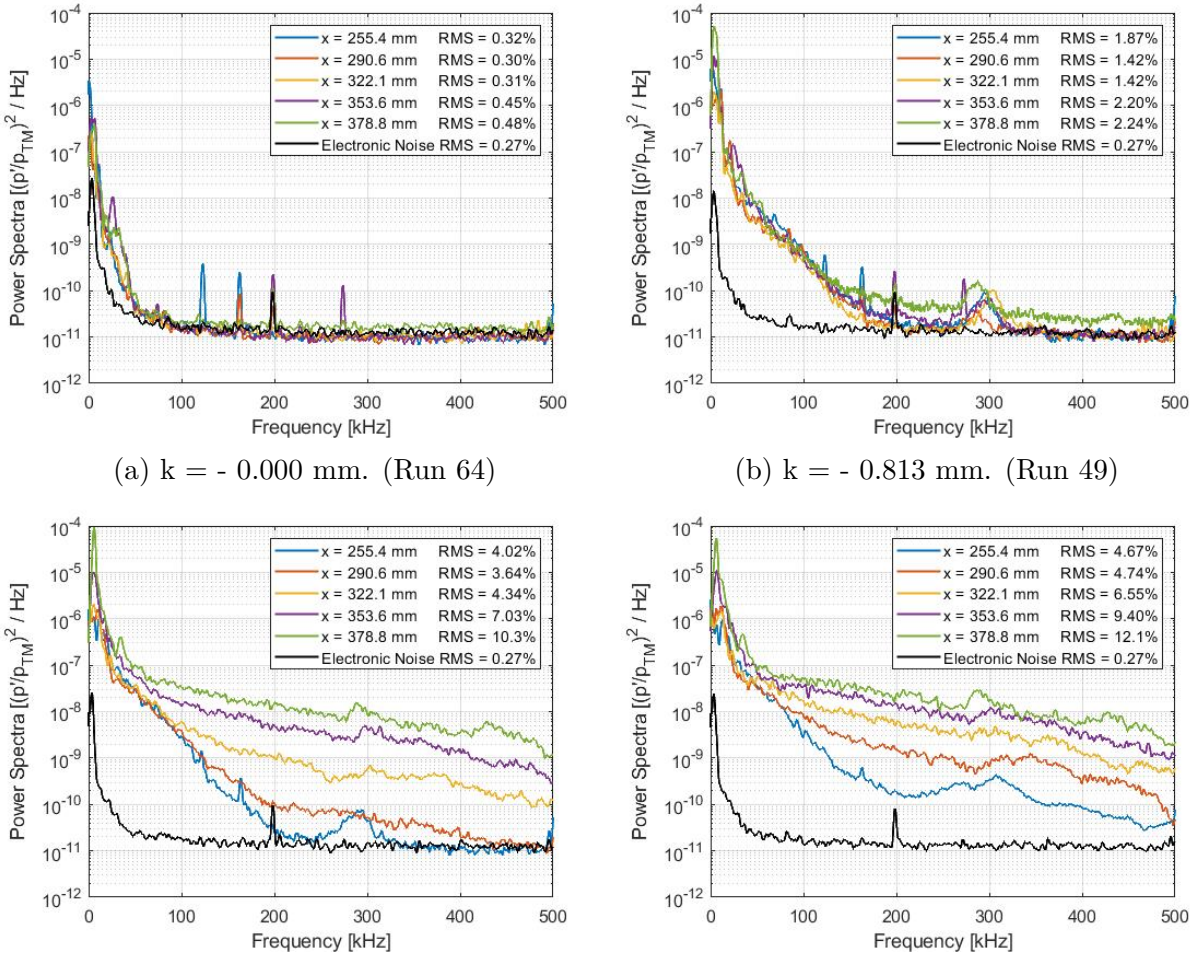

(a) k = - 0.000 mm. (Run 64)

(b) k = - 0.813 mm. (Run 49)

(c) k = - 1.016 mm. (Run 44)

(d) k = - 1.219 mm. (Run 42)

Figure 4.21. PSD along the Modular Cone with forward-facing steps. Re = 6.2×10^6 /m.

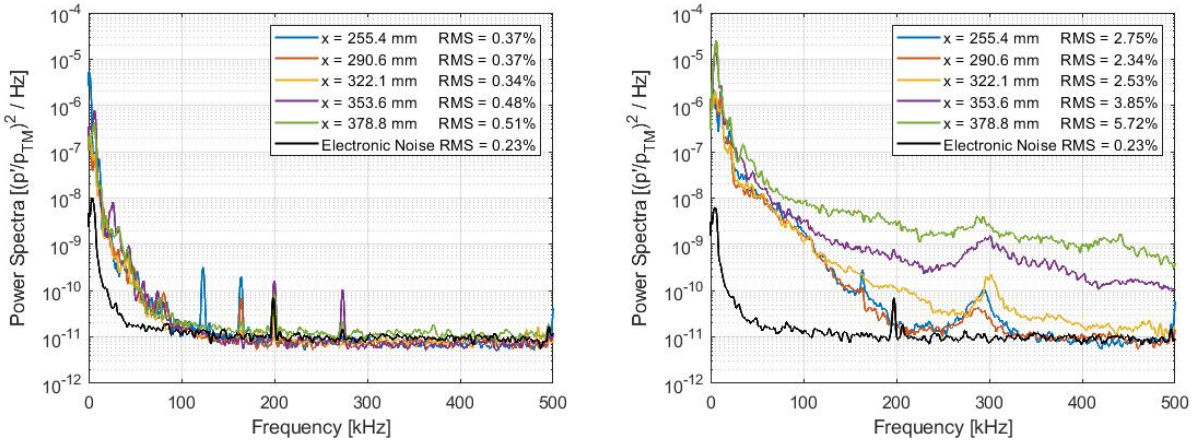

(a) k = - 0.000 mm. (Run 63)

(b) k = - 0.813 mm. (Run 50)

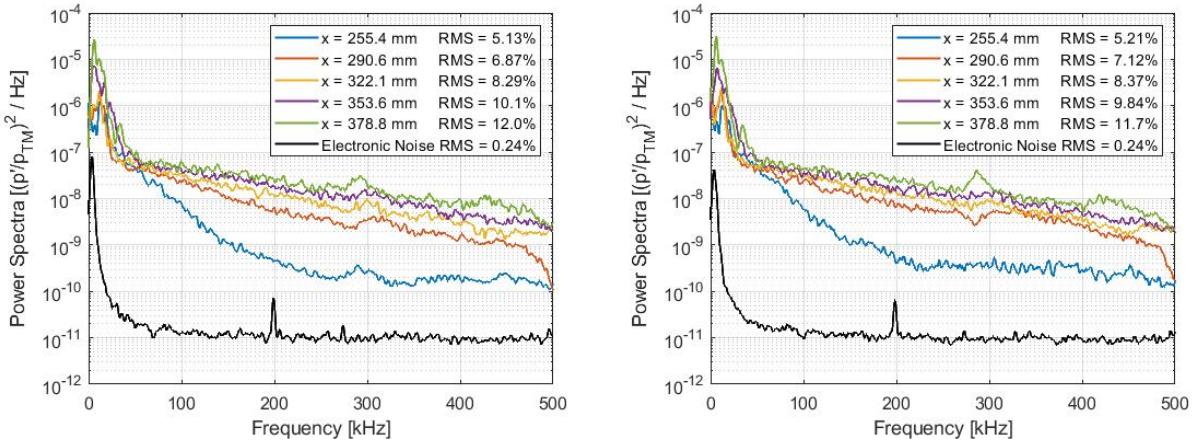

(c) k = - 1.016 mm. (Run 45)

(d) k = - 1.219 mm. (Run 41)

Figure 4.22. PSD along the Modular Cone with forward-facing steps. Re = 7.2×10^6 /m.

5. EXPERIMENTS WITH THE BOLT MODEL

5.1 Measurements at $\alpha = 0°$

The majority of experiments that are presented in this chapter were performed during Entry 3. The BOLT model was first positioned at a 0° angle of attack, and runs were performed with each nosetip without altering the position of the model. This was done to reduce the uncertainty that may be caused by small variations in the sting and model position. During Entry 3, the PEEK experiment surface was facing the north side of the BAM6QT. The stagnation pressure and temperature during each run at which data was processed are provided in Appendix B. The run number is provided for each Figure so that the corresponding stagnation conditions can be obtained.

5.1.1 Baseline Measurements

Measurements with the unpolished, smooth-wall nosetip were first performed to establish a baseline flow on the modified BOLT model. During the time of the experiments the maximum quiet pressure was around 134 psia. This equates to a freestream Reynolds number of 10×10^6 /m. Runs at this maximum quiet pressure were performed with and without the bleed slots activated to identify the effect of tunnel noise levels. The heat transfer contours seen in Figure 5.1 are plotted with the laminar-scaled Stanton number. The view of the PEEK experiment surface was limited to the downstream-half of the model due to the size of the CaF_2 porthole window. In quiet flow, laminar streaks with low heating magnitudes were measured. In noisy flow, two wedges with high heating magnitudes envelop most of the experiment surface.

Spanwise cuts of heating, located at x/L = 0.98 (x = 283 mm), were extracted from each of these runs and plotted in Figure 5.2 to quantitatively compare the heating magnitudes. The location of the spanwise cut is shown as the dotted black lines in Figure 5.1. At this slice location, the most prominent laminar streaks are located approximately ± 5 mm and ± 20 mm from the centerline. The peak heating magnitudes of these laminar streaks are between St $\times\sqrt{Re}$ = 1 and 2. In noisy flow, the peak heating magnitudes increase by a

factor of 2 – 4 and approach a value of $St \times \sqrt{Re} = 4$. The elevated heating magnitudes are representative of a turbulent flow. The sharp decrease in heating that is located beyond -40 mm from the centerline is caused by interference from the edge of the window.

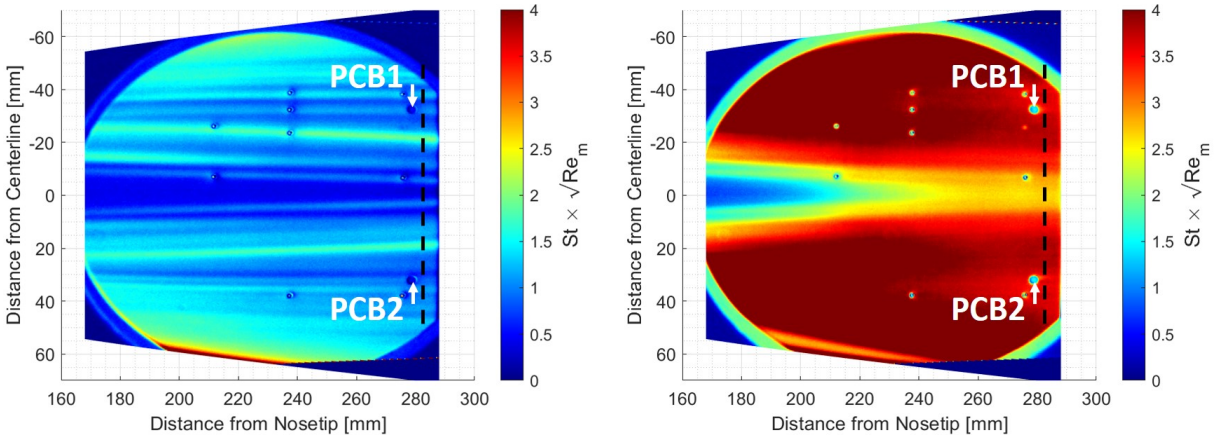

(a) Quiet Flow. (Run 10)

(b) Noisy Flow. (Run 22)

Figure 5.1. Scaled heating contours with the unpolished, smooth-wall nosetip in quiet and noisy flow. Re = 10.2 × 10^6 /m.

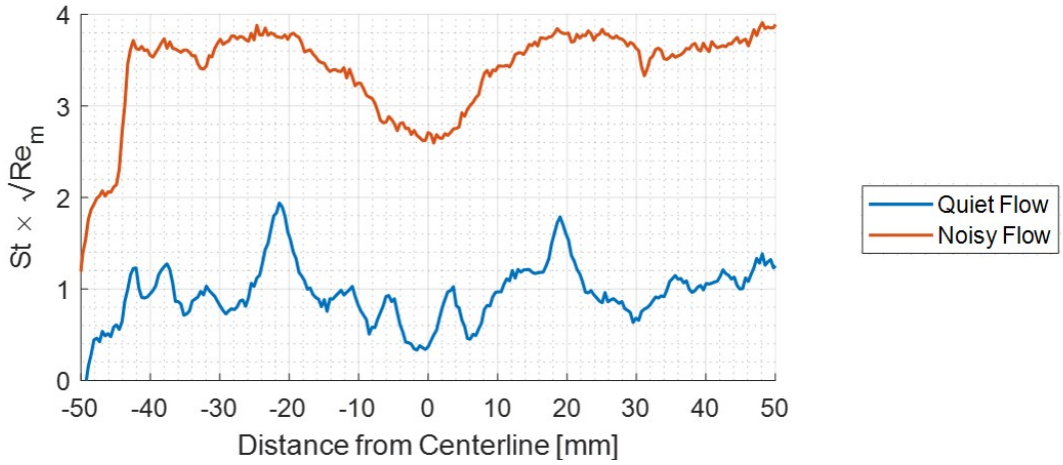

Figure 5.2. Spanwise cuts of heating at x/L = 0.98 (x = 283 mm) with the unpolished, smooth-wall nosetip in quiet and noisy flow. Re = 10.2 × 10^6 /m.

PCB1 and PCB2 are located at the aft end of the model and ± 38 mm from the centerline. The power spectra from the measured pressure fluctuations in quiet and noisy flow are plotted in Figure 5.3. The electronic noise, calculated just before the run when flow is off, is also plotted. The RMS of the pressure fluctuations are provided in the legend and were calculated by integrating between 11 kHz and 500 kHz. In quiet flow, the power spectra of both sensors are near the electronic noise. There is a small amount of frequency content between 11 kHz and 150 kHz, indicating that there were some fluctuations in the flow. A small, 275 kHz peak is seen in the PCB2 power spectra. The amplitude of the peak is less than an order of magnitude above the electronic noise. This might be representative of a small instability that is starting to grow in the boundary layer. In noisy flow, a high amplitude and broadband spectra are seen in both plots. The RMS pressure fluctuation magnitudes are above 10%. The broadband spectra and elevated pressure fluctuation magnitudes are indications of a turbulent flow.

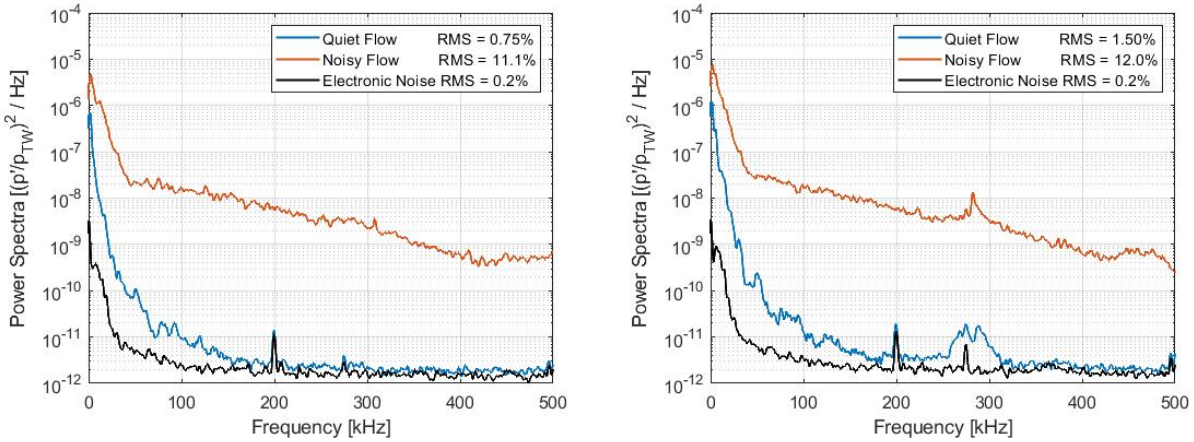

(a) PCB1 Power Spectra.

(b) PCB2 Power Spectra.

Figure 5.3. PCB1 and PCB2 power spectra with the unpolished, smooth-wall nosetip in noisy and quiet flow. Re = 10.2×10^6 /m.

The combination of a significantly elevated heating magnitude and higher pressure fluctuations is good evidence that the flow was turbulent in noisy flow. All subsequent runs were performed in quiet flow, where the transition from a laminar to a turbulent flow could be achieved. The noisy flow measurements are used as a notional reference point for a turbulent flow.

Four runs were performed with different stagnation pressures to identify the effect of Reynolds number. Freestream Reynolds numbers between 8×10^6 /m and 10×10^6 /m were achieved in these runs. Spanwise cuts of heating were extracted from these runs at x/L = 0.98 and plotted in Figure 5.4. The noisy flow measurement is also plotted as a reference for the heating magnitudes of a turbulent flow. The locations of the laminar streaks are consistent across the different freestream Reynolds numbers. However, the peak heating magnitudes of the laminar streaks appear to increase slightly at a higher freestream Reynolds number. When plotted with the laminar-scaled Stanton number, it is expected that the heating magnitudes would collapse onto a similar profile. The slight increase in the scaled heating magnitudes indicates that there was some degree of growth along the laminar streaks. However, the scaled heating magnitudes remain well below the noisy flow levels and are not representative of a turbulent flow.

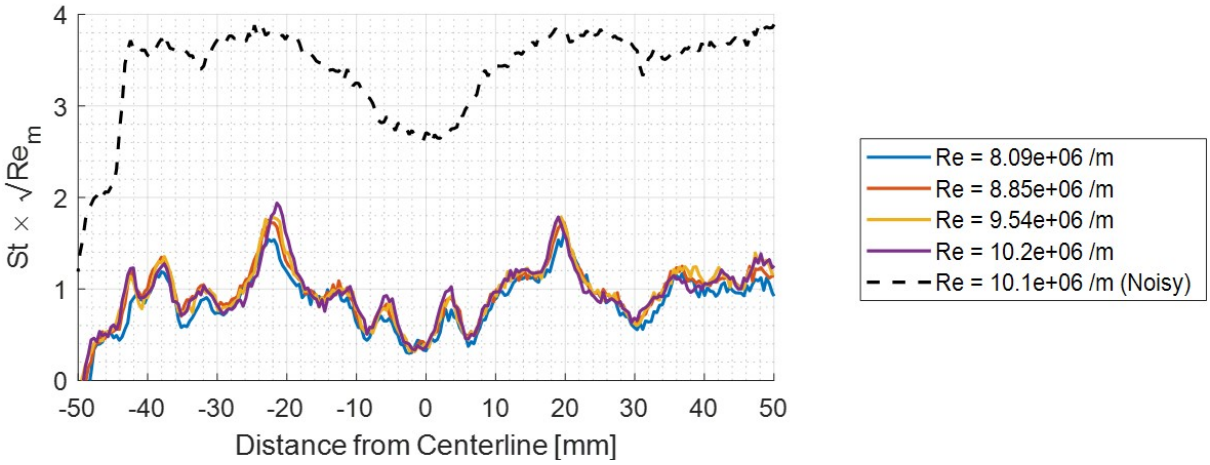

Figure 5.4. Spanwise cuts of heating at x/L = 0.98 (x = 283 mm) with the unpolished, smooth-wall nosetip at different freestream Reynolds numbers. (Runs 10 through 13)

The power spectra from the measured pressure fluctuations at PCB1 and PCB2 during these runs are plotted in Figure 5.5. The frequency content in the power spectra are similar across the different freestream Reynolds numbers and are near the electronic noise. This suggests that there was minimal growth in the boundary layer as the freestream Reynolds number increases. The small 275 kHz peak frequency was measured at PCB2, but only at the highest freestream Reynolds number of 10×10^6 /m. A significant instability does not appear to develop with the smooth-wall geometry under these conditions.

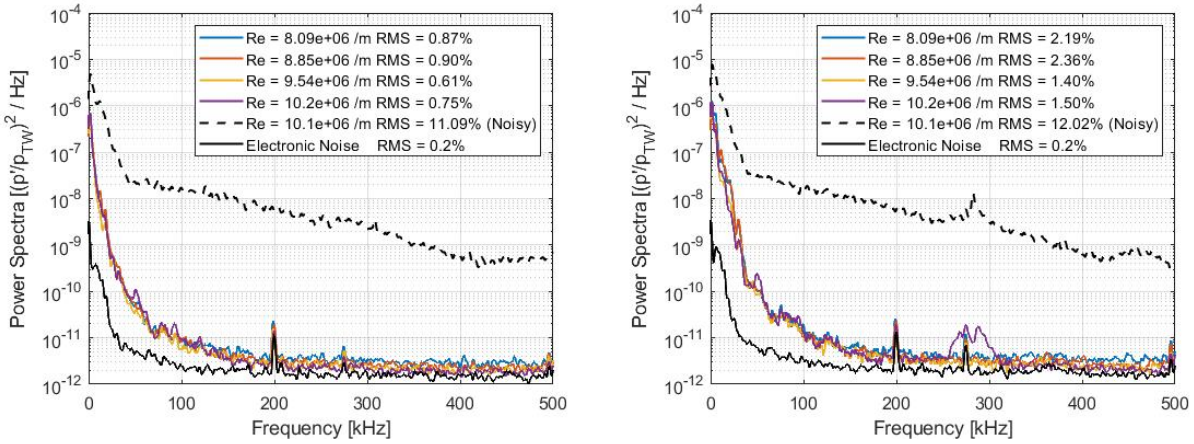

(a) PCB1 Power Spectra.

(b) PCB2 Power Spectra.

Figure 5.5. PCB1 and PCB2 power spectra with the unpolished, smooth-wall nosetip at different freestream Reynolds numbers.

Pressure fluctuations at the various Kulite locations were minimal and also did not exhibit any growth as the freestream Reynolds number increased. Power spectra of the Kulite pressure fluctuations at the maximum quiet freestream Reynolds number of 10×10^6 /m are shown in Figure 5.6. Kulites near the laminar streaks, such as K2 and K4, do not measure a significant significant amount of frequency content. In Figure 5.6d, some frequency content between 25 kHz and 125 kHz was measured. No peaks in the power spectra can be identified that might represent an instability in the boundary layer. There was also minimal growth observed in the power spectra as the freestream Reynolds number increased. Some disturbances may exist in the flow, but a clear instability were be identified in these measurements.

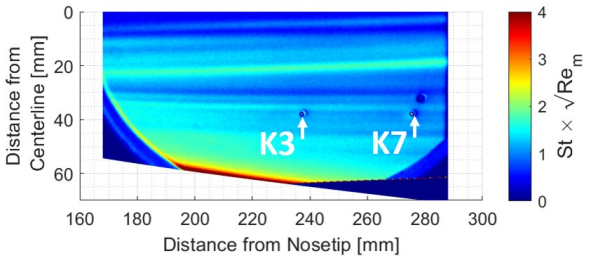

(a) Port side Kulites.

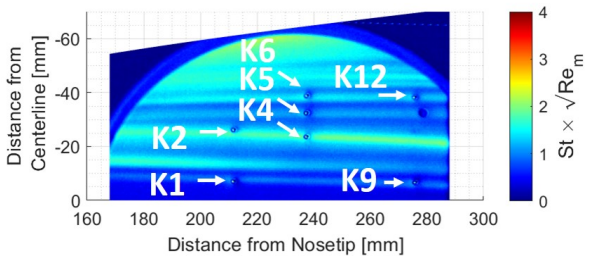

(b) Starboard side Kulites.

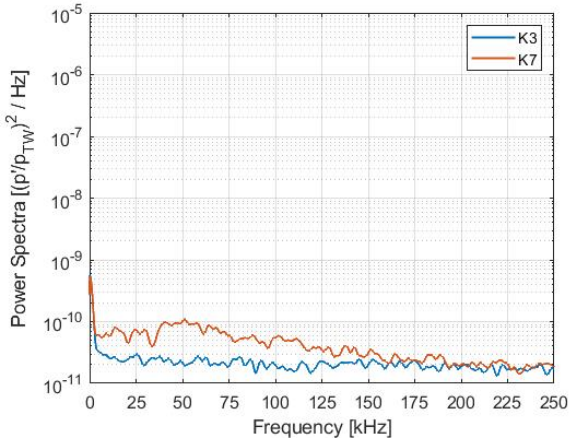

(c) Kulite PSD on the port side.

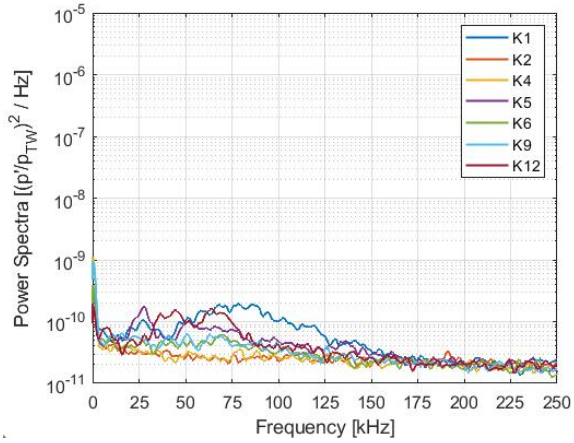

(d) Kulite PSD on the starboard side.

Figure 5.6. Kulite PSD plots with the unpolished, smooth-wall nosetip installed at $\alpha = 0°$ and Re $= 10 \times 10^6$ /m.

A repeat run was performed with the unpolished, smooth-wall nosetip during Entry 3. The run was performed at a freestream Reynolds number of 10.2 $\times$ 10^6 /m. Between the original and repeat run, the unpolished, smooth-wall nosetip was removed and several runs were performed with other nosetips. Spanwise cuts of heating were extracted at x/L = 0.98 from these runs and compared in Figure 5.7. The heating profiles are almost identical, indicating that the removal and reinstallation of the nosetip did not have a significant impact on the flow.

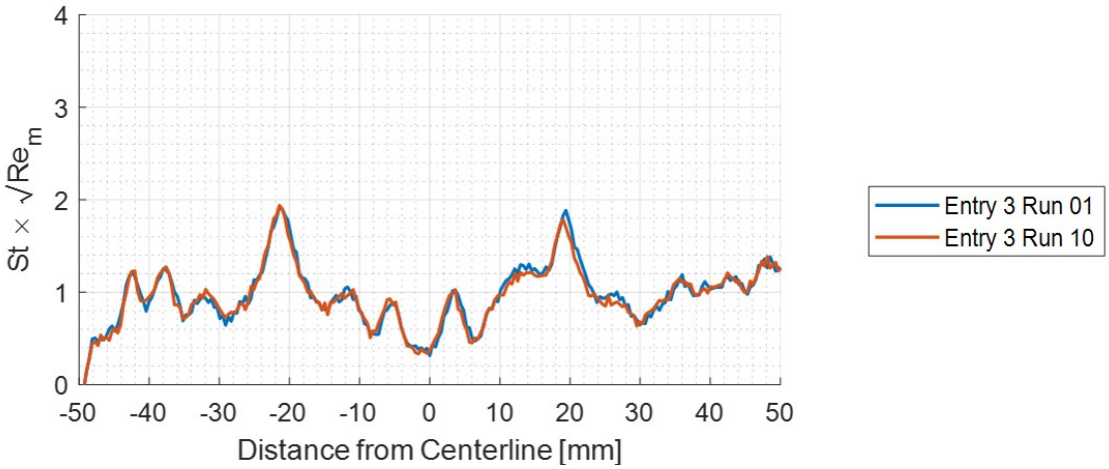

Figure 5.7. Repeatability of the spanwise cut of heating at x/L = 0.98 (x = 283 mm) with the unpolished, smooth-wall nosetip at Re = 10.2 $\times$ 10^6 /m.

The laminar streaks that are located 5 mm and 20 mm from the centerline are not symmetric and appear to be shifted towards the starboard (-Z) side of the experiment surface. An asymmetric streak located -12 mm from the centerline was also observed in both runs. The asymmetric features in the flow might be caused by asymmetries in the model, asymmetries in the nosetip, and residual yaw angles. A +0.20° residual yaw angle was measured with a digital protractor, which canted the port side of the experiment surface towards the flow. The model and sting were flipped 180° during Entry 4 to investigate the impact of the residual yaw angle. The IR camera and window were also moved to the other side of the tunnel. After the model was flipped, a -0.24° to -0.30° residual yaw angle was measured. The starboard side of the experiment surface was facing the direction of flow. The 0.06° difference in the residual yaw angle was achieved by adjusting the set screws that hold the

sting. Depending on the order that the set screws are tightened, the sting will be tilted slightly due to the small tolerances between the sting and the sting support. Note that this method to adjust the yaw angle was different than the fixed sting adapters that were used to achieve larger yaw angles, such as the 2° and 4° yaw angles that were tested in Section 5.3.

Runs were performed with the flipped model at a freestream Reynolds number of approximately 10.2×10^6 /m. One run was performed with a -0.24° yaw angle, and another with a -0.30° yaw angle. Spanwise cuts of heating were extracted from these runs at x/L = 0.98 and plotted in Figure 5.8 to identify the effect of the residual yaw angle. The small 0.06° difference in the yaw angle caused a small shift towards the starboard (+Z) side. A spanwise cut with the model in the original position is also plotted. The spanwise profile is shifted further towards the starboard (-Z) side of the experiment surface due to the larger difference in the residual yaw angle. The peak heating magnitudes are also slightly elevated and are thought to be caused by a residual angle of attack.

The spanwise cuts of heating are shifted by the tangential component of the residual yaw angle ($x \cdot \tan(2\beta)$) and plotted in Figure 5.9. Initially, an $x \cdot \tan(\beta)$ shift was applied to the spanwise cuts, but the profiles were still offset. A larger, $x \cdot \tan(2\beta)$ shift places the centerline of each spanwise profile near z = 0 mm. The peaks of the laminar streaks located 5 mm and 20 mm from the centerline are also symmetric across the centerline and in agreement between the different runs. The asymmetric streak located near -12 mm was on the port side of the experiment surface, even after the model was flipped. This indicates that the asymmetric streak is likely caused by an asymmetry in the model geometry.

The exact reason to which a tangential shift that is two times the magnitude of the measured yaw angle was needed to align the laminar streaks is unknown. However, there are many factors that may contribute to this. First, the laminar streaks appear to be curved towards the centerline. A linear shift in the spanwise component may not be sufficient to account for this. Second, the digital protractor that was used to measure the residual yaw angle is accurate within ±0.06°. The uncertainty is almost 20% of the measured value. The results shown in Figures 5.10 and 5.50 were shifted by $x \cdot \tan(\beta)$ and align the centerline of the data near z = 0 mm.

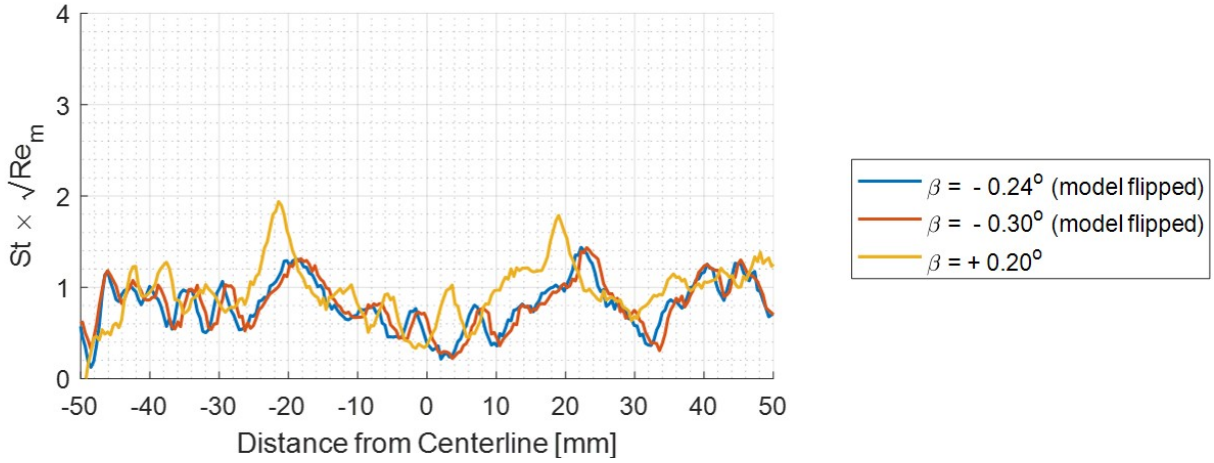

Figure 5.8. Effect of residual yaw angles on the spanwise cuts of heating at x/L = 0.98 (x = 283 mm). Re = 10.2×10^6 /m.

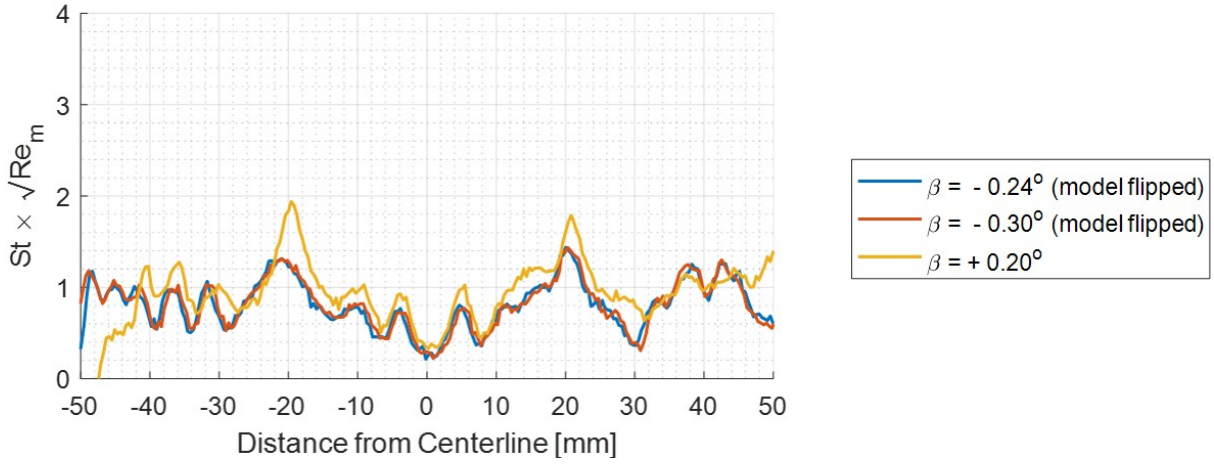

Figure 5.9. Spanwise cuts of heating at x/L = 0.98 (x = 283 mm) from Figure 5.8, shifted by $x \cdot \tan(2\beta)$. Re = 10.2×10^6 /m.

The location and peak heating magnitudes of the laminar streaks are compared to computations performed by Li, Choudhari, and Paredes from Reference [13]. The flow conditions of the experiment and the computations are similar and are provided in Table 5.1. The heating magnitudes are compared at a spanwise cut along x/L = 0.91, shown in Figure 5.10. The data from the experiment is shifted by $x \cdot \tan(\beta)$ to adjust for the 0.20° residual yaw angle. This magnitude of shift was selected such that the centerline and peaks near ± 5 mm are in agreement with the computational result. With the shift, both the location and peak heating magnitudes of the laminar streaks are in good agreement. This indicates that the computations can accurately predict the laminar streak pattern on the BOLT geometry and that the experiments are of good quality. Small differences in the peak locations and heating magnitudes might be caused by asymmetries in the model and a residual angle of attack.

Table 5.1. Experimental and computational freestream conditions for the 33% scale BOLT model

Case	$\mathbf{M}_\infty$	**Re** m^{-1}	$\mathbf{P}_\infty$ Pa	$\mathbf{T}_\infty$ K	$\mathbf{T}_w$ K
BAM6QT	6.0	9.88×10^6	527.7	52.7	303 ± 2
DNS	6.0	9.88×10^6	564.3	51.6	300

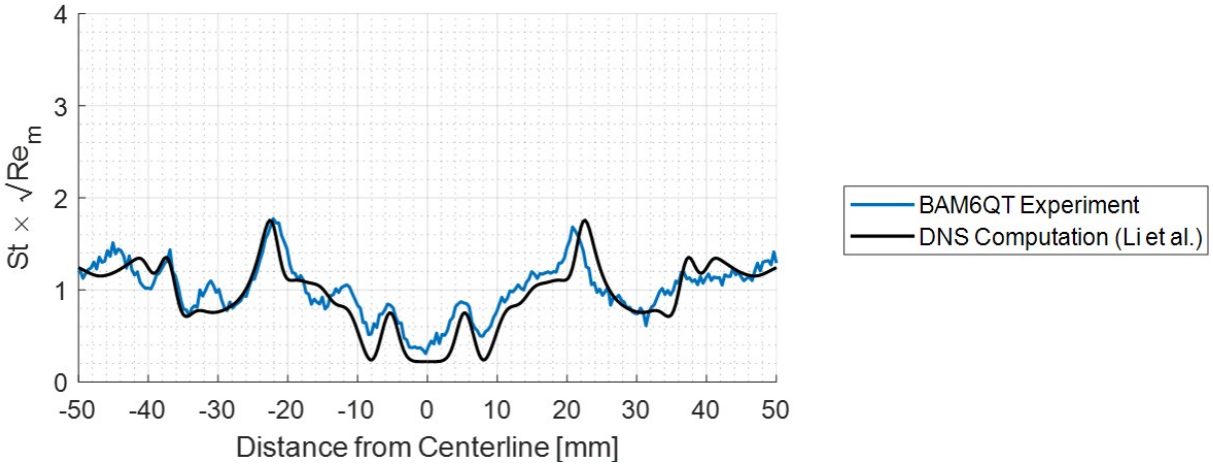

Figure 5.10. A comparison of experiment and computational heat transfer from Li, Choudhari, and Paredes [13] at x/L = 0.91. The experimental data is shifted by $x \cdot tan(\beta)$ to account for the residual yaw angle. Re = 9.88×10^6 /m. (Run 10, P_0 = 129.0 psia, T_0 = 414.4 K)

5.1.2 Measurements with the Backward-Facing Steps

Runs were performed with the two backward-facing steps immediately after the baseline measurements in Entry 3. The model was not adjusted, so the residual 0.20° yaw angle that was previously measured was also present in these measurements. The port side of the experiment surface was facing the windward direction. Four runs with each of the backward-facing steps were performed to enable a comparison across different freestream Reynolds numbers. The scaled heating contours shown in Figure 5.11 are at a freestream Reynolds number of approximately 10.2×10^6 /m. The two runs were performed at similar tunnel conditions, however small variations in the initial stagnation pressure and temperature result in freestream Reynolds numbers that differ by $\pm$ 0.1×10^6 /m. In both heating plots, a region of increased heating was measured on the port side of the experiment surface near 35 mm from the centerline. With the 0.508 mm step, a thin wedge of heating forms at the very aft end of the model. A thin wedge of heating also forms with the larger 1.016 mm step at a similar location, but it appears to form at a further upstream location. A second, smaller wedge of heating forms just outboard of the first one. The heating magnitudes along the two thin wedges of heating appear to be more intense with the larger 1.016 mm step.

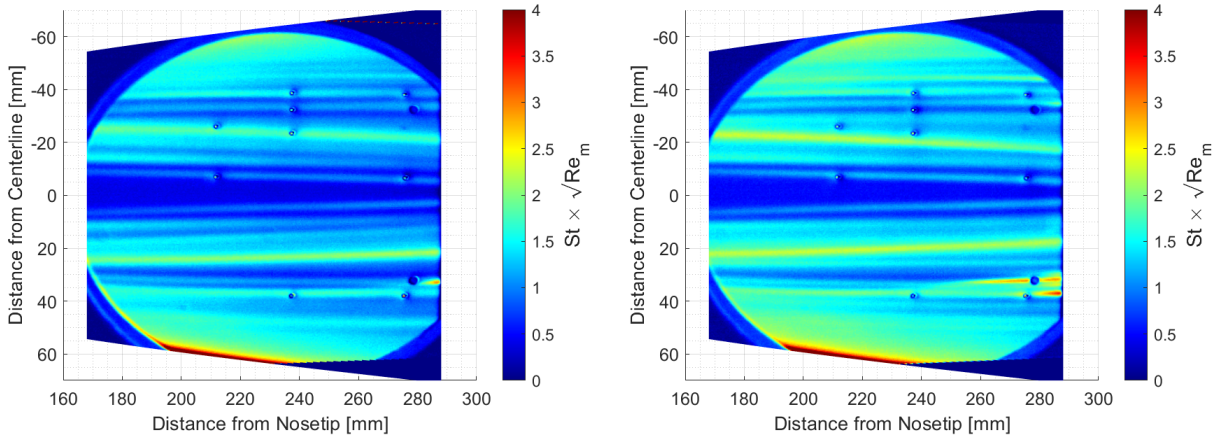

(a) k = + 0.508 mm. (Run 18)

(b) k = + 1.016 mm. (Run 02)

Figure 5.11. Scaled heating contours with the backward-facing steps installed. Re = 10.2×10^6 /m and $\alpha = 0°$.

Spanwise cuts of heating at x/L = 0.98 were extracted from each of the heating contours and plotted in Figure 5.12. The unpolished, smooth-wall measurements in quiet and noisy flow are also plotted in black. The thin wedges of heating form between 30 and 40 mm from the centerline. With the 0.508 mm step, the peak in the spanwise profile is located 34 mm from the centerline and has a peak heating magnitude near $St \times \sqrt{Re} = 2.0$. With the larger 1.016 mm step, there are two peaks in the spanwise heating profile located 32 mm and 37 mm from the centerline. The peak heating magnitudes of both peaks are around $St \times \sqrt{Re} = 2.7$. With the backward-facing steps, heating magnitudes in this region are a factor of 2 to 3 greater than the unpolished, smooth-wall measurement in quiet flow. It is thought that the backward-facing steps are the cause of these wedges of heating.

The laminar streak that is located + 20 mm from the centerline appears to shift due to the backward-facing steps. However, the direction of the shift is different between the two step sizes. An outboard shift was observed with the 0.508 mm step, whereas an inboard shift was observed with the 1.016 mm step. The heating magnitude of the laminar streak was also slightly elevated when compared to the unpolished, smooth-wall measurement. The laminar streak located + 5 mm from the centerline does not appear to be affected by the backward-facing step.

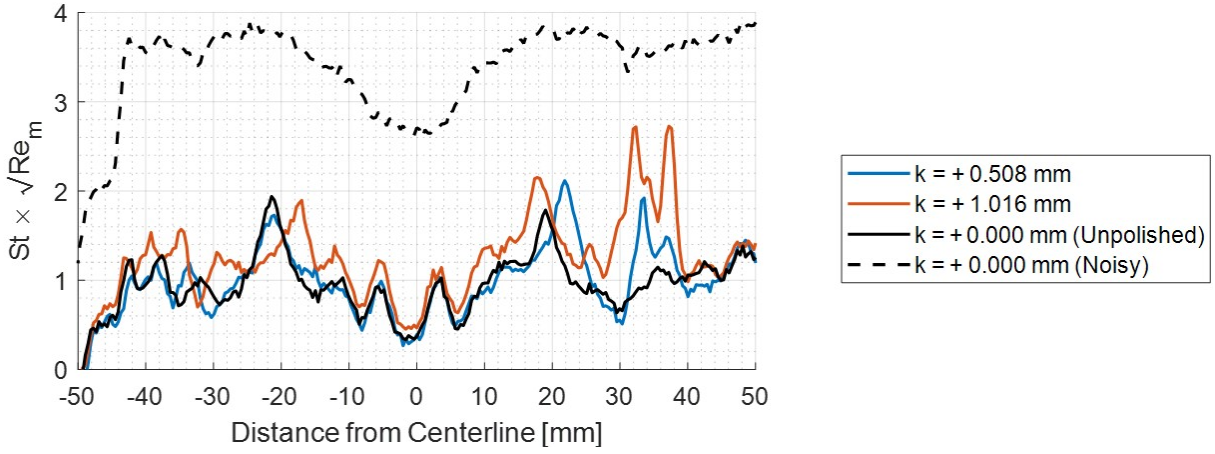

Figure 5.12. Spanwise cuts of heating at x/L = 0.98 (x = 283 mm) with the backward-facing steps installed. Re = 10.2×10^6 /m and $\alpha = 0°$.

Some increased heating and shifts in the laminar streak were observed on the starboard side of the experiment surface, but the effects of the backward-facing steps appear to be concentrated on the port side of the experiment surface. There were many uncertainties in the experiment that could contribute to the asymmetry. First, the port side of the experiment surface was facing towards the windward direction due to the residual yaw angle. The step height on the port side may have a stronger effect because of this. Second, small differences between the port and starboard step heights could potentially produce an asymmetric effect. Asymmetries in the body geometry were also measured and could also contribute to this. It is likely that a combination of these factors results in the observed asymmetries.

The backward-facing steps were tested at different freestream Reynolds numbers to identify the development of the wedges of heating. Growth of the thin wedges of heating was observed as the freestream Reynolds number increased. Zoomed-in scaled heating contours are shown in Figure 5.13 to illustrate this. On the left-hand side, Figures 5.13c, 5.13a, 5.13e, and 5.13g, the thin wedge of heating with the 0.508 mm step is only seen at the highest freestream Reynolds number of 10.2 $\times$ 10^6 /m. With the larger 1.016 mm step, shown in Figures 5.13b, 5.13d, 5.13f, and 5.13h, heating magnitudes start to increase at a freestream Reynolds number of 9.57 $\times$ 10^6 /m. As the freestream Reynolds number increases to 10.2 $\times$ 10^6 /m, the two wedges of heating become visually apparent.

Spanwise cuts of heating at x/L = 0.98 were extracted from each of these runs to quantitatively compare the growth of the wedges of heating. Runs with the 0.508 mm step are plotted in Figure 5.14. Between the freestream Reynolds numbers of 8.13 $\times$ 10^6 /m and 9.58 $\times$ 10^6 /m, the heating magnitudes were relatively consistent and were similar to the unpolished, smooth-wall measurement. A sharp rise in heating located 34 mm from the centerline was measured at a freestream Reynolds number of 10.2 $\times$ 10^6 /m. The outboard shift of the laminar streak located 20 mm from the centerline appears to be consistent across the different freestream Reynolds numbers. With the 1.016 mm step, shown in Figure 5.15, a sharp rise in heating was first measured at a freestream Reynolds number of 9.57 $\times$ 10^6 /m. A peak in the spanwise profile forms near 34 mm from the centerline. As the freestream Reynolds number increases to 10.1 $\times$ 10^6 /m, the heating magnitude increases and a second peak forms near 38 mm from the centerline.

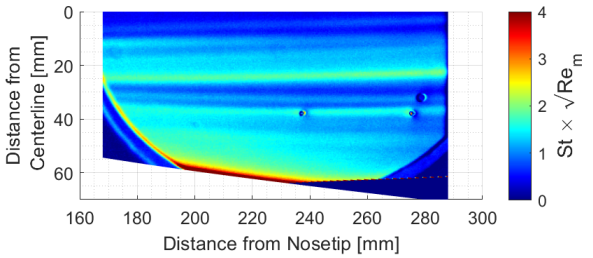

(a) Re = 8.13 × 10^6 /m and k = + 0.508 mm. (Run 21)

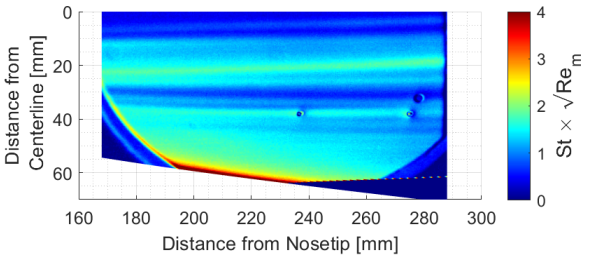

(b) Re = 8.14 × 10^6 /m and k = + 1.016 mm. (Run 05)

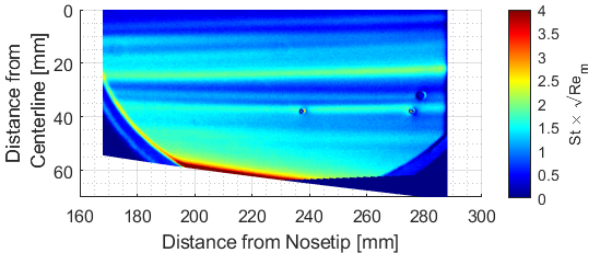

(c) Re = 8.91 × 10^6 /m and k = + 0.508 mm. (Run 20)

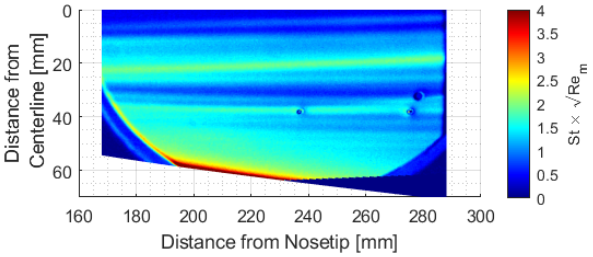

(d) Re = 8.90 × 10^6 /m and k = + 1.016 mm. (Run 04)

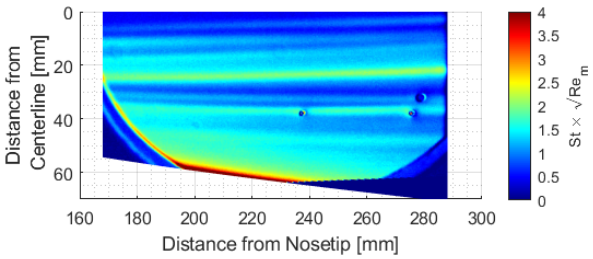

(e) Re = 9.58 × 10^6 /m and k = + 0.508 mm. (Run 19)

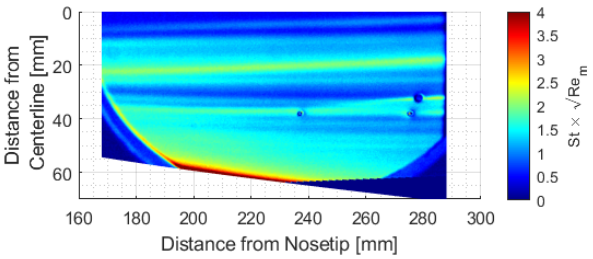

(f) Re = 9.57 × 10^6 /m and k = + 1.016 mm. (Run 03)

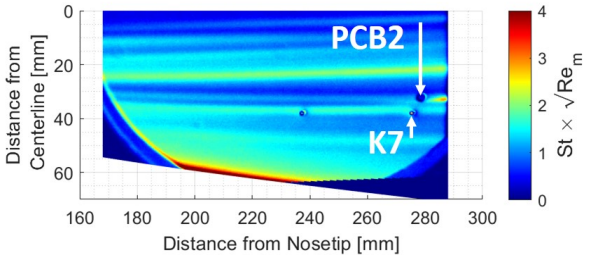

(g) Re = 10.2 × 10^6 /m and k = + 0.508 mm. (Run 18)

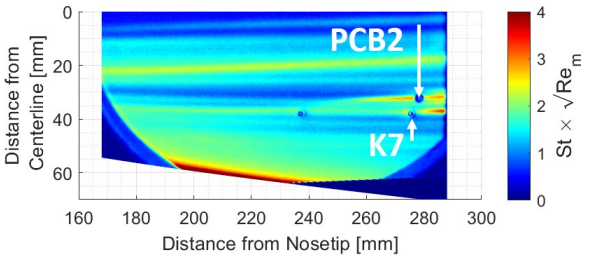

(h) Re = 10.1 × 10^6 /m and k = + 1.016 mm. (Run 02)

Figure 5.13. Zoomed-in scaled heating contours with the backward-facing steps installed at different freestream Reynolds numbers and $\alpha = 0°$.

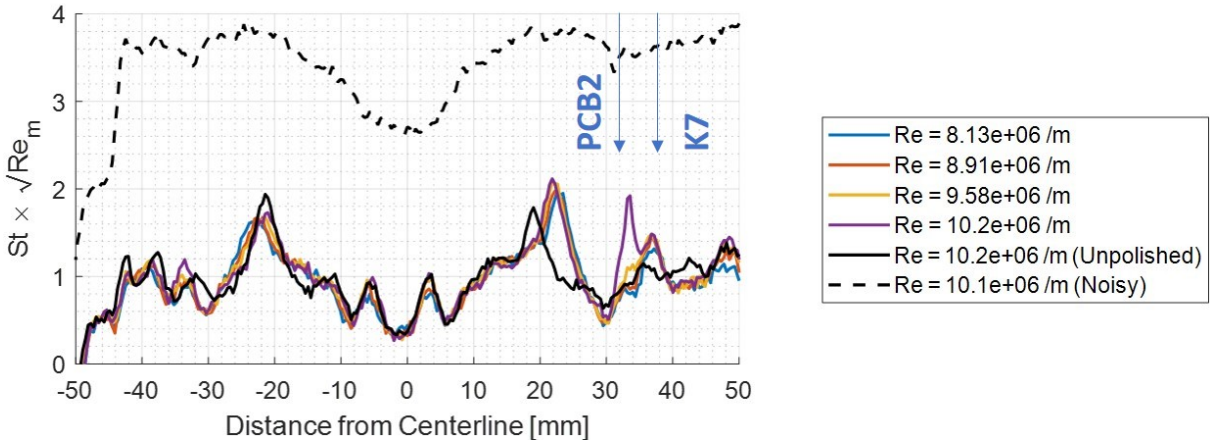

Figure 5.14. Spanwise cuts of heating at x/L = 0.98 (x = 283 mm) with the 0.508 mm backward-facing step at different freestream Reynolds numbers and $\alpha = 0°$.

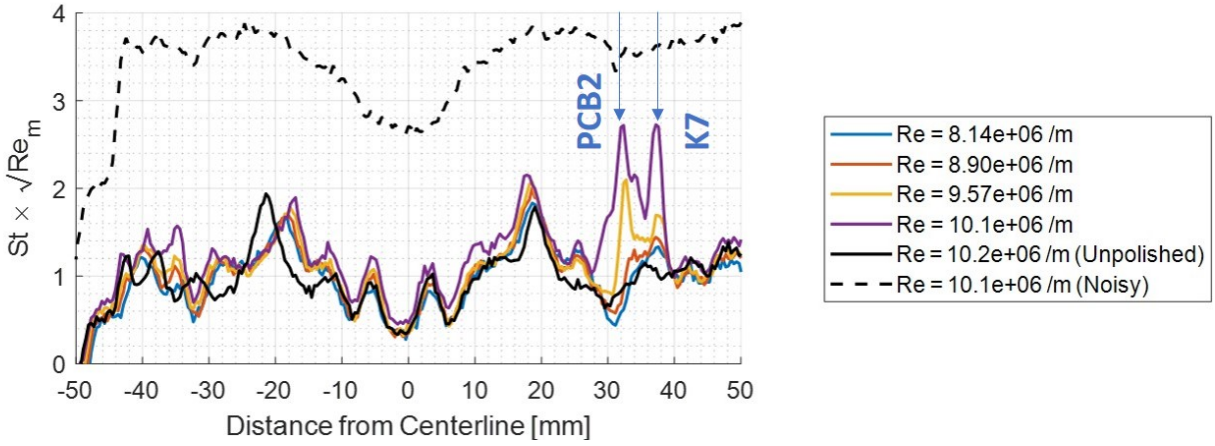

Figure 5.15. Spanwise cuts of heating at x/L = 0.98 (x = 283 mm) with the 1.016 mm backward-facing step at different freestream Reynolds numbers and $\alpha = 0°$.

Increased pressure fluctuations were measured near the thin wedges of heating. The PCB2 sensor, located at the aft end of the model and 38 mm from the centerline, was directly underneath the heating pattern. The power spectra of the measured pressure fluctuations at PCB2 are shown in Figure 5.16. With the 0.508 mm step, a 250 kHz peak frequency is seen in the power spectra. The amplitude of the 250 kHz peak grows as the freestream Reynolds number increases, which is indicative of an instability in the boundary layer. A rise in broadband frequency content at the maximum quiet freestream Reynolds number of 10.2×10^6 /m indicates that the instability is starting to break down. The RMS pressure fluctuation magnitudes are above the smooth-wall measurement but are still below noisy flow levels.

With the larger 1.016 mm step, there is frequency content centered around 150 kHz and 240 kHz peaks in the power spectra. The amplitude of the frequency content also increases with an increasing freestream Reynolds number. A significant increase in broadband fre-

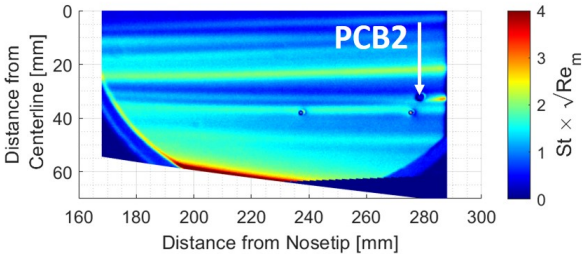

(a) k = + 0.508 mm.

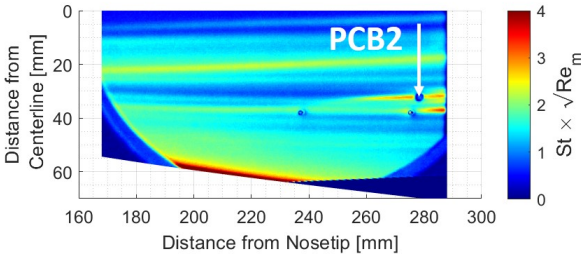

(b) k = + 1.016 mm.

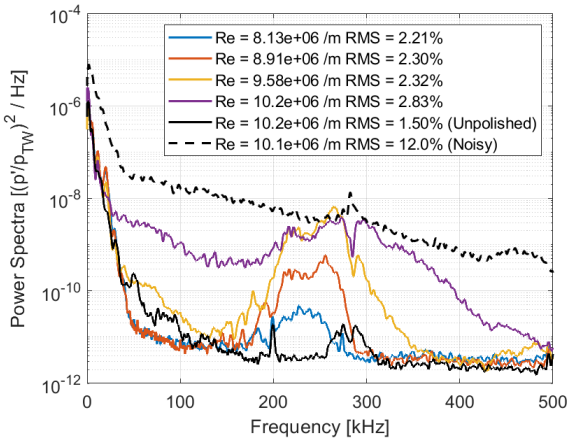

(c) k = + 0.508 mm.

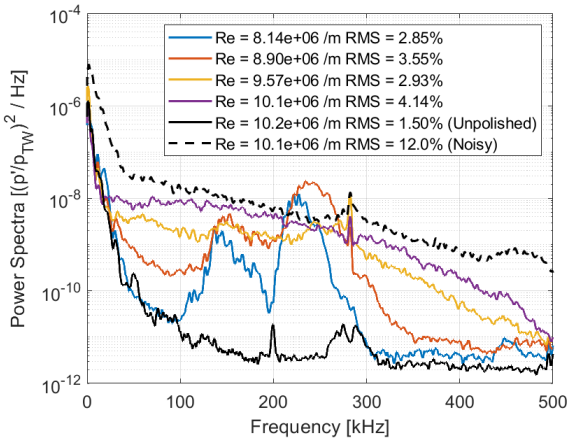

(d) k = + 1.016 mm.

Figure 5.16. PCB2 PSD plots with the backward-facing steps installed at $\alpha = 0°$.

quency content at Re = 9.57 $\times$ 10^6 /m indicates that the instability has broken down into turbulence. This coincides with the onset of increased heating that was observed in the heat transfer at the same freestream Reynolds number. Additional broadband frequency content was measured at the highest Reynolds number of 10.1 $\times$ 10^6 /m as the flow becomes more turbulent.

Because the sensor is near the thin wedge of heating, it is thought that the instability arises from a secondary instability. If the thin wedge of heating is representative of a vortical structure, an instability could arise in the shear layer at the edge of the vortical structure. The peak frequencies are similar to the secondary instability that was identified on a 7° half-angle cone by Edelman [26]. Computations or off-body measurements would be needed to verify this. The instability could also be caused by a modulated second-mode instability. The peak frequencies that were measured with the backward-facing steps are somewhat similar to computations of a second-mode instability by Thome et al. [14]. However, it should be noted that the stability computations were performed without the step in the geometry. It is possible that the step interacts with or amplifies a second-mode instability, but computations that include the step would be needed to verify this.

Although no wedges of heating were observed on the starboard side of the model, some increases in the pressure fluctuations were measured at PCB1. The power spectra of pressure fluctuations at PCB1 with each backward-facing step are shown in Figure 5.17. With the smaller 0.508 mm step, the measured pressure fluctuations were similar to the unpolished, smooth-wall measurement. The power spectra show a minimal amount of frequency content, and the RMS pressure fluctuations are near 0.70% at all the freestream Reynolds numbers that were tested. With the 1.016 mm step, a 180 kHz peak frequency was measured and can be seen in the power spectra. The amplitude of the 180 kHz peak grows with the increasing freestream Reynolds number and is representative of an instability. Low-frequency content was also increasing at Re = 9.57 $\times$ 10^6 /m and indicates that the instability was starting to break down. At the highest freestream Reynolds number of 10.1 $\times$ 10^6 /m, the power spectra is not fully broadband and suggests that the flow has not yet transitioned into turbulence.

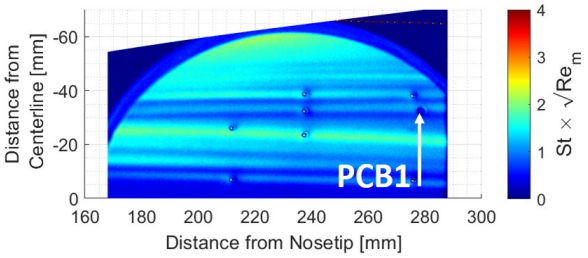

(a) k = + 0.508 mm.

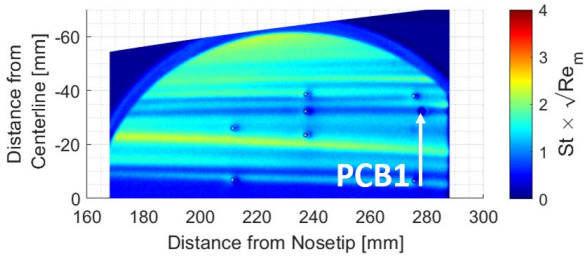

(b) k = + 1.016 mm.

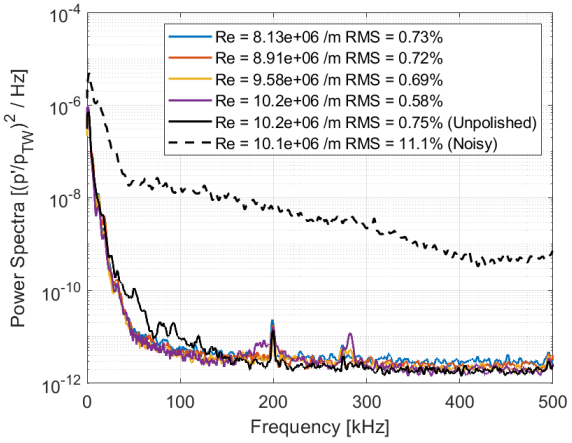

(c) k = + 0.508 mm.

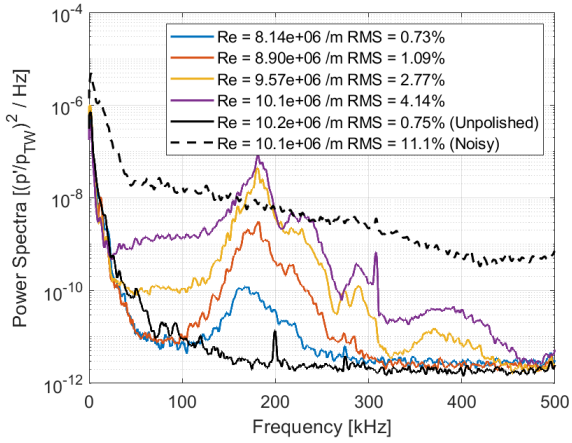

(d) k = + 1.016 mm.

Figure 5.17. PCB1 PSD plots with the backward-facing steps installed at $\alpha = 0°$.

The K7 sensor, located at the aft end and the port side of the model, was also near the wedges of heating. PSDs in Figure 5.18 show the measured frequency content with both backward-facing steps, along with the baseline measurements with the unpolished, smooth-wall nosetip. With the 0.508 mm step, a small amount of frequency content can be seen between 0 kHz and 150 kHz. The broadband amplitudes are small and do not increase as the freestream Reynolds numbers increase. Small fluctuations in the flow are likely present, however there is no clear indication of a growing instability. With the larger 1.016 mm step, frequency content that is centered around a 50 kHz peak and above 175 kHz can be seen in the power spectra. The amplitude of the 50 kHz peak increases as the freestream Reynolds number increases and might be an indication of an instability. The peak frequency is somewhat similar to an unstable mode that was computed by Thome et al. [14]. The increase in frequency content above 175 kHz is likely caused by a Kulite sensor resonance.

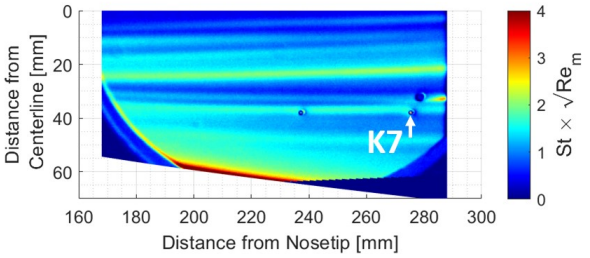

(a) k = + 0.508 mm.

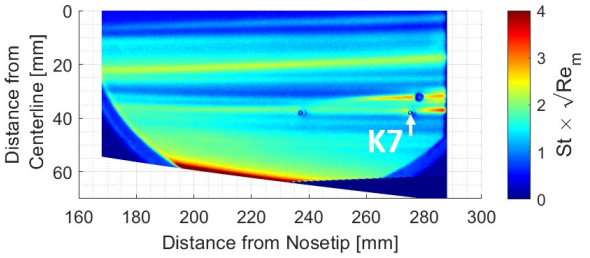

(b) k = + 1.016 mm.

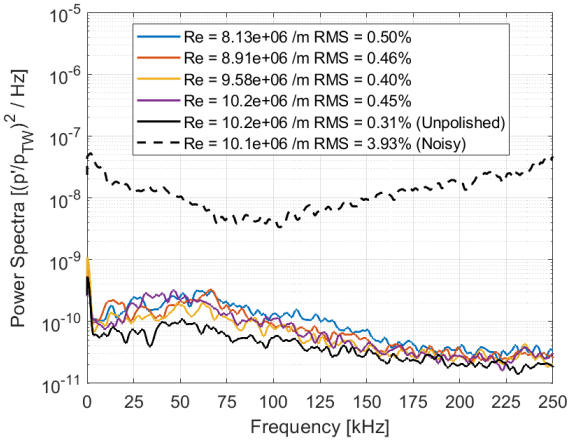

(c) k = + 0.508 mm.

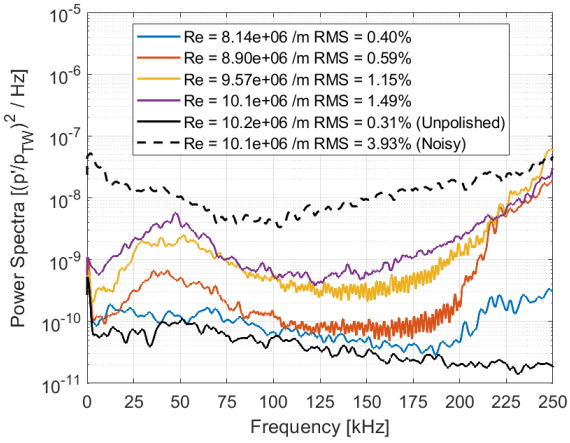

(d) k = + 1.016 mm.

Figure 5.18. K7 PSD plots with the backward-facing steps installed at $\alpha = 0°$.

The power spectra of the Kulite sensors on the port side of the experiment surface with each backward-facing step installed are shown in Figure 5.19 at Re = 10 × 10^6 /m. With the 1.016 mm backward-facing step, only K12 measured a substantial amount of frequency content. At the K12 sensor face, heat transfer magnitudes were similar to the unpolished, smooth-wall measurement. No wedges of heating appear to develop near the K12 sensor face. Some frequency content above 175 kHz was also measured at K5. It is thought to be caused by the Kulite sensor resonance at 300 kHz. Peaks near 50 kHz and 180 kHz in Figure 5.19d might be representative of an instability at the K12 sensor face. K2 and K4 are closest to the most intense laminar streak near - 20 mm from the centerline, but do not measure any elevated pressure fluctuations. The measured frequency content does not appear to have a strong relationship with the strength of laminar streaks.

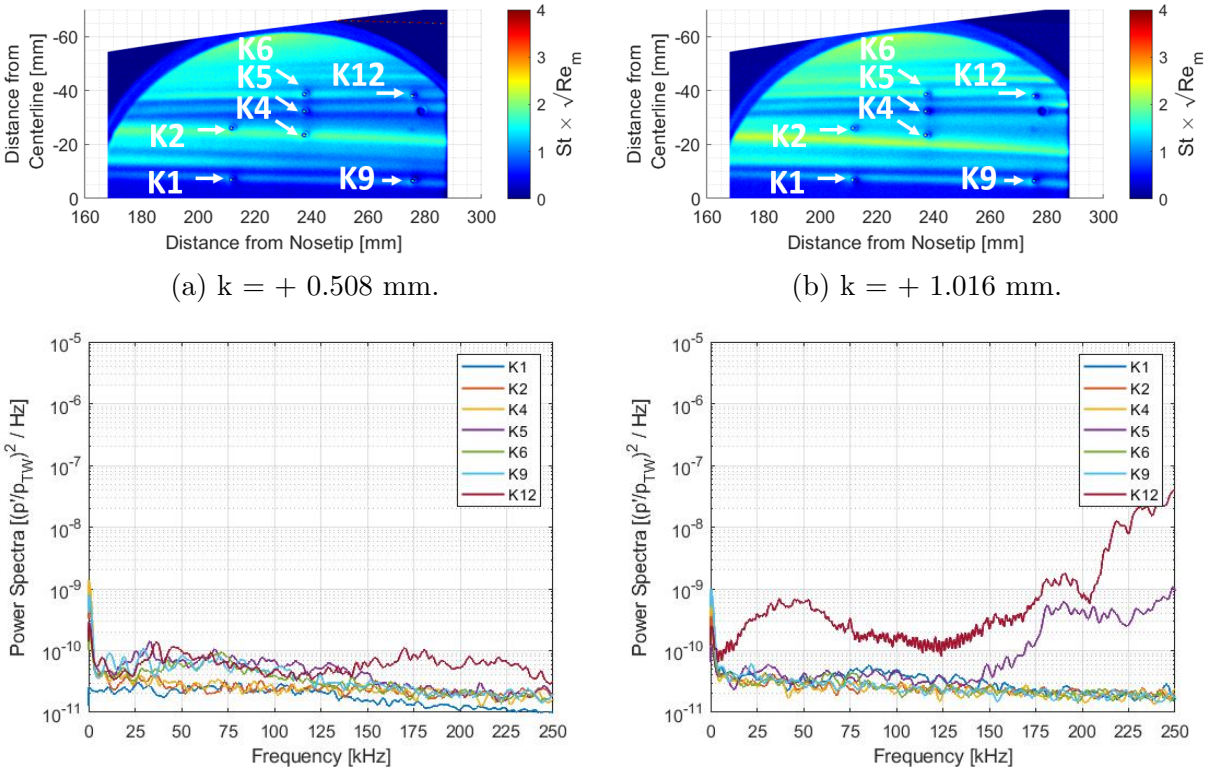

(a) k = + 0.508 mm.

(b) k = + 1.016 mm.

(c) k = + 0.508 mm.

(d) k = + 1.016 mm.

Figure 5.19. Kulite PSD plots with the backward-facing steps installed at $\alpha = 0°$ and Re = 10 × 10^6 /m.

5.1.3 Measurements with the Forward-Facing Steps

Scaled heating contours with the three forward-facing steps are shown in Figure 5.20 at a freestream Reynolds number near 10.1×10^6 /m. The scaled heating contour with the unpolished, smooth-wall nosetip is also shown. The laminar streaks and heating magnitudes with the forward-facing steps are visually similar to the unpolished, smooth-wall measurement. There were no sharp increases in heat transfer that would indicate transition. With the 0.305 mm step, heating magnitudes along the laminar streaks appear to be slightly more intense than the smaller steps.

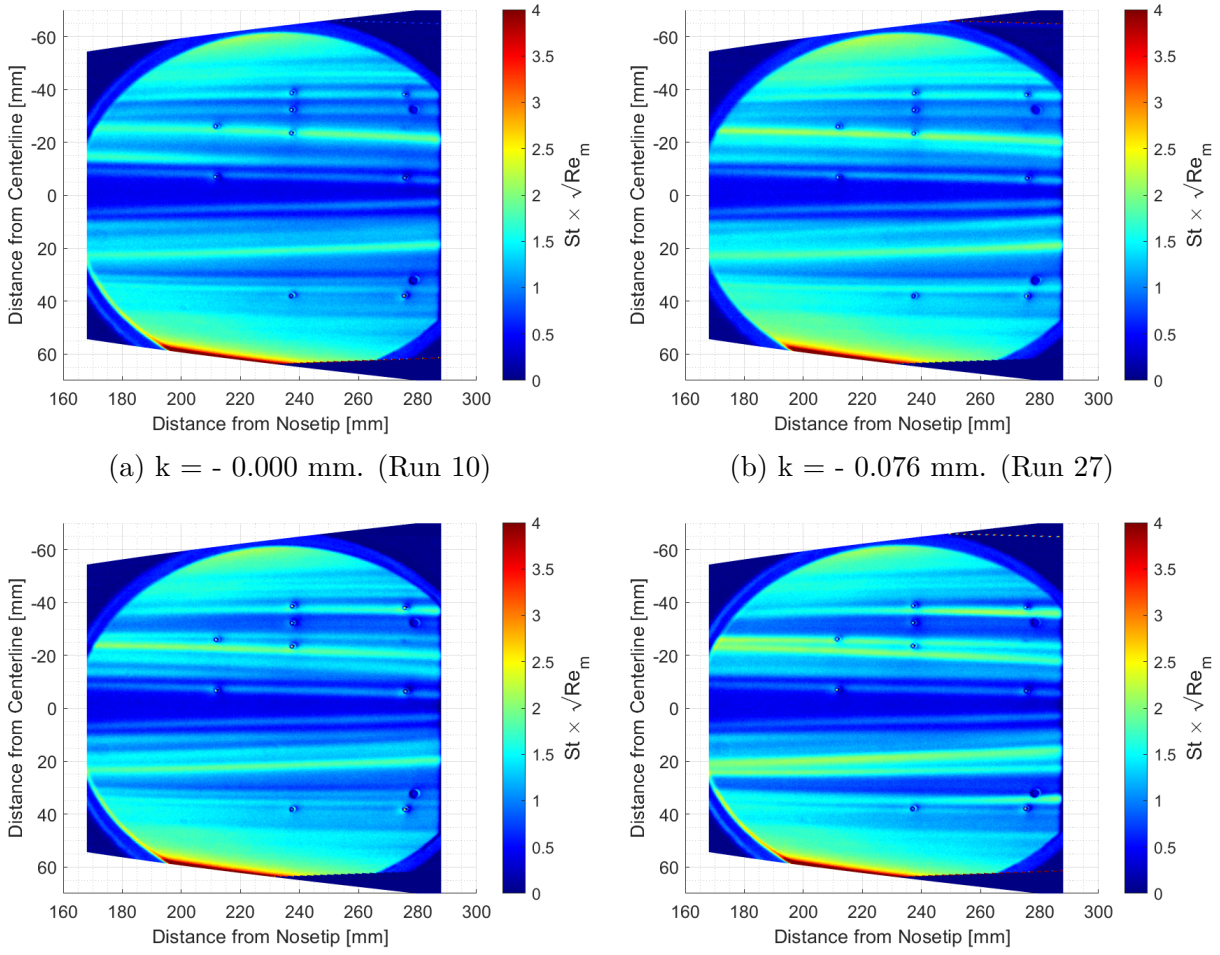

(a) k = - 0.000 mm. (Run 10)

(b) k = - 0.076 mm. (Run 27)

(c) k = - 0.152 mm. (Run 23)

(d) k = - 0.305 mm (Run 06)

Figure 5.20. Scaled heating contours with the forward-facing steps installed at Re = 10.1×10^6 /m and $\alpha = 0°$.

Spanwise cuts of heating were extracted from each heating contour and plotted in Figure 5.21. There is a region of increased heating located -35 mm from the centerline. At this location, the heating magnitude increases as the step size increases. Some differences can also be seen between -20 mm and -10 mm from the centerline. The laminar streak appears to widen with the forward-facing steps. With the largest 0.305 mm step, two lobes of heating that are located -23 mm and -17 mm from the centerline can be seen and represent a "double streak" pattern. The region of increased heating and the double streak pattern is also seen on the starboard side of the model. The effects of the forward-facing steps appear to be more symmetric than the effects seen with the backward-facing steps.

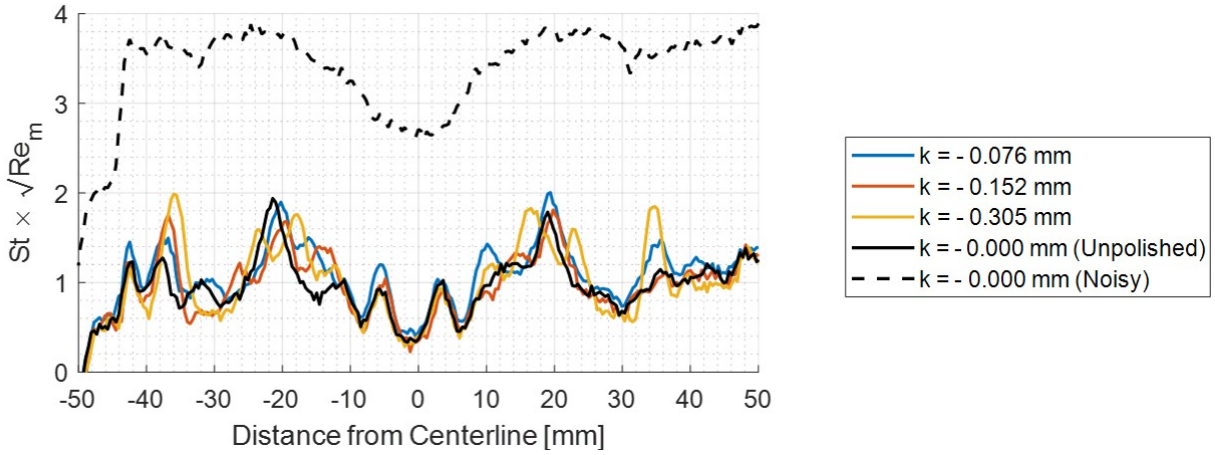

Figure 5.21. Spanwise cuts of heating at x/L = 0.98 (x = 283 mm) with the forward-facing steps installed at Re = 10.1 × 10^6 /m and $\alpha = 0°$.

Spanwise cuts of heating with the 0.305 mm step at different freestream Reynolds numbers are shown in Figure 5.22. Approximately -35 mm from the centerline, an increase in the heating magnitude was measured as the freestream Reynolds number increased. The location of increased heating is similar to the location of the thin wedges observed with the backward-facing steps. The double streak pattern was measured near -20 mm from the centerline and had consistent heating magnitudes across the different freestream Reynolds numbers. The single, laminar streak that was measured with the unpolished, smooth-wall nosetip appears to be split into the double streak pattern. A similar effect can also be seen on the starboard side of the model.

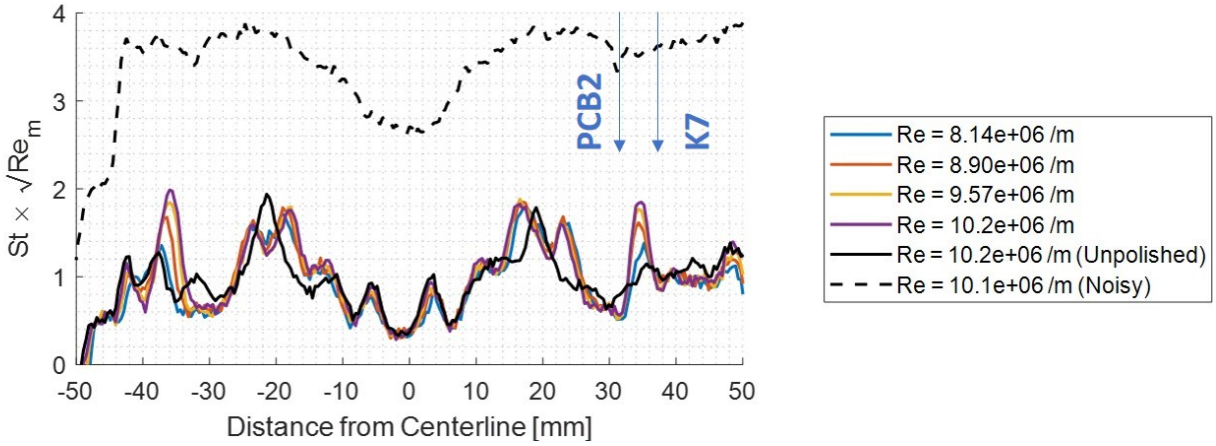

Figure 5.22. Spanwise cuts of heating at x/L = 0.98 (x = 283 mm) with the 0.305 mm forward-facing step at different freestream Reynolds numbers and $\alpha = 0°$. (Runs 06 through 09)

The power spectra of pressure fluctuations at PCB1 and PCB2 with the 0.305 mm step installed are shown in Figure 5.23. Some increases in heating were observed near these sensor locations, but the intensity of heating was much lower than what was measured with the backward-facing steps. Minimal pressure fluctuations were measured at PCB1. The frequency content in the power spectra are near the unpolished, smooth-wall measurement and collapse onto a similar profile. At PCB2, some frequency content that is centered around a 180 kHz peak was measured. The amplitude of the peak frequency increases slightly as the freestream Reynolds number increases. However, the amplitude at the highest freestream Reynolds number of 10.2×10^6 /m is less than an order of magnitude above the unpolished, smooth-wall measurement. It appears that there was an instability growing in the boundary layer, however the amplitude of the instability was much smaller when compared to the measurements with the backward-facing steps.

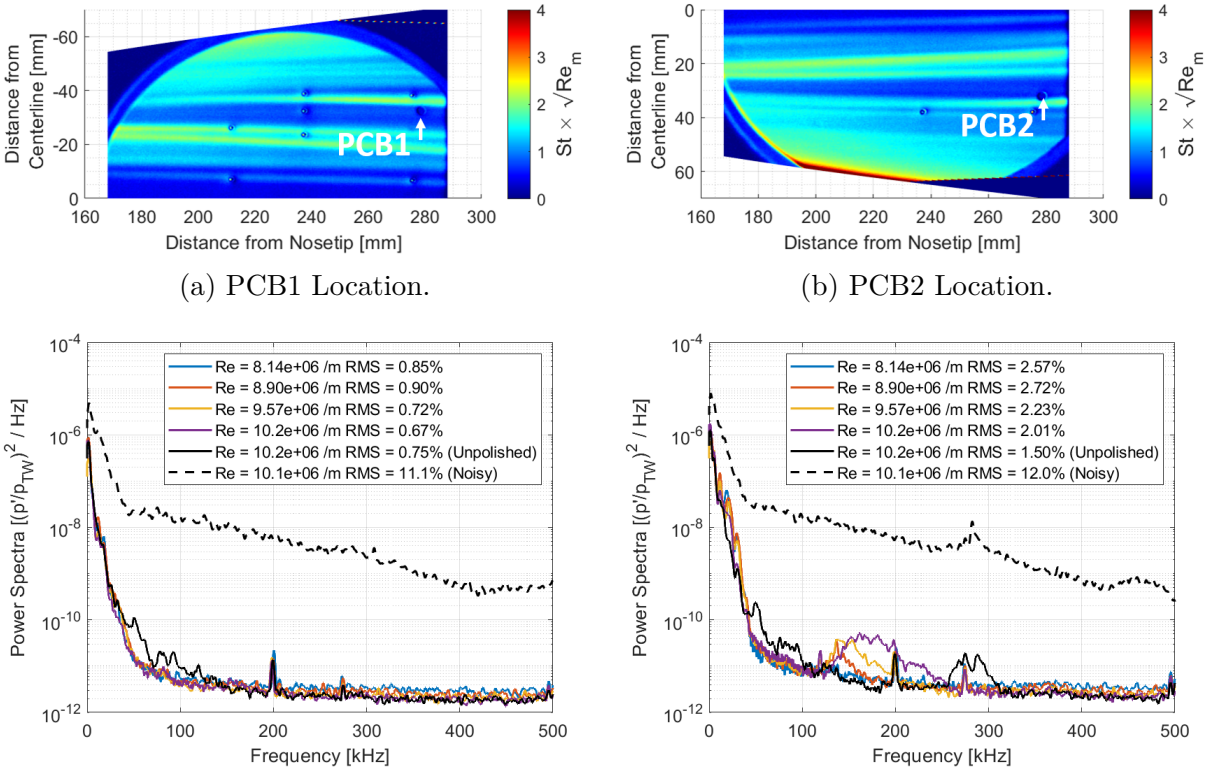

(a) PCB1 Location.

(b) PCB2 Location.

(c) PCB1.

(d) PCB2.

Figure 5.23. PCB1 and PCB2 PSD plots with the 0.305 mm forward-facing step installed at different freestream Reynolds numbers and $\alpha = 0°$.

A clear growth of an instability was not identified in the Kulite pressure fluctuation measurements with the forward-facing steps. The power spectra of the pressure fluctuations at the various Kulite sensor locations with the largest 0.305 mm forward-facing step installed are shown in Figure 5.28 at a freestream Reynolds number near 10×10^6 /m. On the port side of the experiment surface, K3 and K7 measured minimal frequency content. Pressure fluctuation magnitudes were low and did not grow with increasing freestream Reynolds numbers. On the starboard side of the experiment surface, minimal pressure fluctuations were also measured. Some frequency content between 50 kHz and 125 kHz was measured at K1, might represent some disturbances. However, the frequency content did not grow significantly with an increasing freestream Reynolds number.

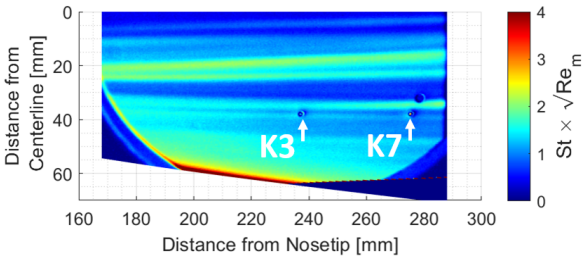

(a) Port side Kulites.

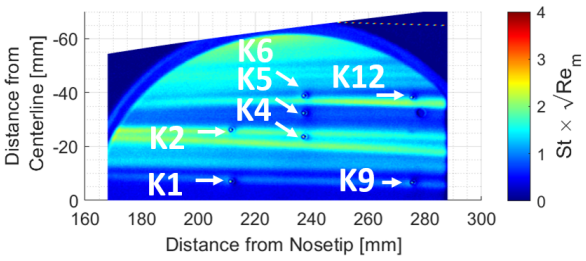

(b) Starboard side Kulites.

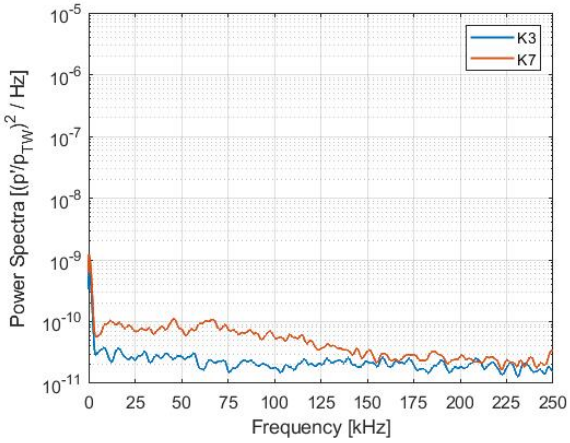

(c) Kulite PSD on the port side.

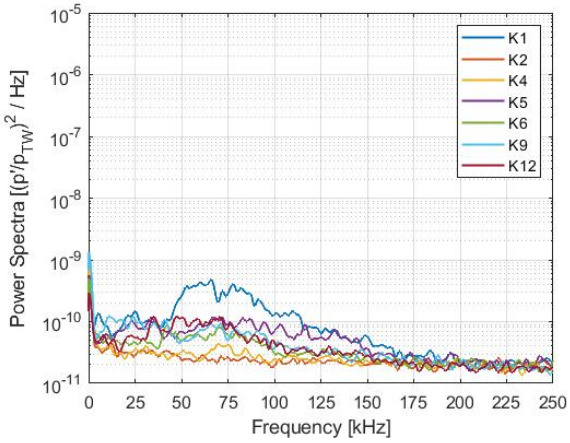

(d) Kulite PSD on the starboard side.

Figure 5.24. Kulite PSD plots with the 0.305 mm forward-facing step installed at $\alpha = 0°$ and Re $= 10 \times 10^6$ /m.

5.1.4 Measurements with the Polished Nosetip

Experiments were performed with the polished, smooth-wall nosetip to investigate the effect of distributed surface roughness. A side-by-side comparison of the scaled heating contours with an unpolished nosetip and polished nosetip is shown in Figure 5.25. Both of these runs were performed at a freestream Reynolds number of approximately 10.2×10^6 /m and during Entry 3. The laminar streak pattern was still observed with the polished nosetip. This suggests that the development of the laminar streaks is not significantly impacted by the surface roughness of the nosetip. Spanwise cuts of heating at x/L = 0.98 from each heating contour are plotted in Figure 5.26. The peak heating magnitudes of the laminar streaks located ± 5 mm from the centerline are nearly identical. The laminar streak that is located + 20 mm from the centerline appears to be slightly shifted between the two runs. A similar shift in the location of the laminar streak was not seen on the starboard side of

the experiment surface. The small shift might be caused by an asymmetry of the nosetip geometry.

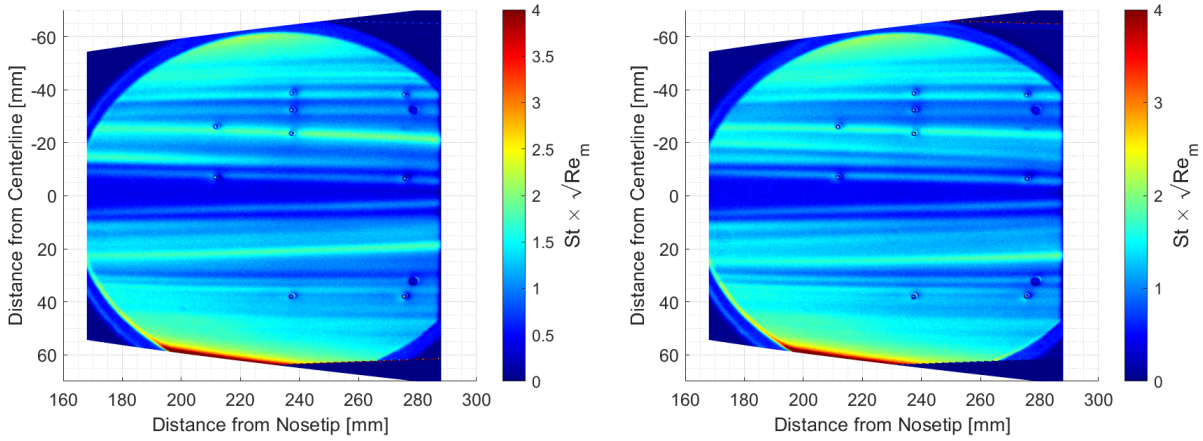

(a) Unpolished Nosetip. (Run 10)

(b) Polished Nosetip. (Run 14)

Figure 5.25. Scaled heating contours with the unpolished and polished smooth-wall nosetips at Re = 10.2 × 10^6 /m and $\alpha = 0°$.

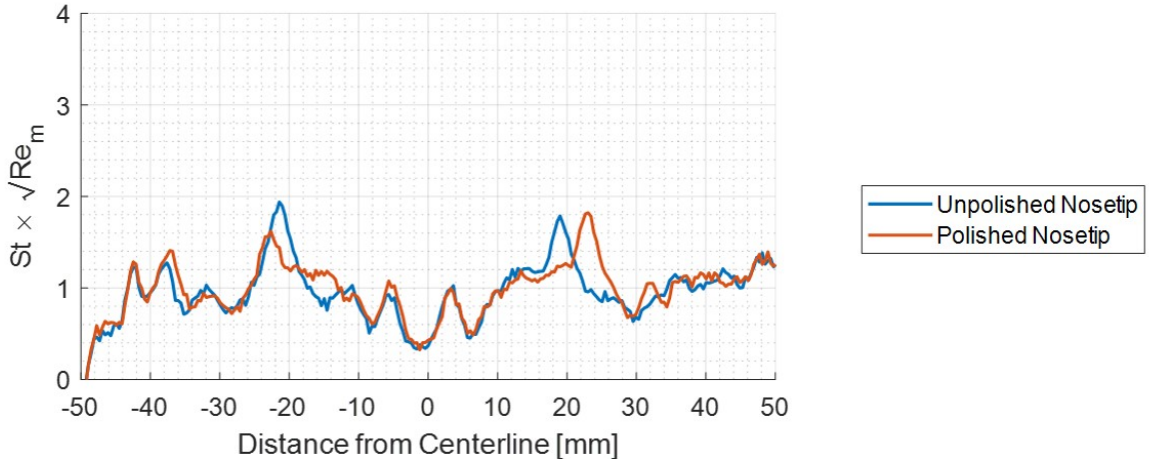

Figure 5.26. Spanwise cuts of heating at x/L = 0.98 (x = 283 mm) with the unpolished and polished smooth-wall nosetips. Re = 10.2 × 10^6 /m and $\alpha = 0°$.

The power spectra of pressure fluctuations at PCB1 and PCB2 with the polished smooth-wall nosetip installed are shown in Figure 5.27. At PCB1, pressure fluctuations were minimal. The power spectra at the different freestream Reynolds numbers are collapsed onto a similar profile and are near the unpolished, smooth-wall measurement. At PCB2, a 250 kHz peak frequency was measured that grows with the increasing freestream Reynolds numbers. It appears that there was an instability at the PCB2 location. It is unclear if the growth of the instability was driven by the lower surface roughness of the polished nosetip, or if it was caused by a slight difference in the nosetip geometry.

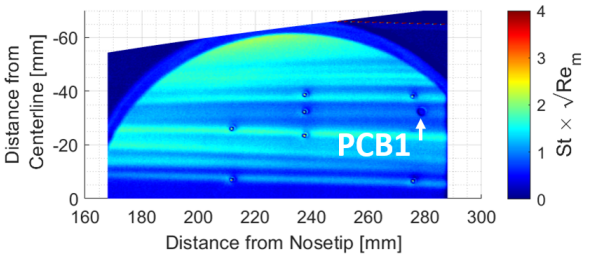

(a) PCB1 Location.

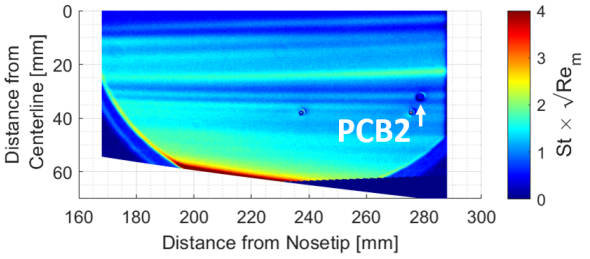

(b) PCB2 Location.

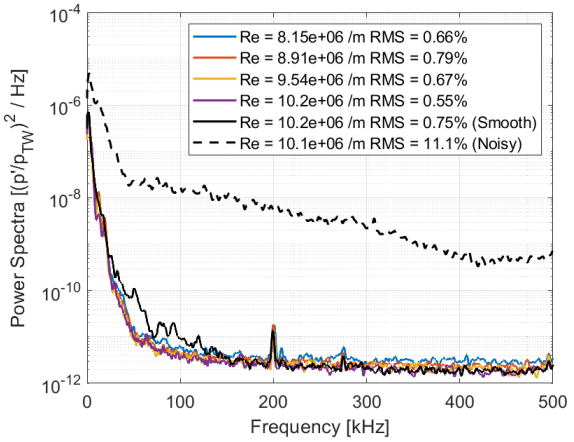

(c) PCB1.

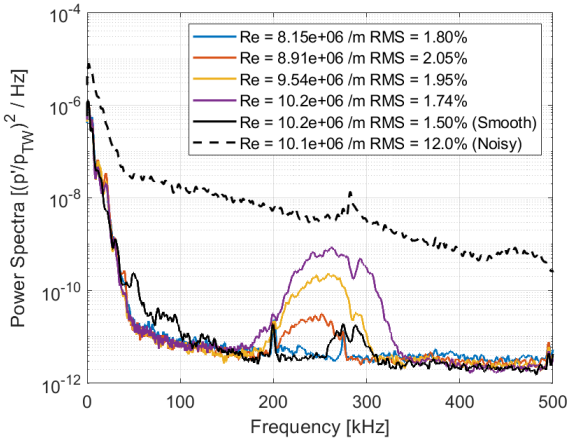

(d) PCB2.

Figure 5.27. PCB1 and PCB2 PSD plots with the polished nosetip installed at different freestream Reynolds numbers and $\alpha = 0°$.

Pressure fluctuations at the Kulites were minimal and similar to the unpolished, smooth-wall measurements. The spectral content of the pressure fluctuations do not show any indications of a growing instability as the freestream Reynolds number increases. Pressure fluctuation data at lower freestream Reynolds numbers are available in the archive, but are not shown due to the lack of a growth of an instability.

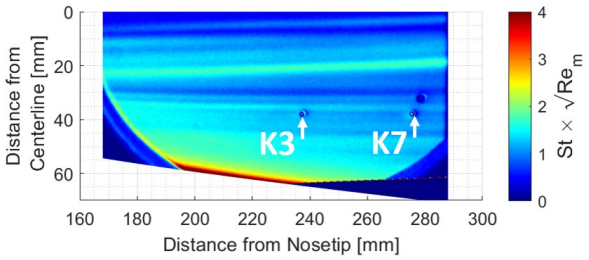

(a) Port side Kulites.

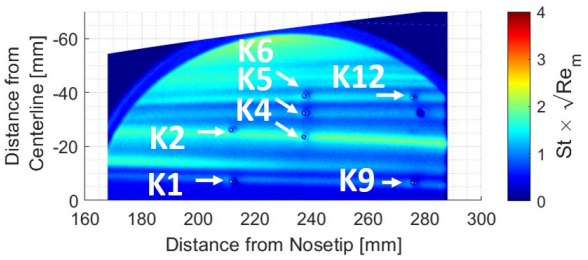

(b) Starboard side Kulites.

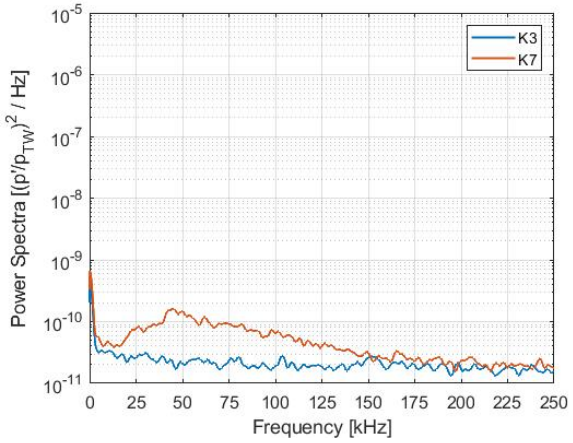

(c) Kulite PSD on the port side.

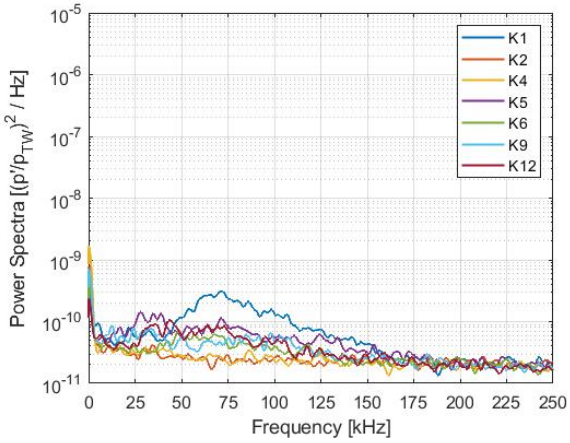

(d) Kulite PSD on the starboard side.

Figure 5.28. Kulite PSD plots with the 0.305 mm forward-facing step installed at $\alpha = 0°$ and Re $= 10 \times 10^6$ /m.

5.2 Measurements at Angles of Attack

The BOLT model was pitched at a 2° and 4° angle of attack, with the PEEK experiment surface facing the windward direction. These experiments were also performed during Entry 3. A 0.20° to 0.30° yaw angle was measured after adjusting the angle of attack, with the port side of the model still facing the windward direction.

5.2.1 Baseline Measurements

Experiments with the unpolished, smooth-wall nosetip were first performed to establish the baseline flow characteristics at these angles of attack. The scaled heating contours at a 2° and 4° angle of attack and at the maximum quiet pressure are shown in Figure 5.29. The magnitude of heating appears to be more intense at the higher angles of attack. At a 4° angle of attack, a thin wedge of heating was observed on the port side of the experiment surface and was located directly over the K3 and K7 sensor faces. A similar wedge of heating was not observed on the starboard side of the model. It is thought that the asymmetry was caused by a combination of the residual yaw angle and asymmetries in the model geometry.

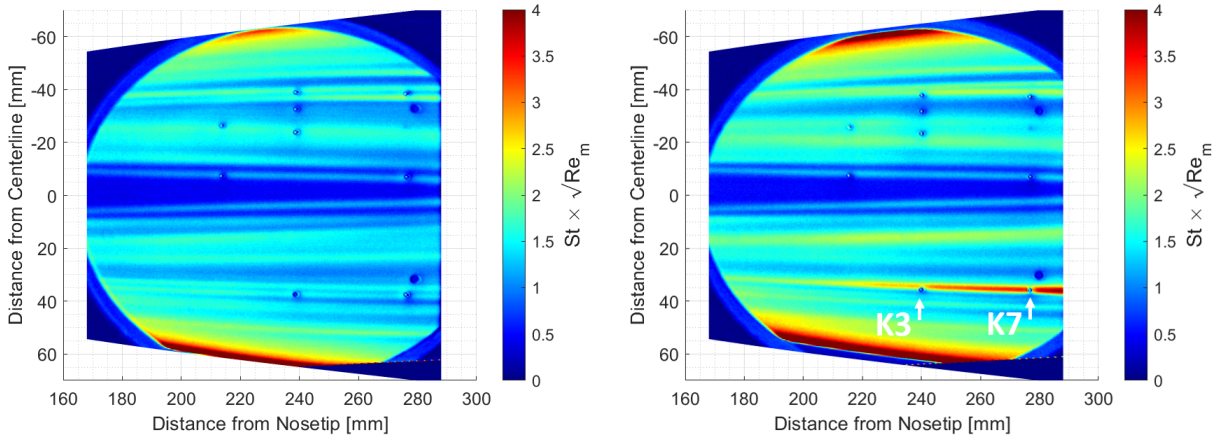

(a) $\alpha = 2°$ (Run 122)

(b) $\alpha = 4°$ (Run 78)

Figure 5.29. Scaled heating contours with the unpolished, smooth-wall nosetip at different angles of attack. Re $\approx 10 \times 10^6$ /m.

Spanwise cuts of heating from each angle of attack and at different freestream Reynolds numbers are shown in Figure 5.30. At a 2° angle of attack, heating magnitudes were relatively

uniform. There was a slight increase in heating magnitudes near - 40 mm from the centerline. At a 4° angle of attack, a sharp increase in heating was measured + 36 mm from the centerline and is representative of the thin wedge of heating. The thin wedge of heating becomes more intense as the freestream Reynolds number increases. The onset of heating grows rapidly and appears to represent a turbulent flow. However, the sensors nearby and directly underneath this heating pattern must be analyzed to confirm the boundary-layer state.

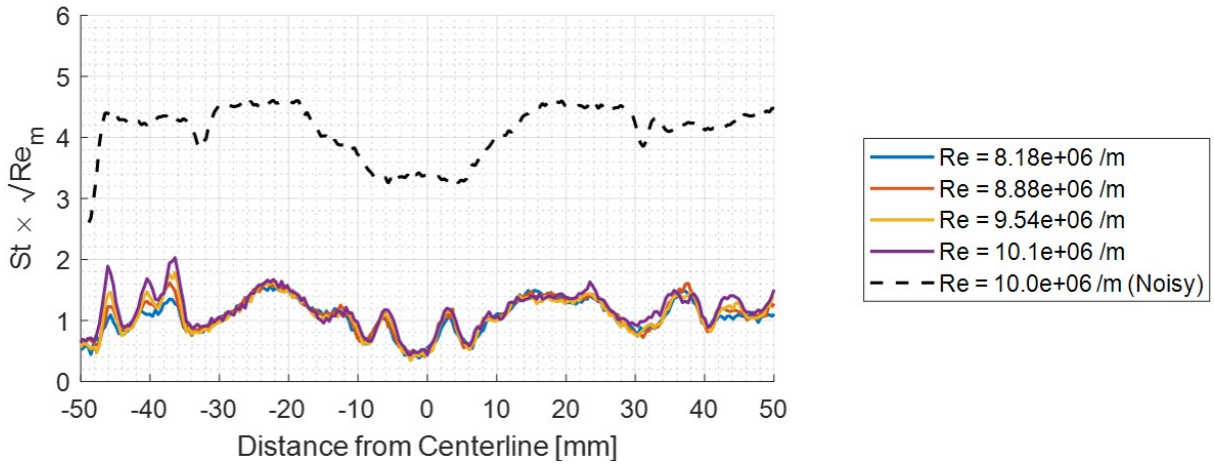

(a) $\alpha = 2°$ (Runs 122 through 127)

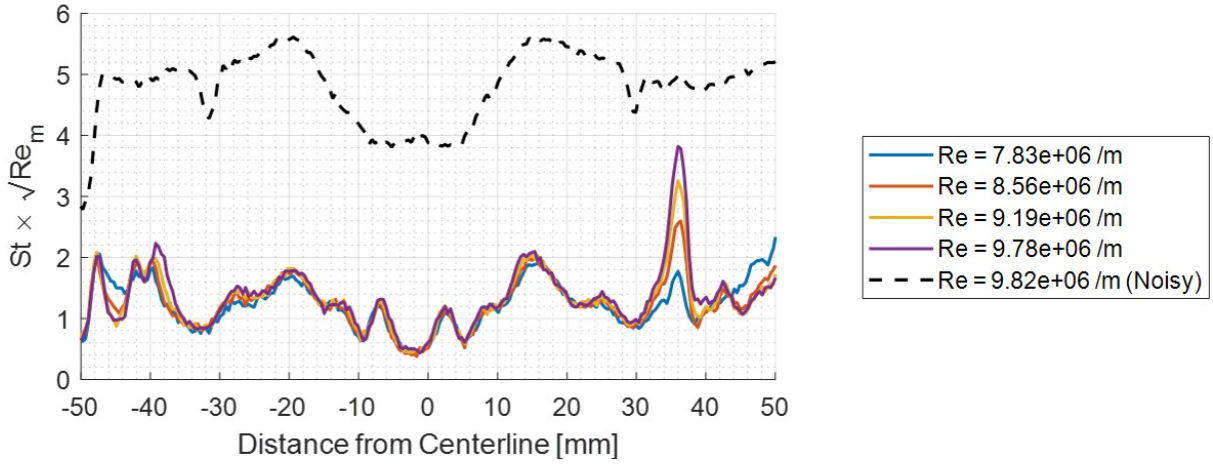

(b) $\alpha = 4°$ (Runs 78 through 81)

Figure 5.30. Spanwise cuts of heating at x/L = 0.98 with the unpolished, smooth-wall nosetip at different angles of attack.

Zoomed-in heating contours of the port side of the experiment surface are shown in Figure 5.31 to show the development of the thin wedge as the freestream Reynolds number increases. The K3 and K7 power spectra are also shown at the different freestream Reynolds numbers. At a 4° angle of attack, there was no significant increase in frequency content at either sensor location despite the streak passing directly over the sensor faces. The streak does not appear to introduce a significant disturbance at the nearby Kulite locations.

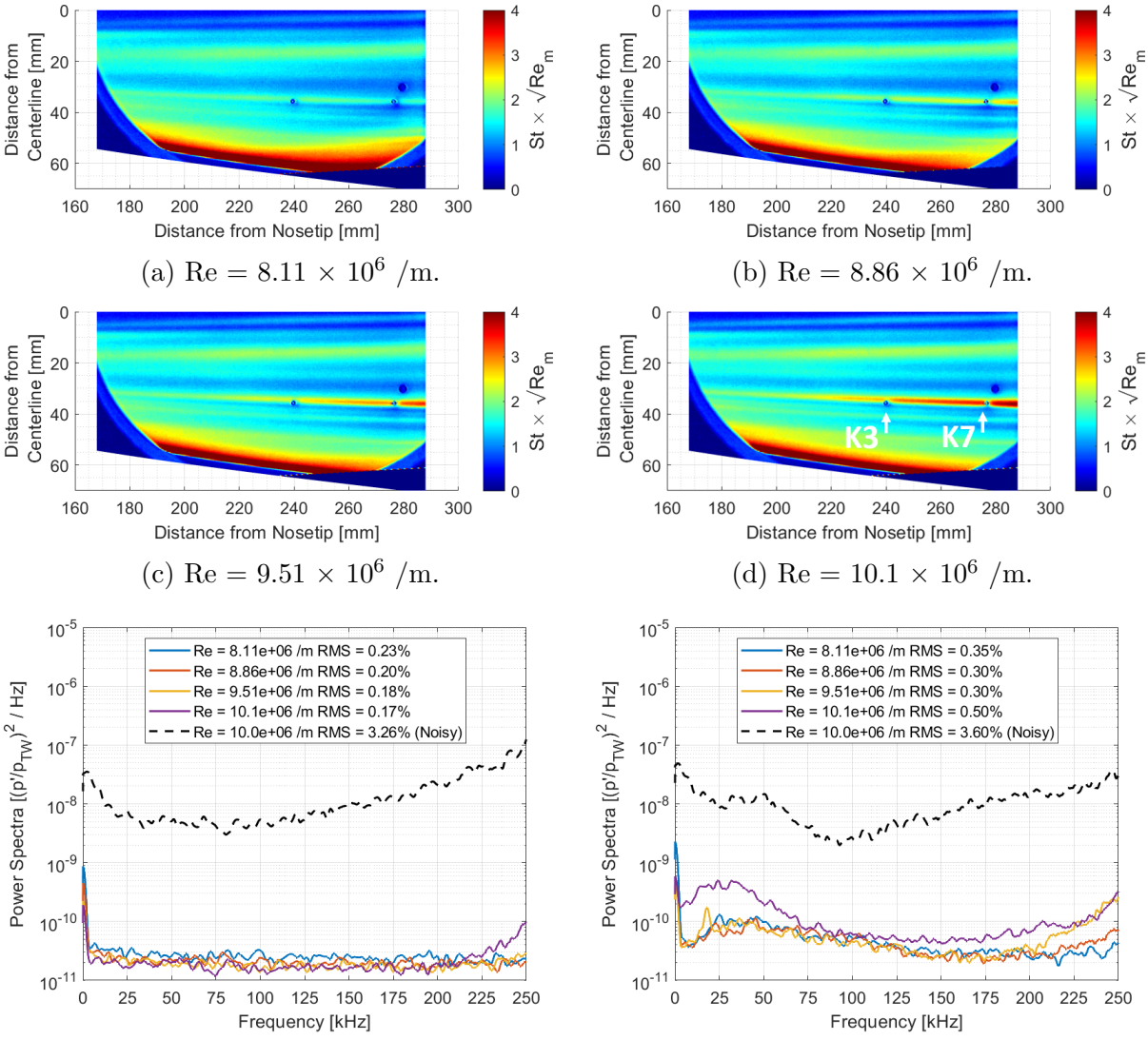

(a) Re = 8.11 × 10^6 /m.

(b) Re = 8.86 × 10^6 /m.

(c) Re = 9.51 × 10^6 /m.

(d) Re = 10.1 × 10^6 /m.

(e) K3 PSD.

(f) K7 PSD.

Figure 5.31. Zoomed-in heating contours and the K3 and K7 power spectra at different freestream Reynolds numbers with the unpolished, smooth-wall nosetip at $\alpha = 4°$.

5.2.2 Measurements with the Backward-Facing Steps

Both backward-facing steps had a significant impact on the surface heating characteristics and the pressure fluctuations in the flow. The scaled heating contours at 2° and 4° angles of attack with the 0.508 mm and the 1.016 mm backward-facing steps are shown in Figures 5.32 and 5.33, respectively. With the 0.508 mm step at a 2° angle of attack, two wedges of heating form on the port side of the experiment surface. The inboard wedge appears to be wider and more intense than the outboard wedge. A single wedge of heating forms on the starboard side of the experiment surface. When the angle of attack was increased to 4°, a wider and further upstream wedge was observed on the port side of the experiment surface. No wedges of heating were observed on the starboard side of the experiment surface. The cause of this asymmetry is unknown.

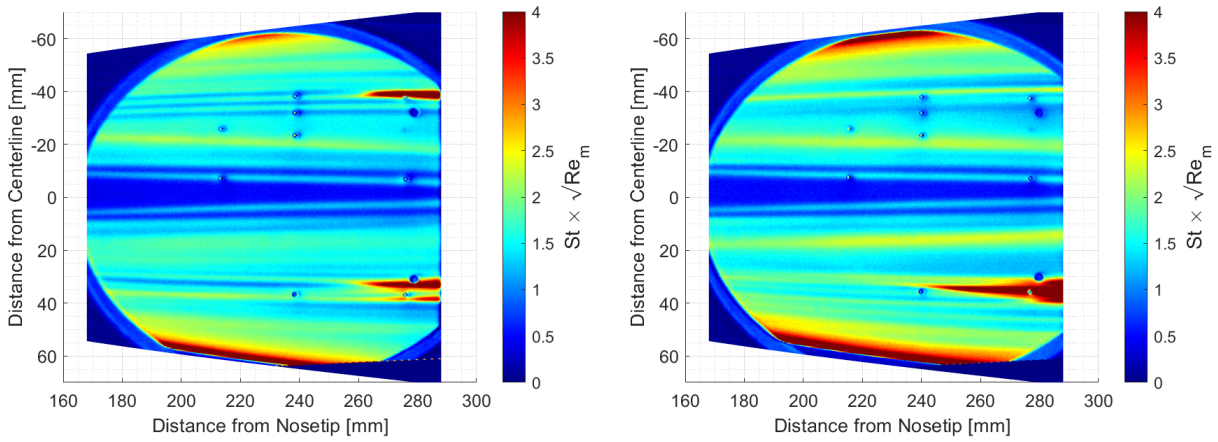

(a) $\alpha = 2°$ (Run 110)

(b) $\alpha = 4°$ (Run 92)

Figure 5.32. Scaled heating contours with the 0.508 mm backward-facing step at different angles of attack. Re $\approx 10 \times 10^6$ /m.

Wider wedges of heating that form at a further upstream location were measured with the larger 1.016 mm step. The wedges of heating were observed on both sides of the experiment surface, although the wedge on the port side was consistently wider. This might be a result of the residual yaw angle. At a 4° angle of attack, both wedges of heating form at a further upstream location and appear to be wider when compared to the wedges of heating that were measured at a 2° angle of attack.

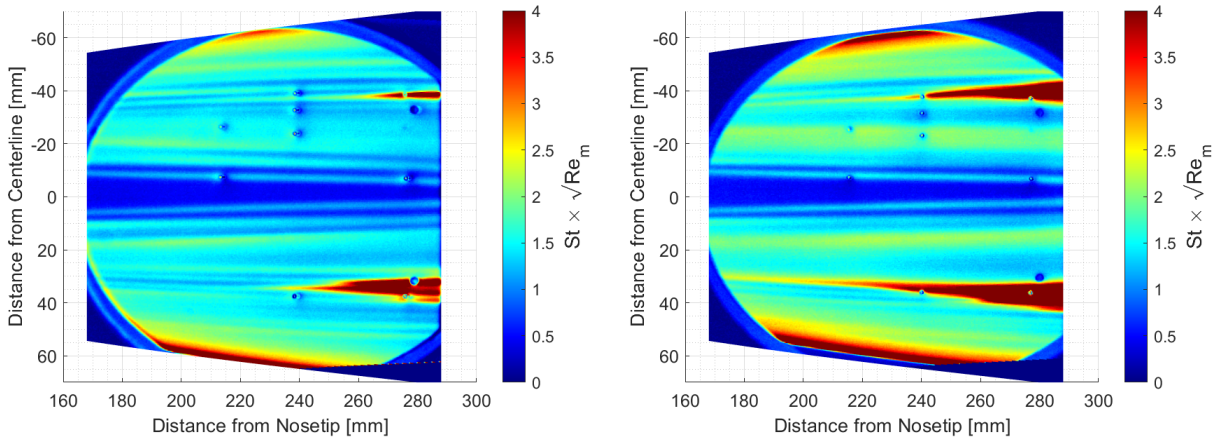

(a) $\alpha = 2°$ (Run 140)

(b) $\alpha = 4°$ (Run 65)

Figure 5.33. Scaled heating contours with the 1.016 mm backward-facing step at different angles of attack. Re $\approx 10 \times 10^6$ /m.

Spanwise cuts of heating with the 0.508 mm and 1.016 mm backward-facing steps at different freestream Reynolds numbers are plotted in Figures 5.34 and 5.35. For both backward-facing steps, a similar development of the wedges of heating was measured. As the freestream Reynolds number increases, the wedges of heating widen and the heating magnitudes increase. As the angle of attack increases, the wedges of heating also widen and grow more intense. The heating magnitudes appear to level out near noisy flow levels, which might suggest that the flow has become fully turbulent. The increase in heating was observed between 30 mm and 50 mm from the centerline. The heating magnitudes between 0 mm and 30 mm from the centerline were similar to the unpolished, smooth-wall measurement.

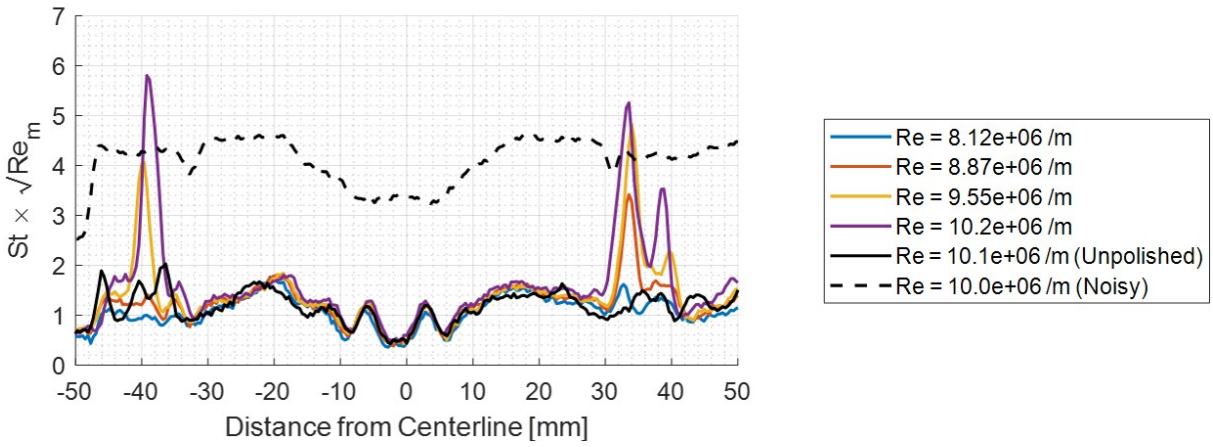

(a) $\alpha = 2°$ (Runs 110 through 113)

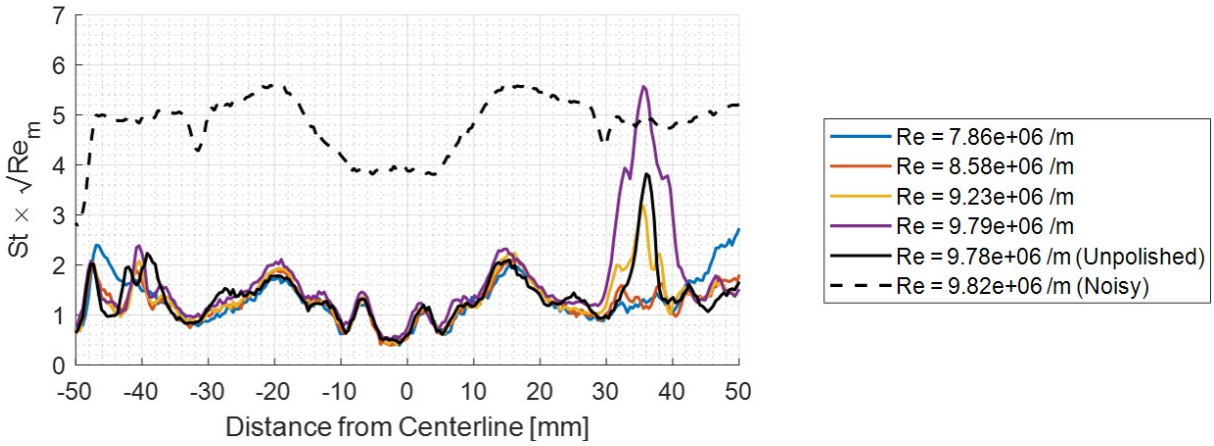

(b) $\alpha = 4°$ (Runs 92 through 95)

Figure 5.34. Spanwise cuts of heating at x/L = 0.98 with the 0.508 mm backward-facing step at different angles of attack.

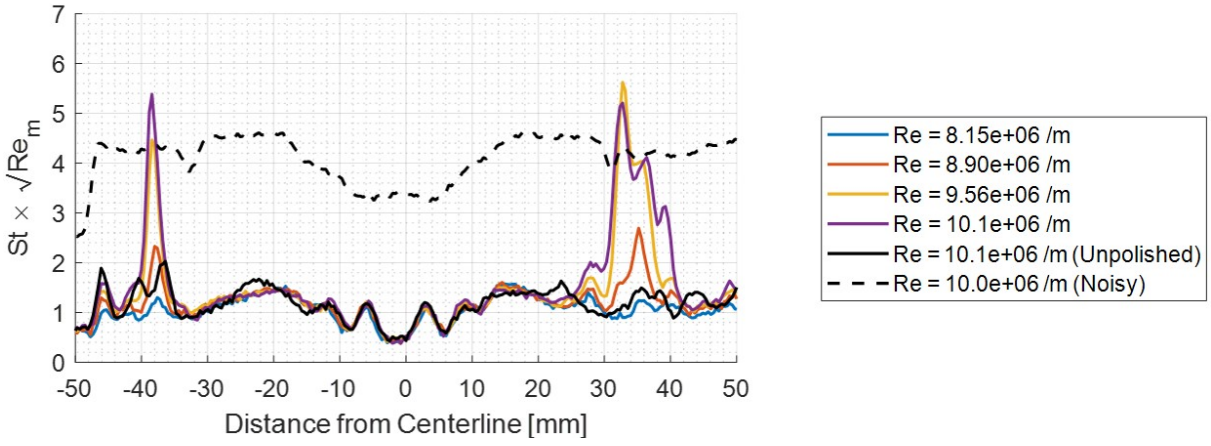

(a) $\alpha = 2°$ (Runs 140 through 143)

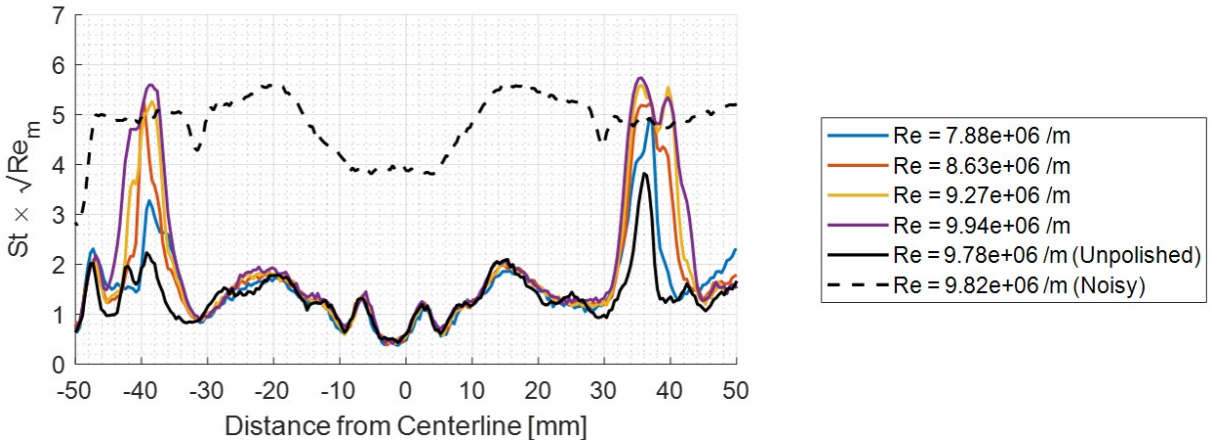

(b) $\alpha = 4°$ (Runs 65 through 68)

Figure 5.35. Spanwise cuts of heating at x/L = 0.98 with the 1.016 mm backward-facing step at different angles of attack.

Kulite sensors near these wedges of increased heating measured a significant increase in pressure fluctuations when compared to the unpolished, smooth-wall measurement. Zoomed-in heating contours and PSDs of the pressure fluctuations at K3 and K7 are shown to illustrate this. The measurements in Figure 5.36 are with the 1.016 mm backward-facing step at a 2° angle of attack. As the wedge of heating forms at a freestream Reynolds number of 8.90×10^6 /m, RMS pressure fluctuation magnitudes at K7 increase. This can be seen in the elevated RMS pressure fluctuation magnitudes and the increase in broadband frequency content in the power spectra. At a freestream Reynolds number of 10.1×10^6 /m, the wedge of heating has progressed upstream and is close to the K3 sensor face. This is reflected in the K3 power spectra, which show additional frequency content that is centered around 50 kHz. The RMS pressure fluctuation magnitudes have also increased by a factor of 2 compared to the RMS pressure fluctuation magnitudes at the lower freestream Reynolds numbers.

At a 4° angle of attack, the wedges of heating form at a further upstream location and are wider. A similar comparison of the scaled heating contours and Kulite power spectra are shown in Figure 5.37. The K7 sensor face was directly underneath the wedges of heating at all four freestream Reynolds numbers. The power spectra at K7 are broadband and near noisy flow levels, which are indicative of a turbulent flow. The RMS pressure fluctuation magnitudes are also near noisy flow magnitudes. Pressure fluctuations at K3 gradually increase with the increasing freestream Reynolds numbers, as the wedge of heating widens and moves closer to the K3 sensor face.

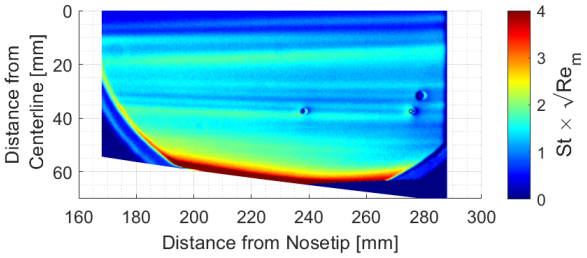

(a) Re = 8.15 × 10^6 /m.

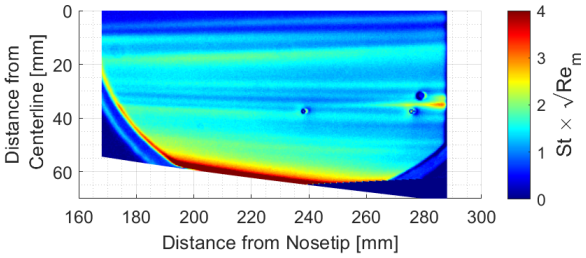

(b) Re = 8.90 × 10^6 /m.

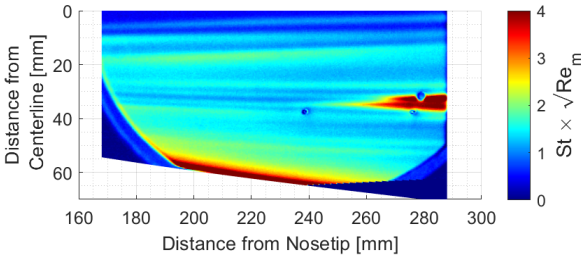

(c) Re = 9.56 × 10^6 /m.

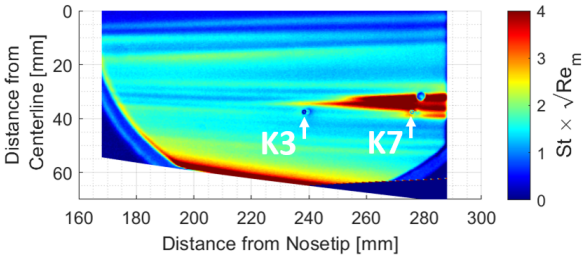

(d) Re = 10.1 × 10^6 /m.

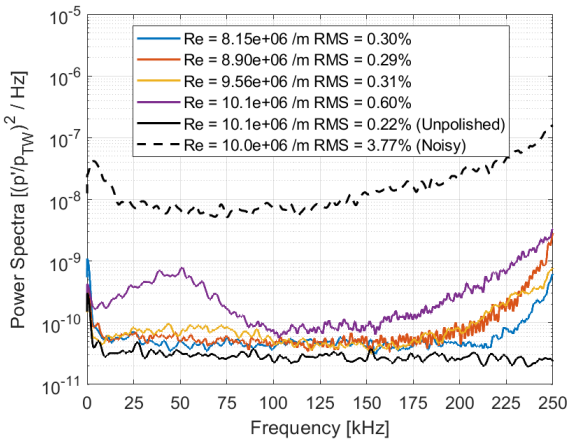

(e) K3 PSD.

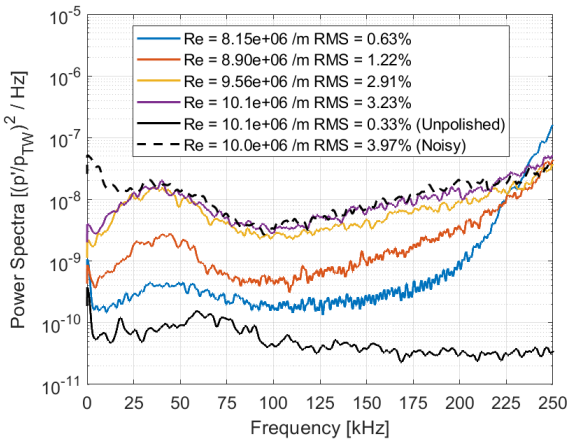

(f) K7 PSD.

Figure 5.36. Zoomed-in scaled heating contours and Kulite power spectra as the freestream Reynolds number increases. k = + 1.016 mm and $\alpha = 2°$.

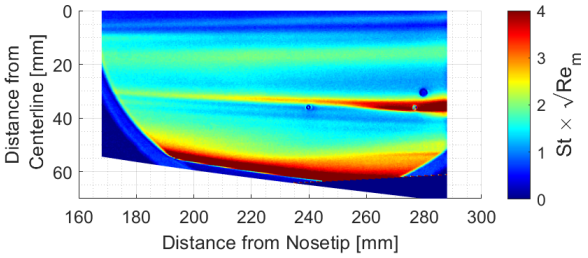

(a) Re = 7.88 × 10^6 /m.

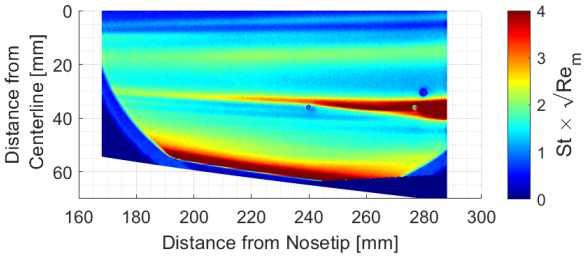

(b) Re = 8.63 × 10^6 /m.

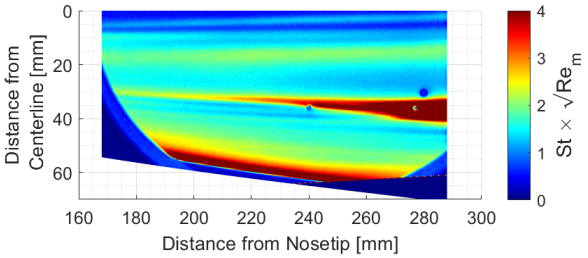

(c) Re = 9.27 × 10^6 /m.

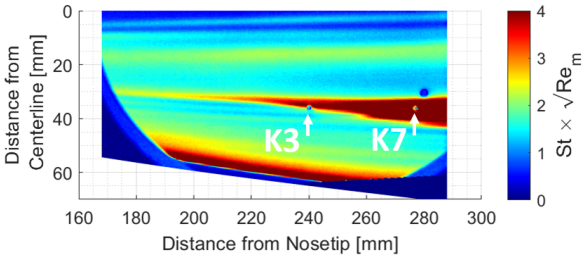

(d) Re = 9.94 × 10^6 /m.

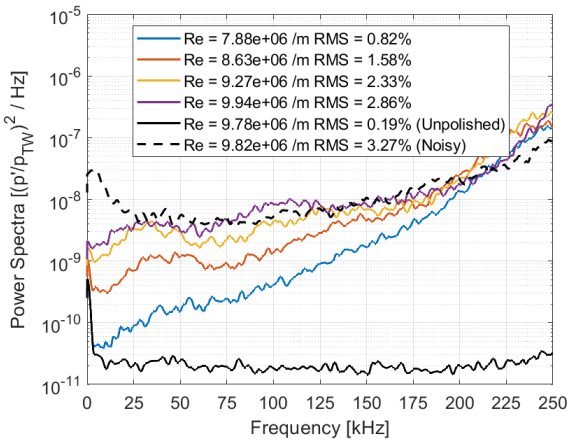

(e) K3 PSD.

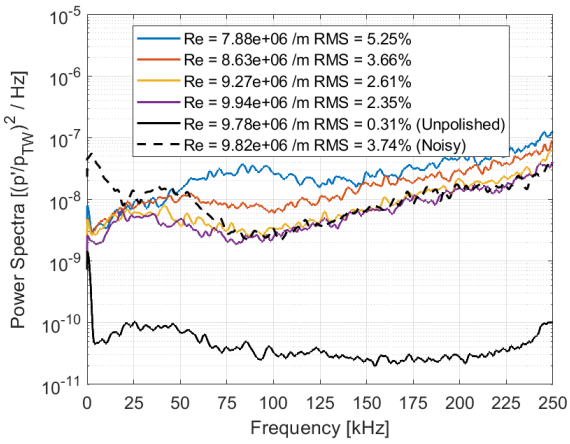

(f) K7 PSD.

Figure 5.37. Zoomed-in scaled heating contours and Kulite power spectra as the freestream Reynolds number increases. k = + 1.016 mm and $\alpha = 4°$.

The K3 and K7 sensors also measure an increase in pressure fluctuations with the smaller 0.508 mm backward-facing step. Plots of the zoomed-in scaled heating contours and the Kulite power spectra at a 2° and 4° angle of attack are shown in Figures 5.38 and 5.39. At a 2° angle of attack, the wedge of heating starts to develop at a freestream Reynolds number of 8.87×10^6 /m. Pressure fluctuations at K7 gradually increase as the freestream Reynolds number increases. The power spectra at K7 show some frequency content that is centered around 25 kHz to 50 kHz. Broadband frequency content was also increasing as the freestream Reynolds number increases. The power spectra at K3 are similar to the unpolished, smooth-wall measurement. Only a small increase in frequency content is seen at the highest freestream Reynolds number of 10.2×10^6 /m.

At a 4° angle of attack, the wedge of heating progresses further upstream and is near the K7 sensor face at a freestream Reynolds number of 9.23×10^6 /m, Figure 5.39c. Elevated pressure fluctuations were measured at this freestream Reynolds number and correspond with the development of the wedge of heating. The power spectra of K7, shown in Figure 5.39f, shows a broadband amplitude and an apparent frequency peak near 50 kHz. This might indicate an instability that is growing near the wedge of heating. The wedge of heating continues to develop and approaches the K3 sensor face at a freestream Reynolds number of 9.79×10^6 /m, Figure 5.39d. RMS pressure fluctuation magnitudes increase by a factor of 3 at the K3 sensor face.

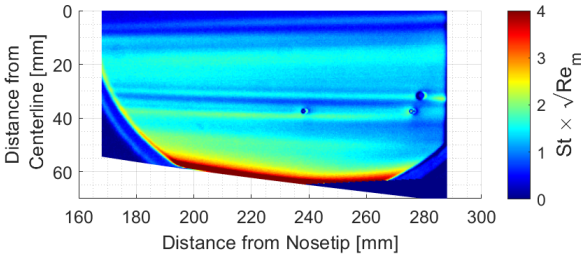

(a) Re = 8.12 × 10^6 /m.

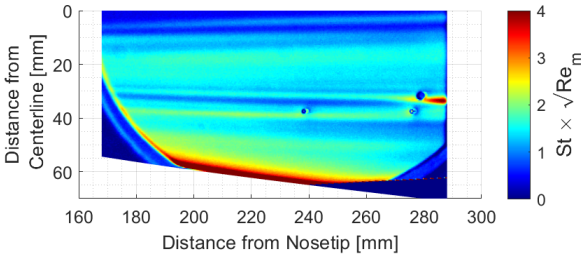

(b) Re = 8.87 × 10^6 /m.

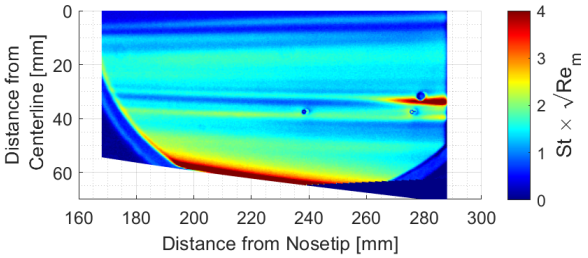

(c) Re = 9.55 × 10^6 /m.

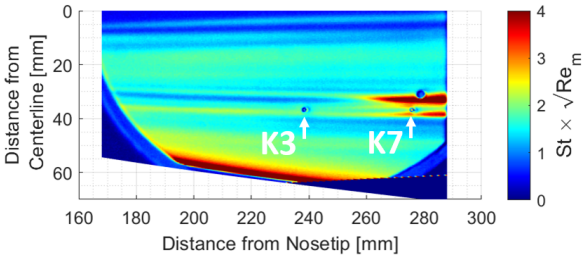

(d) Re = 10.2 × 10^6 /m.

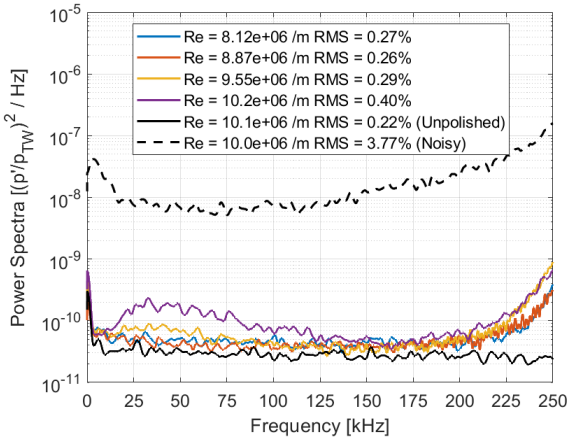

(e) K3 PSD.

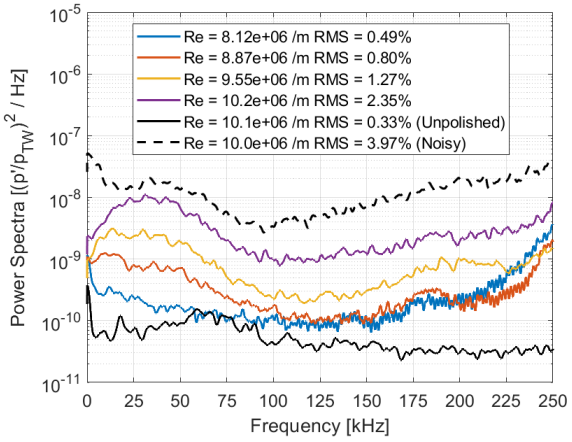

(f) K7 PSD.

Figure 5.38. Zoomed-in scaled heating contours and Kulite power spectra as the freestream Reynolds number increases. k = + 0.508 mm and $\alpha = 2°$.

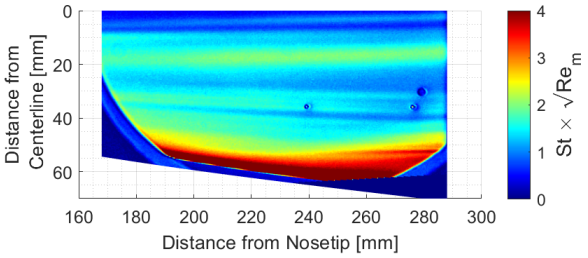

(a) Re = 7.86 × 10^6 /m.

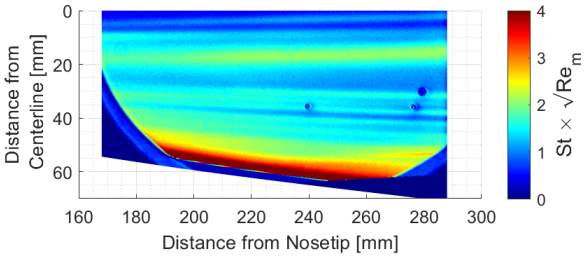

(b) Re = 8.58 × 10^6 /m.

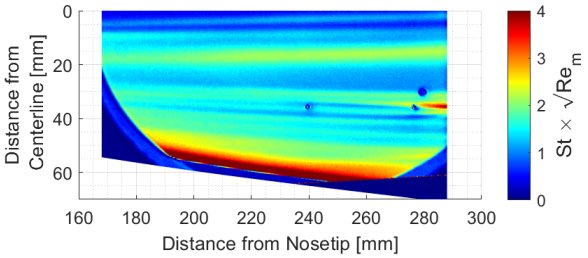

(c) Re = 9.23 × 10^6 /m.

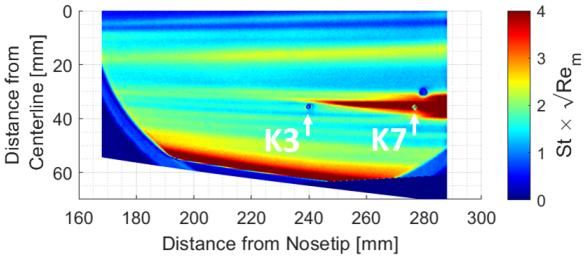

(d) Re = 9.79 × 10^6 /m.

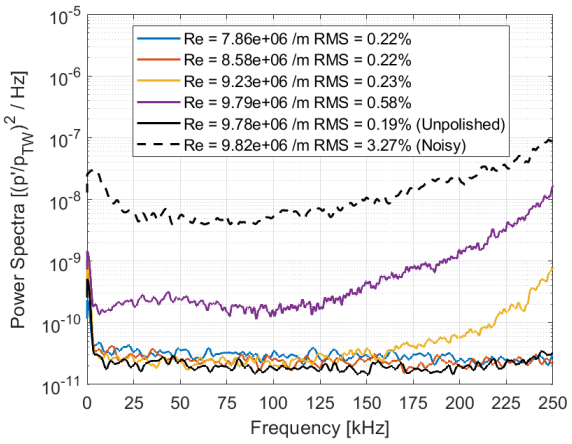

(e) K3 PSD.

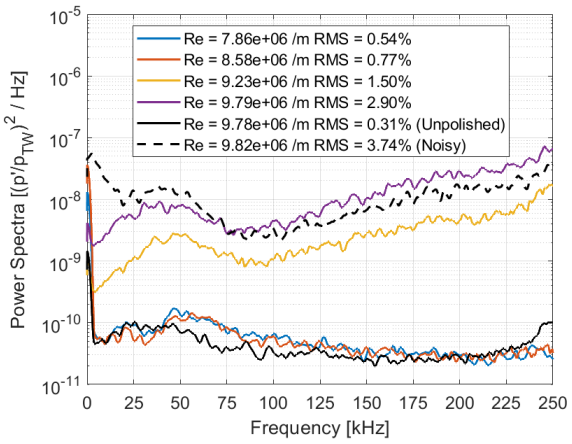

(f) K7 PSD.

Figure 5.39. Zoomed-in scaled heating contours and Kulite power spectra as the freestream Reynolds number increases. k = + 0.508 mm and $\alpha = 4°$.

Increased pressure fluctuations were also measured at PCB2 with the backward-facing steps at angles of attack. Unlike the measurements at a 0° angle of attack, a clear growth of an instability was not identified in the power spectra. With the smaller 0.508 mm step, Figure 5.40c, the power spectra are broadband. Broadband amplitudes increase as the freestream Reynolds numbers increase, but there are no peak frequencies that would represent an instability. With the larger 1.016 mm step, Figure 5.40d, a 250 kHz peak frequency is seen at the freestream Reynolds number of 8.15 $\times$ 10^6 /m. As the freestream Reynolds number increases, the power spectra becomes broadband and indicates that the boundary layer has become turbulent. The 250 kHz peak might be representative of an instability that breaks down at a freestream Reynolds number of 8.90 $\times$ 10^6 /m.

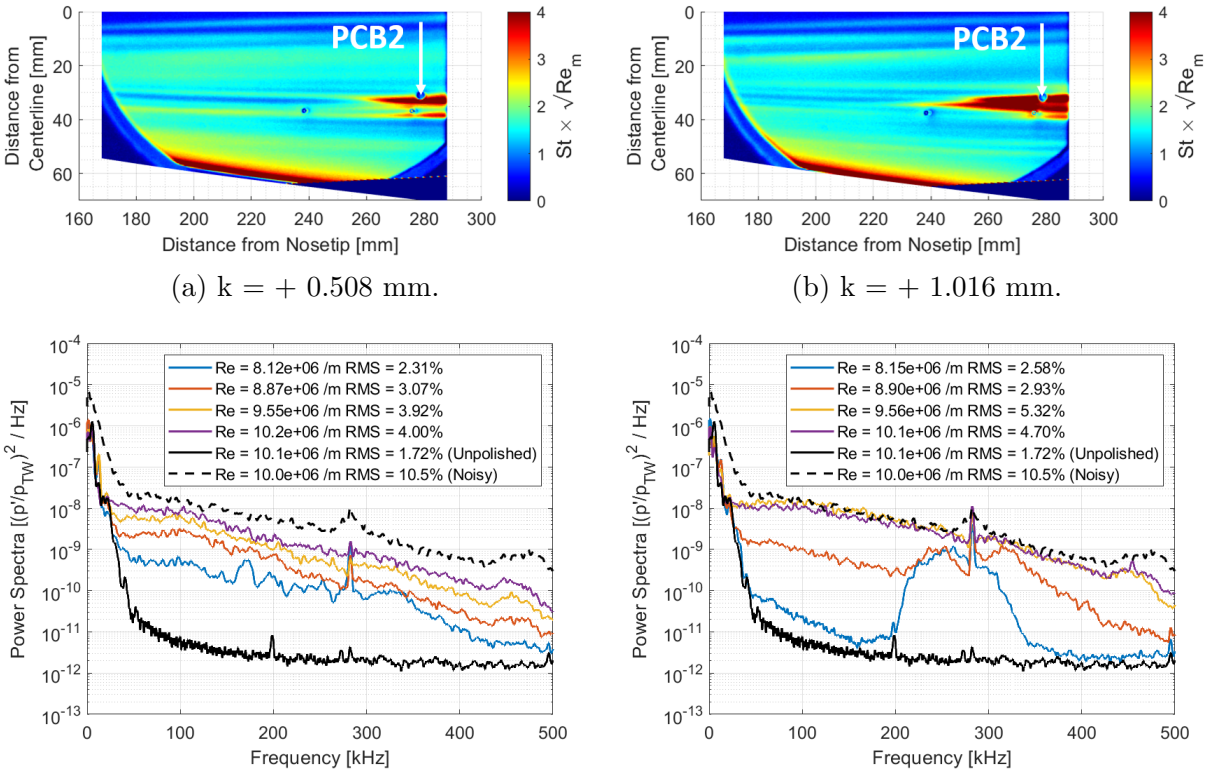

(a) k = + 0.508 mm.

(b) k = + 1.016 mm.

(c) k = + 0.508 mm.

(d) k = + 1.016 mm.

Figure 5.40. PCB2 power spectra near the wedges of heating that form with the backward-facing steps at $\alpha = 2°$.

At a 4° angle of attack, the wedge of heating is located further outboard and does not appear to envelop the PCB2 sensor face. The zoomed-in heating contours and PCB2 power spectra for both backward-facing steps are shown in Figure 5.41. The power spectra are of a lower amplitude when compared to the measurements at a 2° angle of attack. The RMS pressure fluctuation magnitudes are also lower. It is thought that the pressure fluctuations at the PCB2 sensor location were lower because the sensor face was further away from the wedge of heating. A sharp 282 kHz peak frequency is seen in both power spectra and is thought to be caused by a sensor resonance.

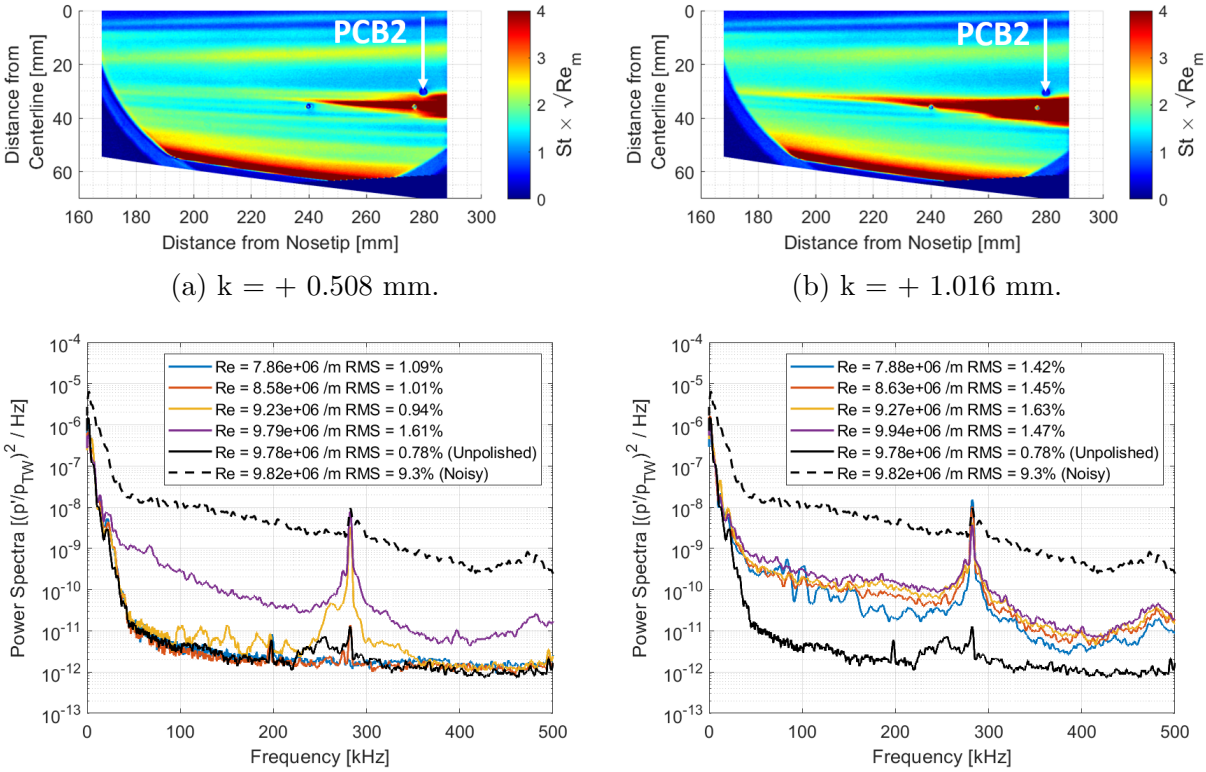

(a) k = + 0.508 mm.

(b) k = + 1.016 mm.

(c) k = + 0.508 mm.

(d) k = + 1.016 mm.

Figure 5.41. PCB2 power spectra near the wedges of heating that form with the backward-facing steps at $\alpha = 4°$.

5.2.3 Measurements with the Forward-Facing Steps

Each of the forward-facing steps was tested at 2° and 4° angles of attack. The effects of the forward-facing steps were also magnified on the windward side of the model. Scaled heating contours at a 2° angle of attack and at a freestream Reynolds number near 10×10^6 /m are shown in Figure 5.42. Wedges of heating were observed on the port side of the experiment surface with the 0.152 mm and 0.305 mm steps. The heating magnitudes were more intense with the larger 0.305 mm step.

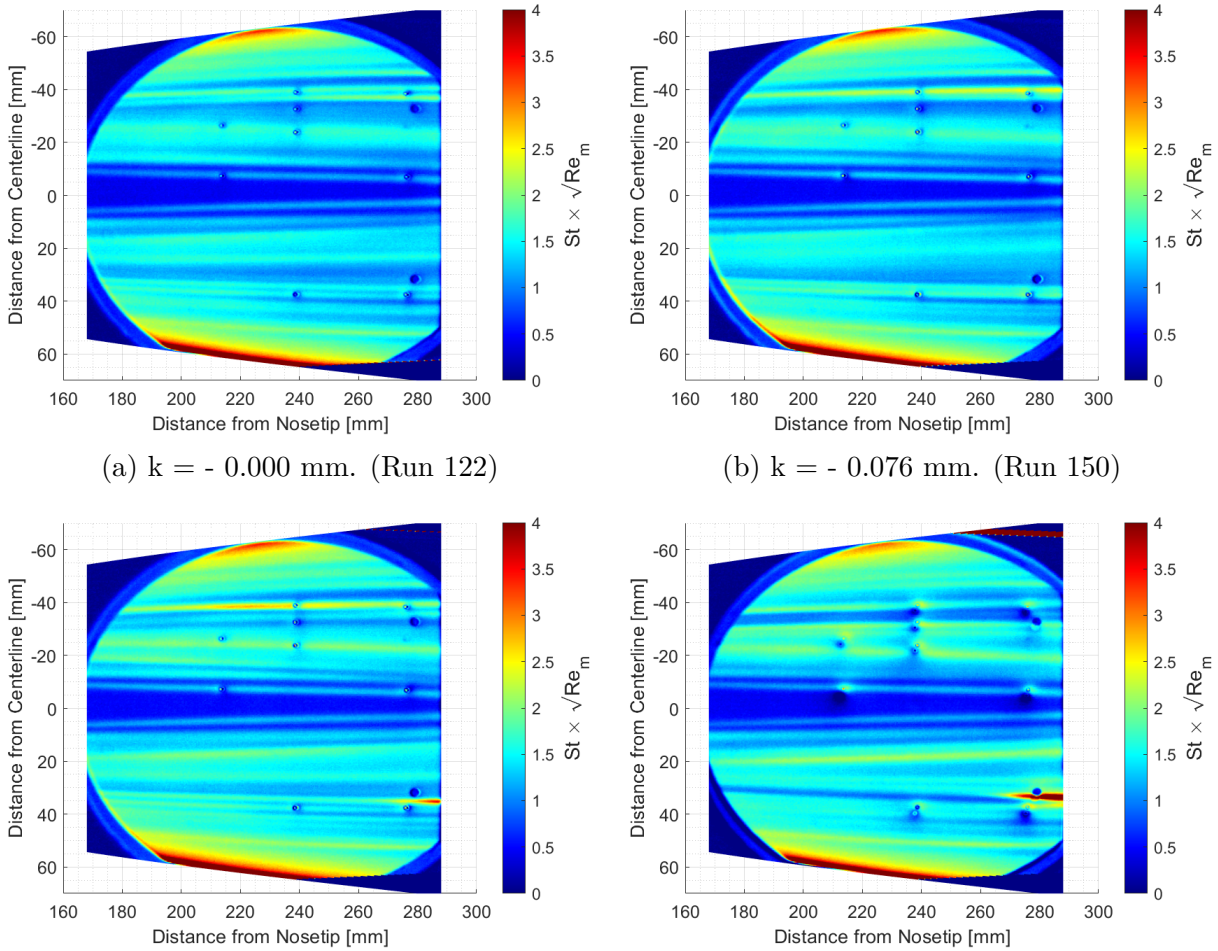

(a) k = - 0.000 mm. (Run 122)

(b) k = - 0.076 mm. (Run 150)

(c) k = - 0.152 mm. (Run 146)

(d) k = - 0.305 mm. (Run 117)

Figure 5.42. Scaled heating contours with the forward-facing steps at $\alpha = 2°$. Re = 10×10^6 /m.

At a 4° angle of attack, the effects of the steps are more apparent. The scaled heating contours at a freestream Reynolds number of approximately 10 $\times$ 10^6 /m are shown in Figure 5.43. Thin wedges of heating were measured near 35 mm from the centerline with the 0.076 mm and 0.152 mm steps. These heating patterns are similar to the smooth-wall measurements. An intense wedge of heating was measured with the 0.305 mm step, but only on the port side of the experiment surface.

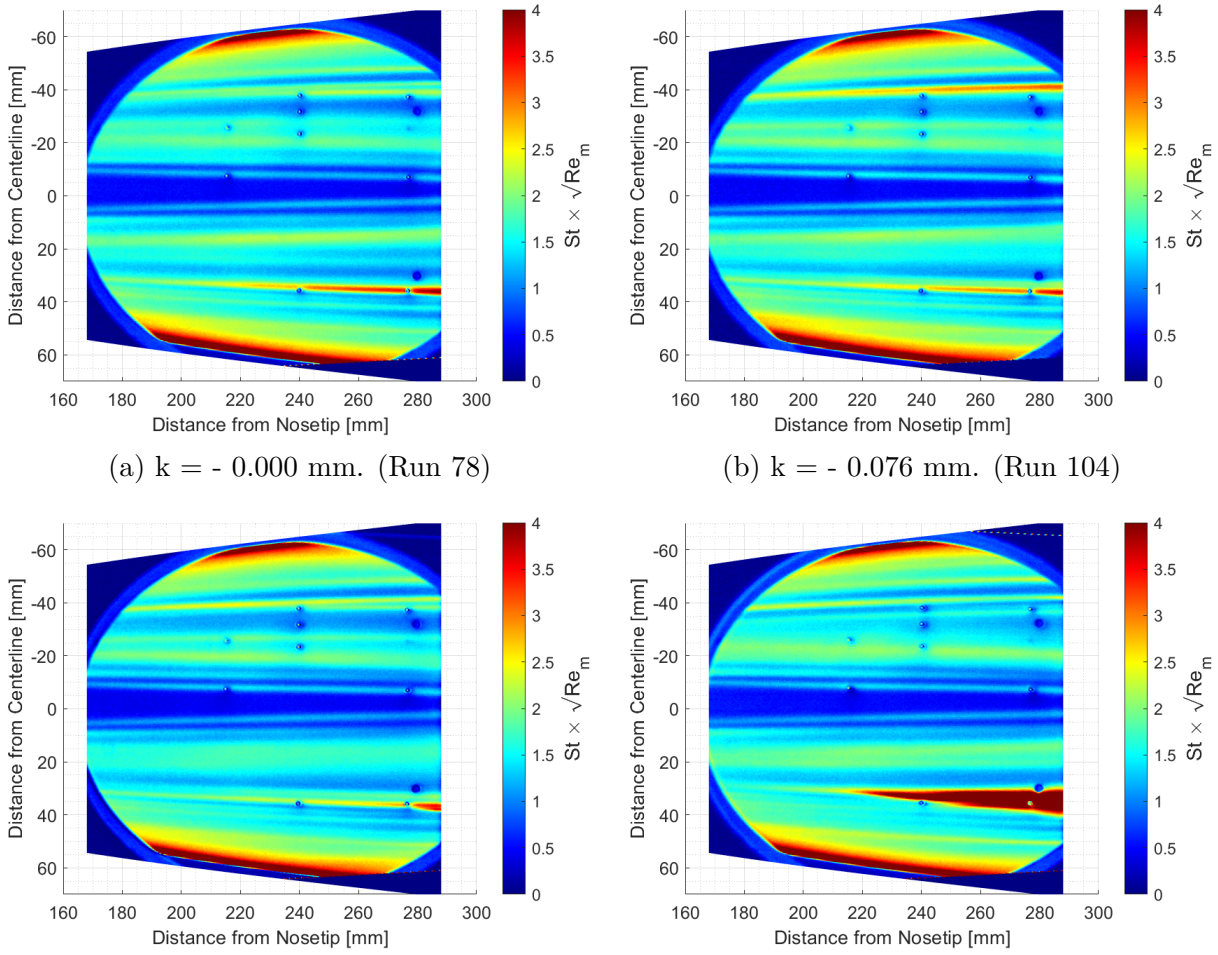

(a) k = - 0.000 mm. (Run 78)

(b) k = - 0.076 mm. (Run 104)

(c) k = - 0.152 mm. (Run 98)

(d) k = - 0.305 mm. (Run 71)

Figure 5.43. Scaled heating contours with the forward-facing steps at $\alpha = 4°$. Re = 10 $\times$ 10^6 /m.

Increased pressure fluctuations were only measured near the wedge that was measured with the largest 0.305 mm forward-facing step. Zoomed-in scaled heating contours that show the development of the wedge of heating and the power spectra of pressure fluctuations at K3 and K7 are shown in Figure 5.44. At K7, the RMS pressure fluctuation magnitudes increase as the wedge develops on the experiment surface. A broadband increase in frequency content is seen in the power spectra, Figure 5.44f. Pressure fluctuations at K3 were minimal and near the unpolished, smooth-wall measurement.

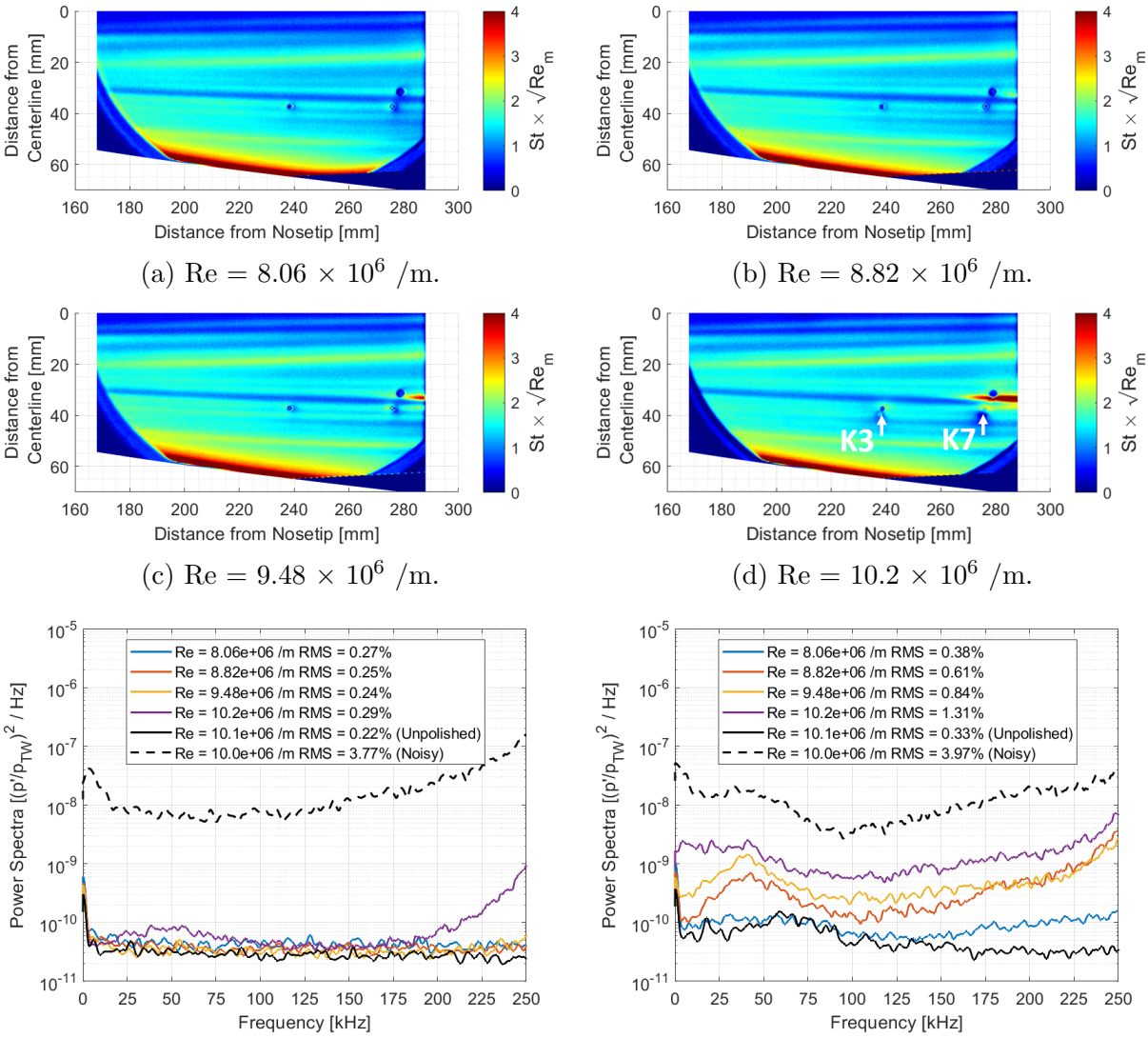

(a) Re = 8.06 × 10^6 /m.

(b) Re = 8.82 × 10^6 /m.

(c) Re = 9.48 × 10^6 /m.

(d) Re = 10.2 × 10^6 /m.

(e) K3 PSD.

(f) K7 PSD.

Figure 5.44. Zoomed-in scaled heating contours and Kulite power spectra as freestream Reynolds number increases. k = - 0.305 mm and $\alpha = 2°$.

At a 4° angle of attack, the wedge of heating was measured at the lowest freestream Reynolds number that was tested, 7.87 × 10^6 /m. The wedge forms directly over the K7 sensor face. The power spectra of K7, shown in Figure 5.45, are near noisy flow levels and indicate that the wedge is likely a turbulent flow. The power spectra at K3 grow as the freestream Reynolds number increases. The turbulent wedge is located close to K3 sensor face and likely causes this increase in pressure fluctuations.

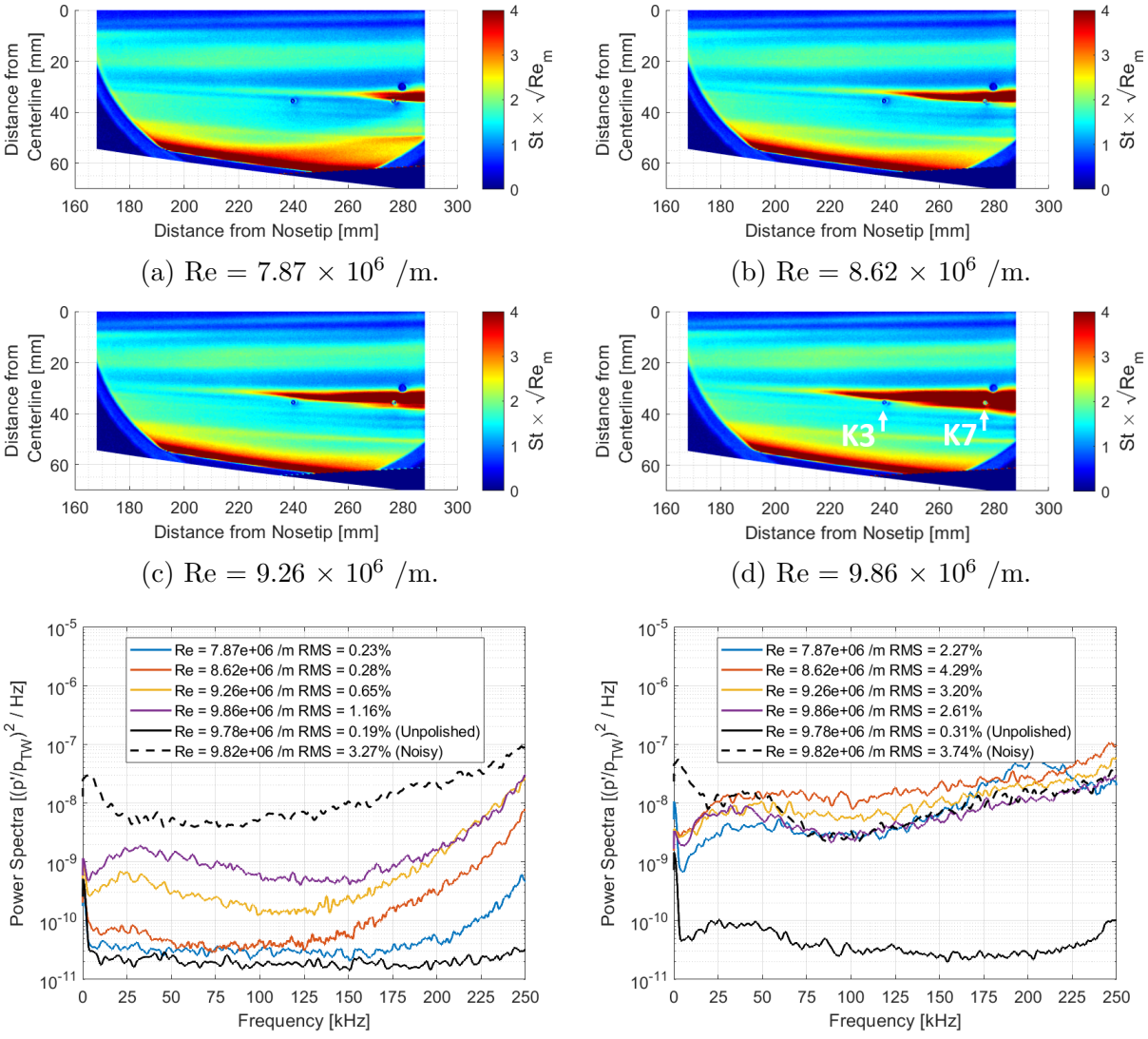

(a) Re = 7.87 × 10^6 /m.

(b) Re = 8.62 × 10^6 /m.

(c) Re = 9.26 × 10^6 /m.

(d) Re = 9.86 × 10^6 /m.

(e) K3 PSD.

(f) K7 PSD.

Figure 5.45. Scaled heating contours and Kulite power spectra as freestream Reynolds number increases. k = - 0.305 mm and $\alpha = 4°$.

The PCB2 sensor was also located near the wedges of heating. No instabilities were identified in the pressure fluctuations. Scaled heating contours and the PCB2 power spectra with the 0.176 mm and 0.305 mm forward-facing steps are shown in Figure 5.46. There is minimal frequency content in the power spectra with the 0.176 mm step, with the exception of a 282 kHz peak that is thought to be caused by a sensor resonance. This was similar to what was observed with the backward-facing steps at a 4° angle of attack. With the 0.305 mm step, the broadband frequency content in the power spectra grows with increasing freestream Reynolds numbers. There are no peak frequencies that would indicate an instability in the boundary layer.

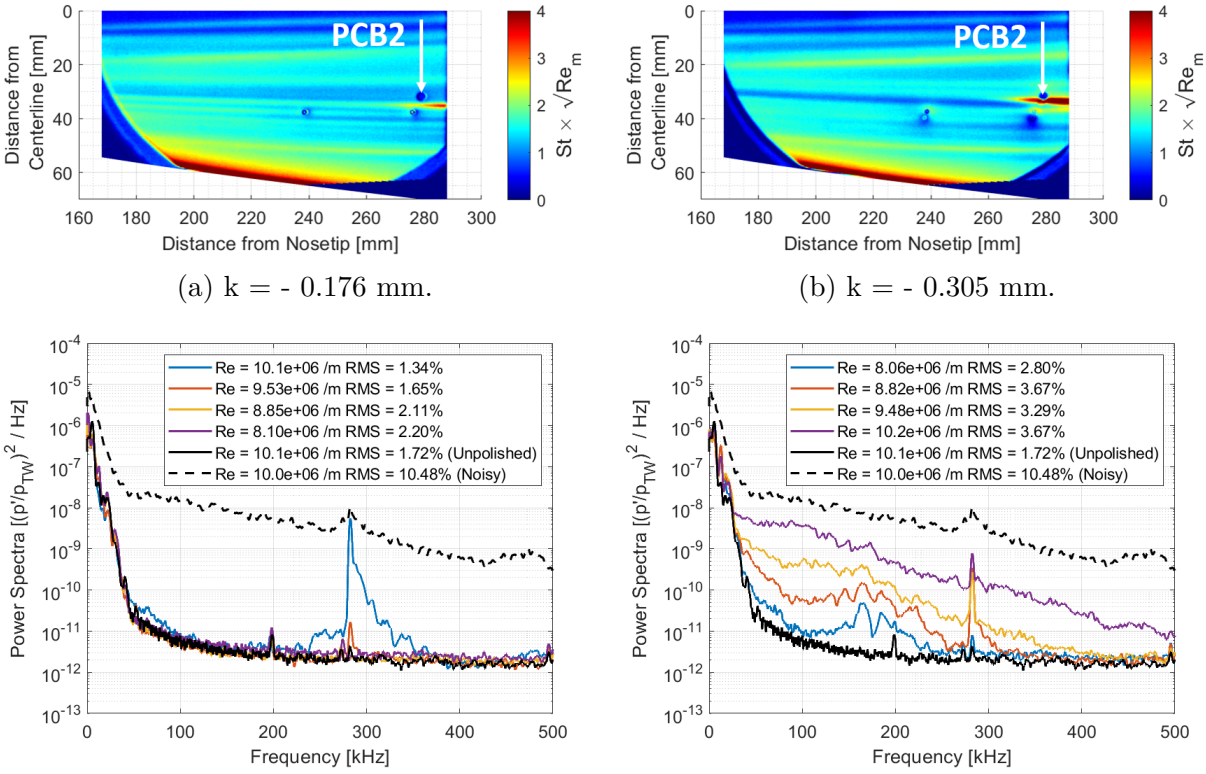

(a) k = - 0.176 mm.

(b) k = - 0.305 mm.

(c) k = - 0.176 mm.

(d) k = - 0.305 mm.

Figure 5.46. PCB2 power spectra near the wedges of heating that form with the backward-facing steps at $\alpha = 2°$.

A similar trend was observed at a 4° angle of attack with these forward-facing steps. The scaled heating contours and PCB2 power spectra are shown in Figure 5.47. With the smaller 0.176 mm step, the power spectra at the different freestream Reynolds numbers were similar to the unpolished, smooth-wall measurement and collapse onto a similar profile. With the larger 0.305 mm step, a broadband increase in frequency content can be seen in the power spectra as the freestream Reynolds number increases. The sharp 282 kHz peak was measured and thought to be caused by a sensor resonance.

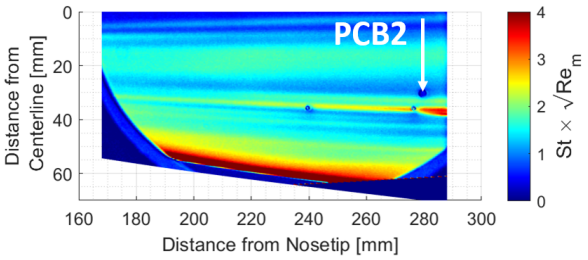

(a) k = + 0.508 mm.

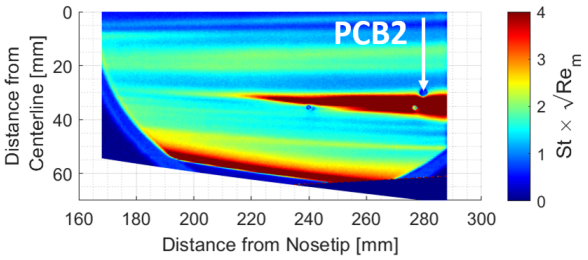

(b) k = + 1.016 mm.

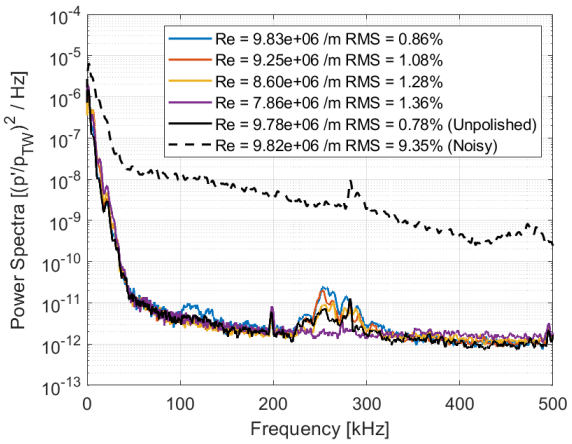

(c) k = + 0.508 mm.

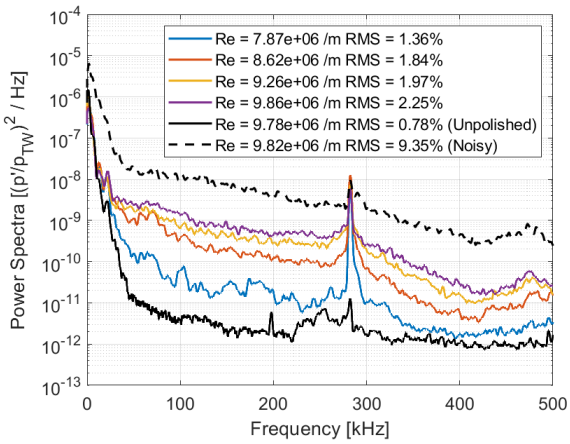

(d) k = + 1.016 mm.

Figure 5.47. PCB2 power spectra near the wedges of heating that form with the backward-facing steps at $\alpha = 4°$.

5.3 Measurements at Yaw Angles

Some experiments were performed at 2° and 4° yaw angles with a 0° angle of attack. The starboard side of the BOLT model was positioned towards the windward direction so that the incoming flow would travel over the denser sensor array. Wedges of heating were only observed with the largest 1.016 mm backward-facing step. The scaled heating contours with the 1.016 mm step at 0°, 2°, and 4° yaw angles are shown in Figure 5.48. The location of the wedge moves further inboard due to the direction of the incoming flow. As the yaw angle increases, the wedge becomes wider and forms at a further upstream location. This indicates that the higher yaw angle results in a larger effect of the step.

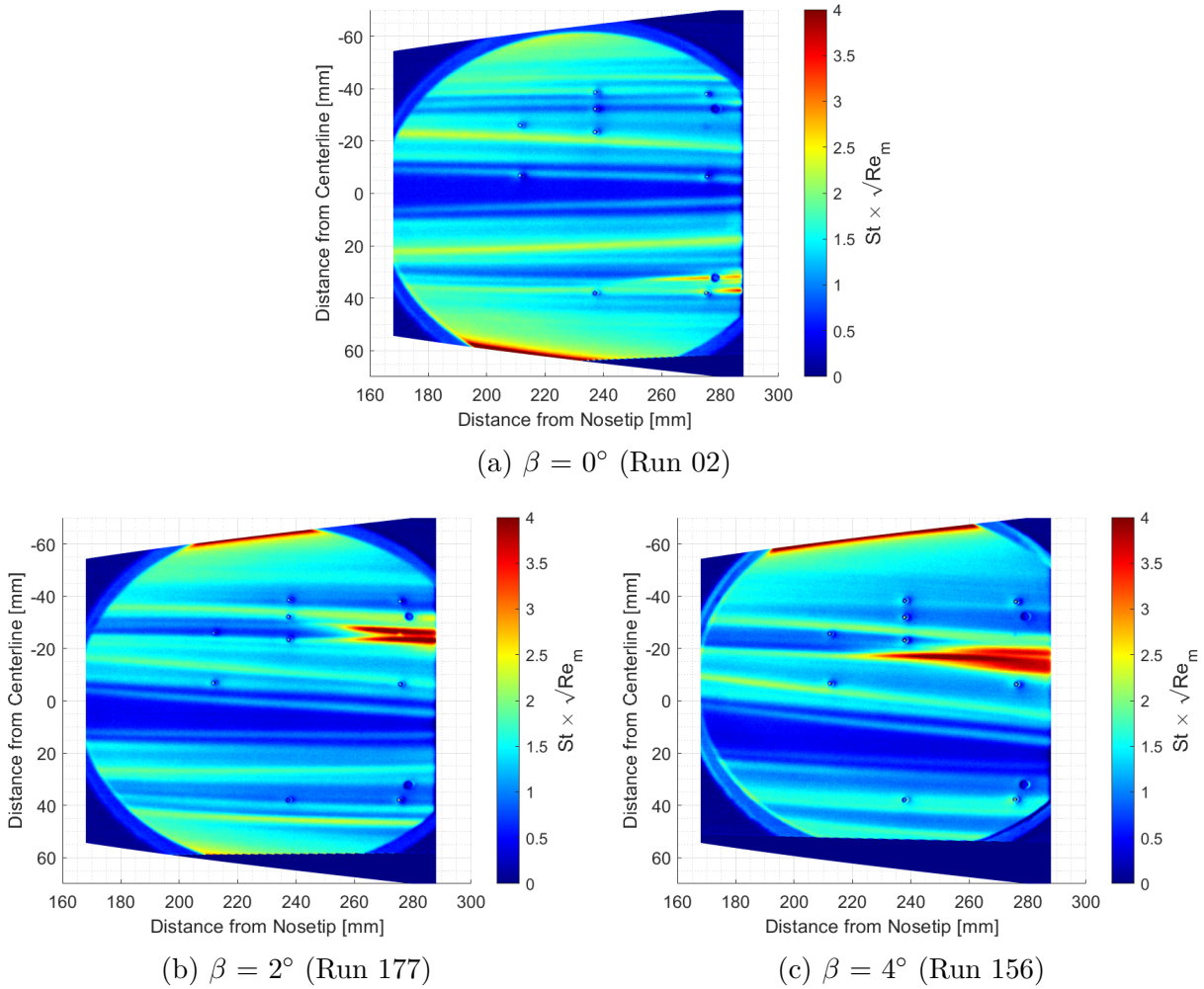

(a) $\beta = 0°$ (Run 02)

(b) $\beta = 2°$ (Run 177)

(c) $\beta = 4°$ (Run 156)

Figure 5.48. Scaled heating contours with the 1.016 mm backward-facing step at different yaw angles. Re = 10.2×10^6 /m.

Spanwise cuts were extracted from the scaled heating contours at x/L = 0.98 and plotted in Figure 5.49 below. The centerline of the profiles are shifted towards the (+Z) direction because of the direction of flow. Peak heating magnitudes of the wedges approach a value of St $\times\sqrt{Re} = 4$. The higher yaw angle does not appear to cause a rise in the peak heating magnitude. The spanwise profiles are shifted by $x \cdot tan(\beta)$ and plotted in Figure 5.50. The centerline and peak near -5 mm are now aligned. The peaks of the heating wedges are also aligned near - 34 mm from the centerline.

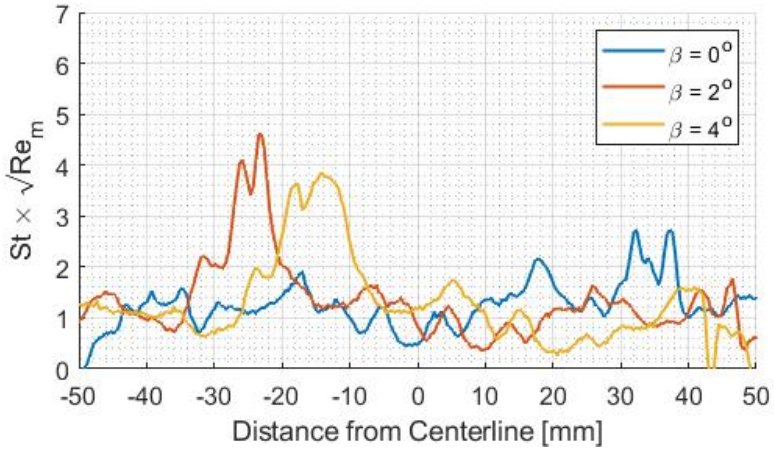

Figure 5.49. Effect of residual yaw angles on the spanwise cuts of heating at x/L = 0.98 (x = 283 mm). Re = 10.2 × 10^6 /m.

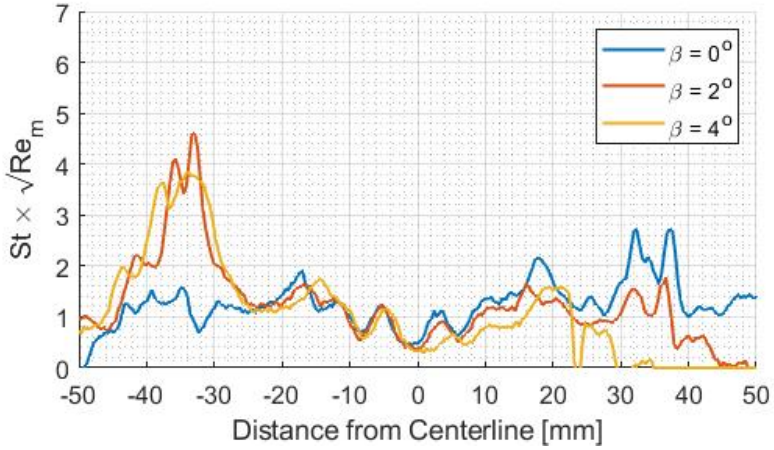

Figure 5.50. Spanwise cuts of heating at x/L = 0.98 (x = 283 mm) from Figure 5.49, shifted by x · tan(β). Re = 10.2 × 10^6 /m.

The Kulites measured some increase in pressure fluctuations, but were not near noisy flow levels. The location of the wedge of heating was not close enough to the Kulites to verify that the flow was turbulent. The power spectra of Kulites nearest to the wedge of heating are shown in Figures 5.51 and 5.52. At a 2° yaw angle, the K2 and K4 sensor measured some increase in pressure fluctuations. At K2, some frequency content was measured above 125 kHz. This was likely due to the Kulite sensor resonance. At K4, two peaks in the power spectra can be seen that are centered around 30 kHz and 70 kHz. The amplitude of the peaks were relatively consistent across the different freestream Reynolds numbers.

At a 4° yaw angle, the wedge of heating moves closest to the K4 and K9 sensors. The K4 sensor measured some frequency content between 125 kHz and 250 kHz that grew with the increasing freestream Reynolds numbers. There appears to be a peak around 180 kHz in the power spectra, shown in Figure 5.51d. It is unclear if this was representative of an instability or if it was caused by the Kulite sensor resonance near 300 kHz. In the K9 power spectra, Figure 5.51e, some frequency content between 0 and 50 kHz is seen. The K2 sensor is located upstream of the wedge and measured some frequency content between 50 kHz and 200 kHz. A clear growth of a peak frequency cannot be identified.

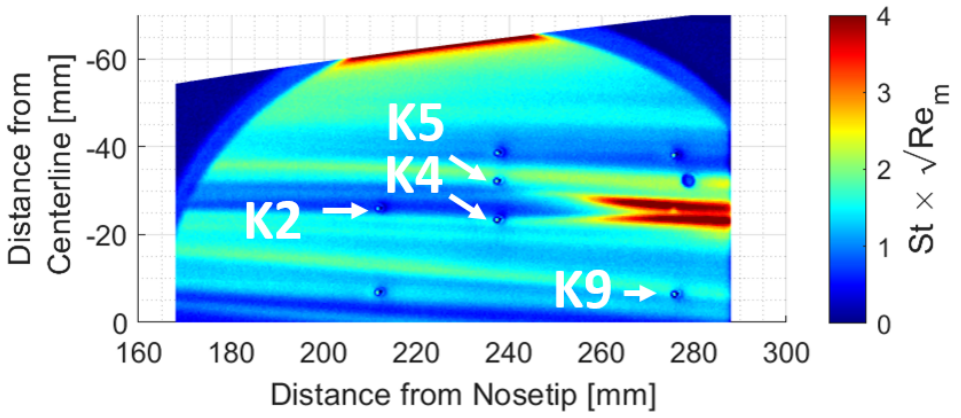

(a) $\beta = 2°$

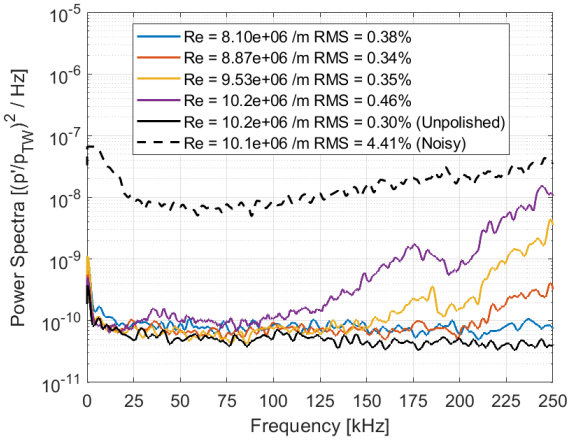

(b) K2 PSD

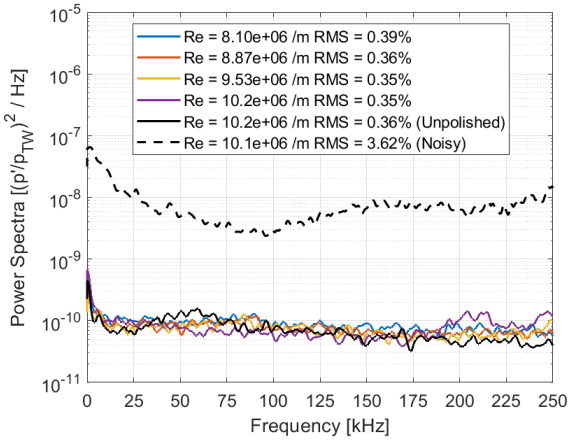

(c) K5 PSD

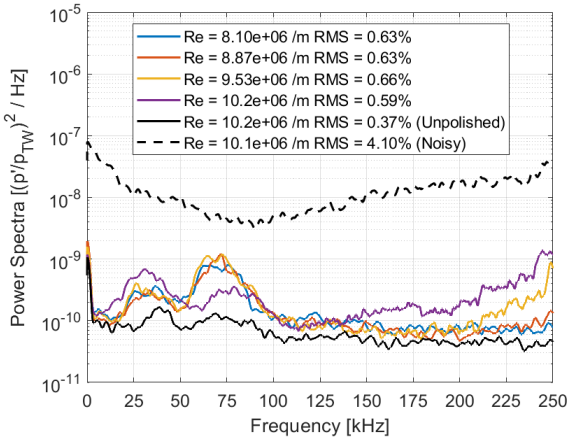

(d) K4 PSD

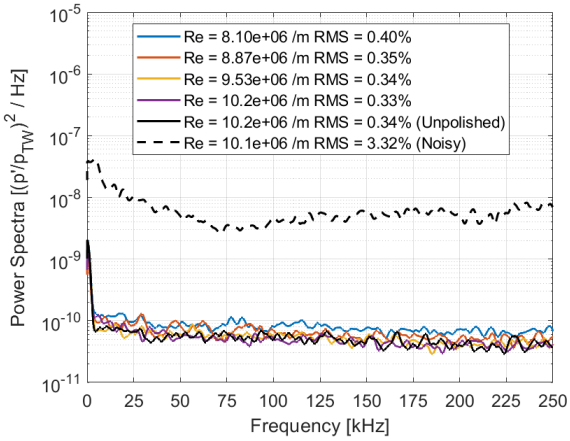

(e) K9 PSD

Figure 5.51. Kulite power spectra near the wedges of heating that form with the 1.016 mm backward-facing step at $\beta = 2°$.

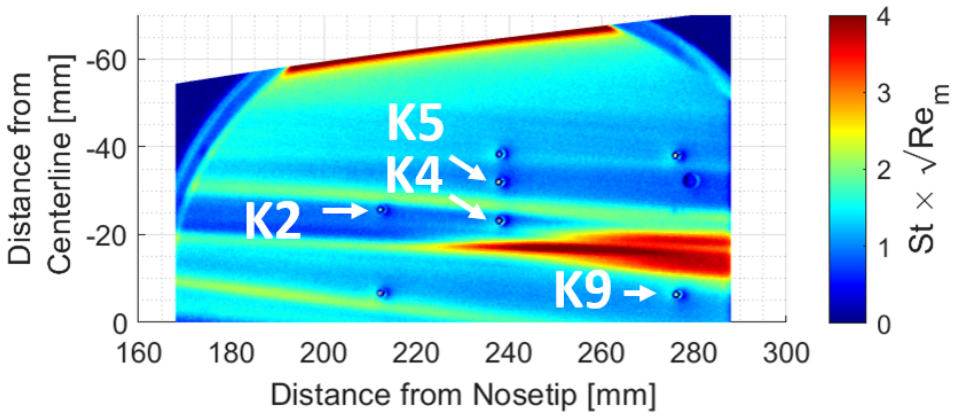

(a) $\beta = 4°$

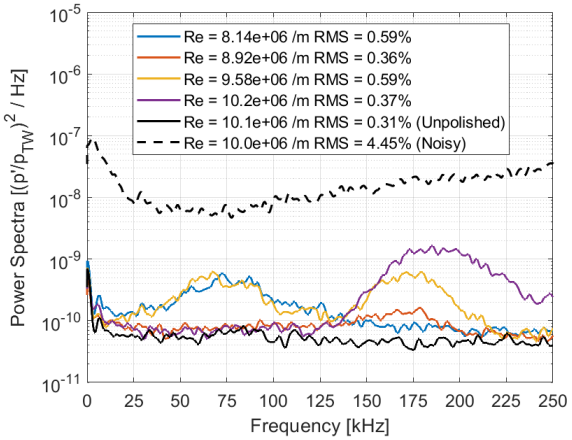

(b) K2 PSD

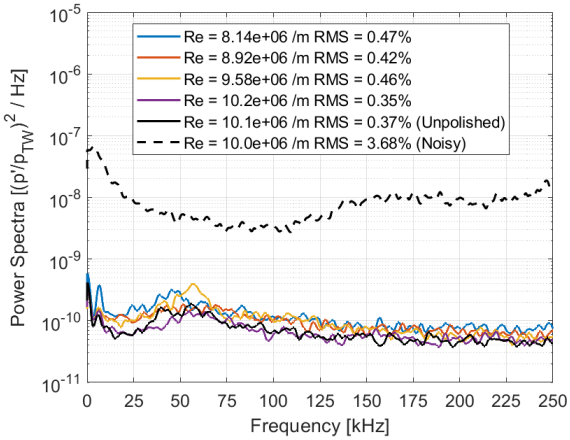

(c) K5 PSD

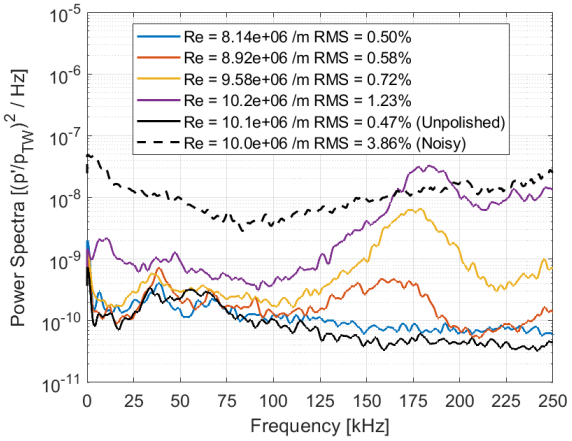

(d) K4 PSD

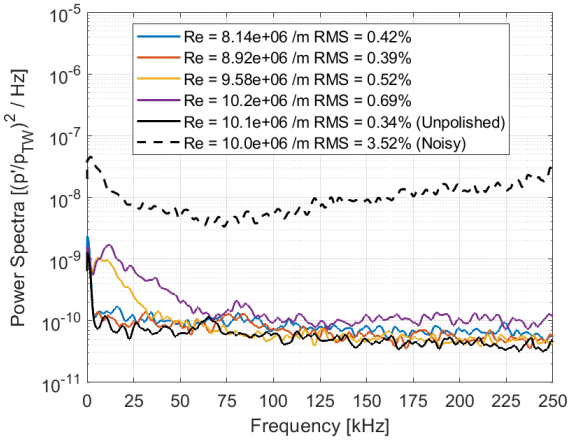

(e) K9 PSD

Figure 5.52. Kulite power spectra near the wedges of heating that form with the 1.016 mm backward-facing step at $\beta = 4°$.

The PCB1 sensor, located on the port side of the experiment surface and closest to the wedge of heating, measured some increase in pressure fluctuations. An instability was not clearly evident in the power spectra, and the broadband amplitudes are between the smooth-wall measurement and noisy flow levels. At a 2° yaw angle, there is some frequency content centered around peak at 200 kHz and 280 kHz. At a 4° yaw angle, there is also some frequency content that is centered around a 280 kHz peak. These peaks may represent an instability, however a clear growth in the amplitude of the peak cannot be identified in the power spectra. The frequency content appears to be less at a 4° yaw angle, likely because the wedge is located further away from the PCB2 sensor face.

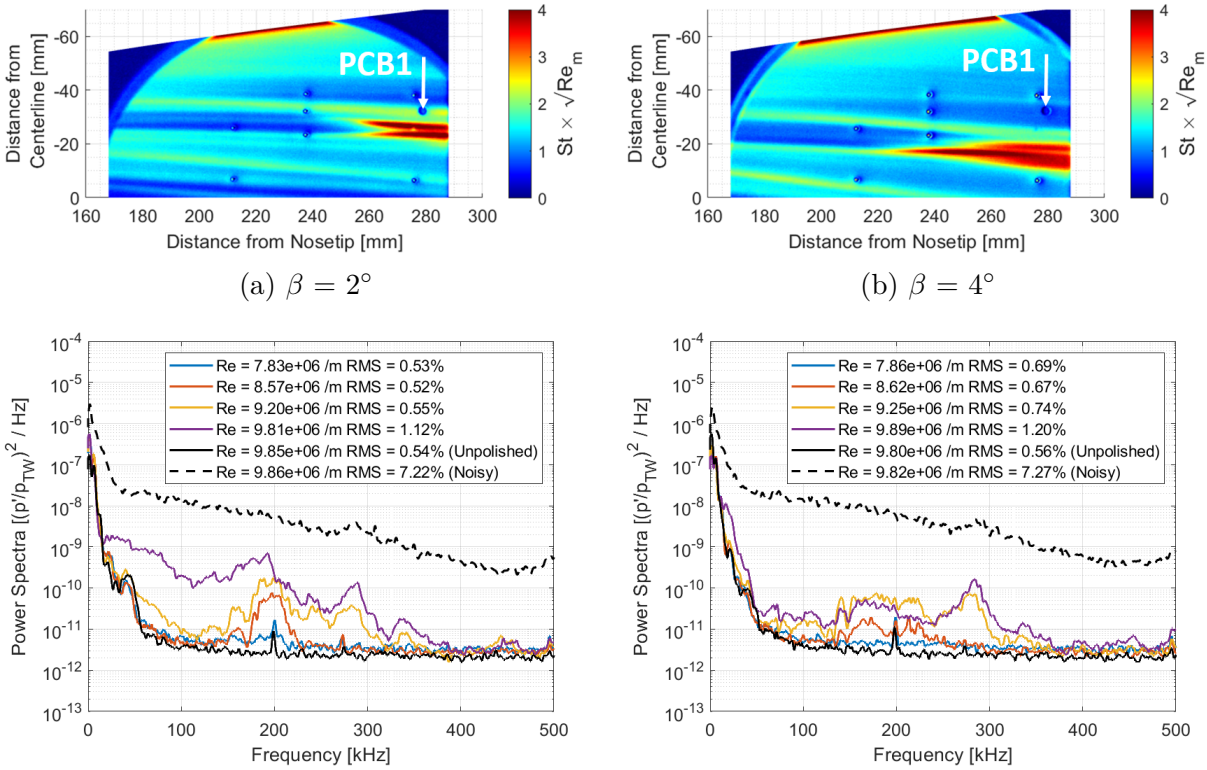

(a) $\beta = 2°$ (b) $\beta = 4°$

(c) $\beta = 2°$ (d) $\beta = 4°$

Figure 5.53. PCB1 power spectra near the wedges of heating that form with the 1.016 mm backward-facing step at $\beta = 2°$ and 4°.

6. SUMMARY AND RECOMMENDATIONS FOR FUTURE WORK

This research was focused on the effect of forward- and backward-facing steps on instability and transition. First, experiments were performed with the sharp 7° half-angle Modular Cone as a preliminary investigation. Then, a comprehensive set of experiments was performed with the 33% scale BOLT model. For each model, different step heights were created just downstream of the nosetip. Forward- and backward-facing steps on the cone ranged from 0.610 mm to 1.219 mm in height. Steps on the BOLT model were sized at the leading-edge joint, where the step was the largest. Forward-facing steps were 0.052 mm, 0.176 mm, and 0.305 mm in height. Backward-facing steps were 0.508 mm and 1.016 mm in height. A polished nosetip was also tested to identify the effect of surface roughness. IR thermography and surface pressure fluctuation measurements were obtained with the steps and compared to measurements with a baseline, smooth-wall geometry. A replica measurement technique was utilized to measure the steps on the BOLT model. Replica measurements were similar to coordinate measurement machine (CMM) probe measurements.

Experiments with the Modular Cone were first performed at a 0.0° angle of attack. With each step, a Reynolds sweep was performed over the course of four runs. Data at freestream Reynolds numbers between 8×10^6 /m and 11×10^6 /m were collected. At a 0.0° angle of attack, forward-facing steps did not cause an increase in the heat transfer, but a 250 kHz instability was identified in the pressure fluctuations. The instability was similar to a second-mode instability and was larger with a larger step size. At a 6° angle of attack, forward-facing steps caused an increase in heat transfer on the windward ray. Larger steps caused a higher increase in heating magnitudes, and a higher freestream Reynolds number also caused an increase in heating magnitudes. Increased pressure fluctuations were also measured along the windward ray, but instabilities were not identified in the spectral content. Backward-facing steps did not cause an increase in heat transfer nor an increase in pressure fluctuations.

Experiments with the modified BOLT model were first performed at a nominal 0° angle of attack and 0° yaw angle. A Reynolds sweep was also performed, with data collected between a freestream Reynolds number of 8×10^6 /m and 10×10^6 /m for each step. Thin wedges

of heating were observed on the port side of the experiment surface with both the 0.508 mm and 1.016 mm backward-facing steps. Heating magnitudes were more intense with the larger 1.016 mm step. Instabilities were identified near these thin wedges of heating. The peak frequencies of the instabilities were between 180 kHz and 250 kHz. The forward-facing steps were also tested but did not have as significant of an effect as the backward-facing steps. Only a small, 180 kHz instability was measured with the largest 0.305 mm forward-facing step. Experiments with the polished, smooth-wall nosetip resulted in similar locations and heating magnitudes of laminar streaks when compared to measurements with the unpolished, smooth-wall nosetip. This indicates that the effect of distributed surface roughness was minimal on the development of the laminar streaks. Higher heating magnitudes and pressure fluctuations were consistently measured on the port side of the model and were thought to be caused by a residual 0.20° yaw angle. However, asymmetries in the nosetips and model may also have a contribution.

The effects of the steps were more intense when the BOLT model was positioned at angles of attack or yaw angles. At 2° and 4° angles of attack, turbulent wedges of heating were observed with the backward-facing steps. The larger 1.016 mm step resulted in a wider and further upstream wedge when compared to the smaller 0.508 mm step. The wedges were also wider and further upstream at a higher angle of attack. Kulite and PCB sensors near the wedges measured increased pressure fluctuations that were representative of a turbulent flow. With the forward-facing steps, only the 0.305 mm step size resulted in a turbulent wedge. A thin wedge of heating was observed with smaller forward-facing steps and the unpolished, smooth-wall nosetip. A significant increase in pressure fluctuations was not measured near these thin wedge of heating. At 2° and 4° yaw angles, turbulent wedges were observed with the largest 1.016 mm backward-facing step. Some increases in pressure fluctuations were measured by nearby Kulite sensors.

6.1 Future Work

These experiments have shown the effects of forward- and backward-facing steps on the Modular Cone and the modified 33% scale BOLT model. Instabilities were modulated by

the steps and a laminar-turbulent transition was observed in the heat transfer. Correlations between the step height and transition locations could potentially be generated from the data but were not within the scope of the current work. Future experiments could be performed to reduce uncertainties and also to provide additional data if correlations were sought. The following are some suggestions for future work to better understand the effect of steps on both models.

1. The effect of the steps could be magnified if the disturbance generated by the step was larger. This could be achieved with experiments at a higher freestream Reynolds number or a larger step size. A higher maximum quiet pressure has historically been achieved in the BAM6QT. Additional data with a broader range of freestream Reynolds numbers or a variety of step sizes would increase the robustness of engineering-based correlations.

2. If additional experiments are performed with the BOLT model, the residual yaw angle could be aligned by seeking the symmetry of the laminar streaks. A sting adapter that allows for fine adjustments would be needed for this. The residual angle of attack should also be reduced. Angle of attack could cause some difference in the heating magnitudes of the laminar streaks. A comparison of the laminar streaks to the DNS computation might be used for this alignment.

3. Additional measurements of the model and the step-height profiles could provide additional insight into the asymmetries that were observed in the present experiments. Precise CMM measurements of the PEEK experiment surface could be used to identify the cause of the asymmetric laminar streak. Replica measurements of the entire joint profile could also be explored. Recent upgrades to the Zygo ZeGage software include a capability to stitch multiple depth maps, which might enable measurements of the step height across the entire azimuth. Measurements on a curved replica still remain a challenge.

4. Off-body measurements near the wedges of heating could be used to identify if a vortical structure exists and is the cause of the increased heating magnitudes. Perturbation

measurements could also be used to provide a better understanding of the instability mechanisms. A micro-pitot probe is currently under development for use in the BAM6QT and could be used for this purpose.

REFERENCES

[1] Schneider, S. P., "Hypersonic laminar-turbulent transition on circular cones and scramjet forebodies", *Progress in Aerospace Sciences*, Vol. 40, Issues 1-2, 2004, pp. 1 - 50. https://doi.org/10.1016/j.paerosci.2003.11.001.

[2] Hamilton II, H. H., Millman, D. R., and Greendyke, R. B., "Finite-difference solution for laminar or turbulent boundary layer flow over axisymmetric bodies with ideal gas, CF4, or equilibrium air chemistry", Technical Paper 3271, NASA, December 1992.

[3] Reed, H. L. and Saric, W. S., "Linear Stability Theory Applied to Boundary Layers", *Annual Reviews of Fluid Mechanics*, Vol. 28, 1996, pp. 389 - 428. https://doi.org/10.1146/annurev.fl.28.010196.002133.

[4] Chynoweth, B. C., *A New Roughness Array for Controlling the Nonlinear Breakdown of Second-Mode Waves at Mach 6*, Master's thesis, Purdue University, August 2015.

[5] Estorf, M., Radespiel, ., Schneider, S. P., Johnson, H., and Hein, S., "Surface-Pressure Measurements of Second-Mode Instability in Quiet Hypersonic Flow," *AIAA Paper 2008-1153*, June 2012. https://doi.org/10.2514/6.2012-1153.

[6] Herbert, T., "Secondary Instability of Boundary Layers", *Annual Reviews of Fluid Mechanics*, Vol. 20, 1988, pp. 487 - 526. https://doi.org/10.1146/annurev.fl.20.010188.002415.

[7] Wheaton, B. M., Bartkowicz, M. D., Subbareddy, P. K., Schneider, S. P., and Candler, G. V., "Roughness-Induced Instabilities at Mach 6: A Combined Numerical and Experimental Study," *AIAA Paper 2011-3248*, June 2011. https://doi.org/10.2514/6.2011-3248.

[8] Schneider, S. P., "Effects of Roughness on Hypersonic Boundary-Layer Transition", *Journal of Spacecraft and Rockets*, Vol. 45, No. 2, 2008, pp. 193 - 209. https://doi.org/10.2514/1.29713.

[9] Wheaton, B. M., Berridge, D. C., Wolf, T. D., Stevens, R. T., and McGrath, B. E., "Boundary Layer Transition (BOLT) Flight Experiment Overview," *AIAA Paper 2018-2892*, June 2018. https://doi.org/10.2514/6.2018-2892.

[10] Wheaton, B. M., Berridge, D. C., Wolf, T. D., Araya, D. B., Stevens, R. T., McGrath, B. E., and Kemp, B. L., "Final Design of the Boundary Layer Transition (BOLT) Flight Experiment," *AIAA Paper 2020-1041*, January 2020. https://doi.org/10.2514/6.2020-1041.

[11] Wheaton, B. M., Butler, C., McKiernan, G., and Berridge, D., "Initial Results from the BOLT Flight Experiment," *AIAA Paper 2022-0345*, January 2022. https://doi.org/10.2514/6.2022-0345.

[12] Berry, S. A., Wheaton, B. M., and Chynoweth, B. C., "Secondary Side Considerations for the BOLT Flight Experiment," *AIAA Paper 2020-1559*, January 2020. https://doi.org/10.2514/6.2020-1559.

[13] Li, F., Choudhari, M., and Paredes, P., "Streak Instability Analysis for BOLT Configuration," *AIAA Paper 2020-3028*, June 2020. https://doi.org/10.2514/6.2020-3028.

[14] Thome, J., Knutson, A., and Candler, G. V.,"Boundary layer instabilities on BoLT subscale geometry," *AIAA Paper 2019-0092*, January 2019. https://doi.org/10.2514/6.2019-0092.

[15] Mullen, D., Moyes, A. J., Kocian, T. S., and Reed, H. L., "Heat Transfer and Boundary-Layer Stability Analysis of Subscale BOLT and the Fin Cone," *AIAA Paper 2019-3081*, June 2019. https://doi.org/10.2514/6.2019-3081.

[16] Kostak, H. E., Bowersox, R. D. W., McKiernan, G. R., Thome, J., Candler, G. V., and King, R. A., "Freestream Disturbance Effects on Boundary Layer Instability and Transition on the AFOSR BOLT Geometry," *AIAA Paper 2019-0088*, January 2019. https://doi.org/10.2514/6.2019-0088.

[17] Kostak, H. E., and Bowersox, R. D. W., "Hypersonic Boundary Layer Off-Body and Surface Measurements on the AFOSR BOLT Geometry," *AIAA Paper 2020-1043*, January 2020. https://doi.org/10.2514/6.2020-1043.

[18] Neel, I. T., Leidy, A. N., Tichenor, N. R., and Bowersox, R. D. W., "Influence of Environmental Disturbances on Hypersonic Crossflow Instability on the HIFiRE-5 Elliptic Cone," *AIAA Paper 2018-1821*, January 2018. https://doi.org/10.2514/6.2018-1821.

[19] Hofferth, J. W. and Saric, W. S., "Boundary-Layer Transition on a Flared Cone in the Texas AM Mach 6 Quiet Tunnel," *AIAA Paper 2012-0923*, January 2012. https://doi.org/10.2514/6.2012-0923.

[20] Berridge, D. C., Kostak, H. E., McKiernan, G. R., King, R. A., Wason, M. P., Wheaton, B. M., Wolf, T. D., and Schneider, S. P., "Hypersonic Ground Tests With High-Frequency Instrumentation In Support of the Boundary Layer Transition (BOLT) Flight Experiment," *AIAA Paper 2019-0090*, January 2019. https://doi.org/10.2514/6.2019-0090.

[21] Berger, K. T., Hollingsworth, K. E., Wright, S. A., and Rufer, S. J., "NASA Langley Aerothermodynamics Laboratory: Hypersonic Testing Capabilities," *AIAA Paper 2015-1337*, January 2015. https://doi.org/10.2514/6.2015-1337.

[22] Berridge, D. C., McKiernan, G. R., Wadhams, T. P., Holden, M. S., Wheaton, B. M., Wolf, T. D., and Schneider, S. P., "Hypersonic Ground Tests In Support of the Boundary Layer Transition (BOLT) Flight Experiment," *AIAA Paper 2018-2893*, June 2018. https://doi.org/10.2514/6.2018-2893.

[23] Chynoweth, B. C., Schneider, S. P., Wheaton, B. M., and Wolf, T. D., "Transition Measurements with Forward and Aft Facing Steps on the BOLT Geometry at Mach 6," *AIAA Paper 2020-1560*, January 2020. https://doi.org/10.2514/6.2020-1560.

[24] Steen, L. E., *Characterization and Development of Nozzles for a Hypersonic Quiet Wind Tunnel*, Master's Thesis, Purdue University, December 2010.

[25] Turbeville, F. D., *Measurements of Transition in the Corner Formed by a Highly-Swept Fin and a Cone at Mach 6*, Ph.D. thesis, Purdue University, December 2021.

[26] Edelman, J. B., *Nonlinear Growth and Breakdown of the Hypersonic Crossflow Instability*, Ph.D. thesis, Purdue University, August 2019.

[27] Wheaton, B. M., *Private Communication*, June 2019.

[28] Anderson, J. D., *Hypersonic and High-Temprature Gas Dynamics*, 2nd ed., American Institute of Aeronautics and Astronautics, 2006.

[29] Cerasuolo, S, *Heat Flux Measurements by Infrared Thermography in the Boeing/AFOSR Mach-6 Quiet Tunnel*, Master's thesis, Universita degli Studi di Napoli Frederico II, January 2017.

[30] Zaccara, M., *Infrared Thermography Data Reduction for Heat Transfer Measurements in the Boeing/AFOSR Mach-6 Quiet Tunnel*, Master's thesis, Universita degli Studi di Napoli Frederico II, January 2018.

[31] Newman, J. A., Willard, S. A., Smith, S. W., and Piascik, R. S., "Replica-based crack inspection," *Engineering Fracture Mechanics*, Vol. 76, No. 1, 2008, pp. 898 - 910. https://doi.org/10.1016/j.engfracmech.2008.12.012.

[32] "Zygo ZeGage Objective Chart," Zygo Corporation, Middlefield, CT, January 2021.

[33] Willems, S., Gulhan, A., Ward, C. A. C., and Schneider, S. P., "Free Transition on a Slender Cone in a Quiet and a Conventional Wind Tunnel and the Effect of Ultrasonically Absorptive Materials," *Progress in Flight Physics*, Vol. 9, 2017, pp. 497 - 516. https://doi.org/10.1051/eucass/201609497.

A. MODULAR CONE ENTRY 4 RUN LOG

Run	P_0 [psia]	T_0 [K]	Re_m	Quiet?	Step Height	Alpha	Note
1	91.9	416.9	7.21 $\times 10^6$	N	$\pm$ 0.000 mm	0	Centering
2	-	-	-	N	$\pm$ 0.000 mm	0	Centering
3	-	-	-	Y	$\pm$ 0.000 mm	0	Centering
4	109.6	414.3	8.69 $\times 10^6$	N	$\pm$ 0.000 mm	0	Centering
5	71.9	415.8	5.67 $\times 10^6$	N	$\pm$ 0.000 mm	0	Centering
6	143.3	416.2	11.3 $\times 10^6$	Y	$\pm$ 0.000 mm	0	Centering
7	143.3	416.6	11.3 $\times 10^6$	Y	- 1.219 mm	0	
8	108.8	416.7	8.55 $\times 10^6$	Y	- 1.219 mm	0	
9	92.8	421.2	7.15 $\times 10^6$	Y	- 1.219 mm	0	
10	124.8	421.1	9.62 $\times 10^6$	Y	- 1.219 mm	0	
11	143.2	420.7	11.1 $\times 10^6$	Y	- 0.813 mm	0	
12	124.6	419.6	9.66 $\times 10^6$	Y	- 0.813 mm	0	
13	108.8	418.3	8.49 $\times 10^6$	Y	- 0.813 mm	0	
14	92.6	418.0	7.23 $\times 10^6$	Y	- 0.813 mm	0	
15	126.0	417.3	9.87 $\times 10^6$	Y	$\pm$ 0.000 mm	0	
16	108.8	417.7	8.50 $\times 10^6$	Y	$\pm$ 0.000 mm	0	
17	92.3	416.8	7.24 $\times 10^6$	Y	$\pm$ 0.000 mm	0	
18	143.3	417.4	11.2 $\times 10^6$	Y	$\pm$ 0.000 mm	0	
19	143.2	416.6	11.2 $\times 10^6$	Y	- 1.016 mm	0	
20	124.8	417.2	9.77 $\times 10^6$	Y	- 1.016 mm	0	
21	109.0	417.1	8.54 $\times 10^6$	Y	- 1.016 mm	0	
22	92.6	416.2	7.29 $\times 10^6$	Y	- 1.016 mm	0	
23	143.9	420.5	11.1 $\times 10^6$	Y	- 0.610 mm	0	
24	124.1	420.1	9.60 $\times 10^6$	Y	- 0.610 mm	0	
25	108.9	419.9	8.44 $\times 10^6$	Y	- 0.610 mm	0	
26	92.7	418.8	7.21 $\times 10^6$	Y	- 0.610 mm	0	
27	142.3	417.7	11.1 $\times 10^6$	Y	- 0.813 mm	0	
28	142.2	417.6	11.1 $\times 10^6$	Y	+ 1.219 mm	0	
29	124.4	418.2	9.71 $\times 10^6$	Y	+ 1.219 mm	0	
30	109.0	417.7	8.52 $\times 10^6$	Y	+ 1.219 mm	0	
31	142.2	417.2	11.1 $\times 10^6$	Y	+ 1.016 mm	0	
32	124.6	417.6	9.74 $\times 10^6$	Y	+ 1.016 mm	0	
33	108.9	416.8	8.54 $\times 10^6$	Y	+ 1.016 mm	0	
34	142.1	421.6	10.9 $\times 10^6$	Y	- 0.813 mm	0	
35	142.1	420.7	11.0 $\times 10^6$	Y	- 1.016 mm	0	
36	142.0	418.9	11.0 $\times 10^6$	Y	- 1.219 mm	6	PCB on WR

**WR denotes Windward Ray*

Run	**P_0 [psia]**	**T_0 [K]**	**Re_m**	**Quiet?**	**Step Height**	**Alpha**	**Note**
37	124.5	418.7	9.69 $\times 10^6$	Y	- 1.219 mm	6	PCB on WR
38	109.1	417.4	8.54 $\times 10^6$	Y	- 1.219 mm	6	PCB on WR
39	73.5	416.7	5.77 $\times 10^6$	Y	- 1.219 mm	6	PCB on WR
40	57.1	416.2	4.49 $\times 10^6$	Y	- 1.219 mm	6	PCB on WR
41	92.2	416.4	7.25 $\times 10^6$	Y	- 1.219 mm	6	PCB on WR
42	80.7	416.5	6.34 $\times 10^6$	Y	- 1.219 mm	6	PCB on WR
43	63.9	414.7	5.06 $\times 10^6$	Y	- 1.219 mm	6	PCB on WR
44	79.8	413.9	6.33 $\times 10^6$	Y	- 1.016 mm	6	PCB on WR
45	92.1	415.2	7.27 $\times 10^6$	Y	- 1.016 mm	6	PCB on WR
46	76.3	414.1	6.06 $\times 10^6$	Y	- 1.016 mm	6	PCB on WR
47	141.7	415.4	11.2 $\times 10^6$	Y	+ 1.219 mm	6	PCB on WR
48	141.7	421.2	10.9 $\times 10^6$	Y	+ 0.813 mm	6	PCB on WR
49	79.8	419.6	6.19 $\times 10^6$	Y	- 0.813 mm	6	PCB on WR
50	92.1	418.8	7.17 $\times 10^6$	Y	- 0.813 mm	6	PCB on WR
51	100.3	418.9	7.81 $\times 10^6$	Y	- 0.813 mm	6	PCB on WR
52	108.9	418.5	8.48 $\times 10^6$	Y	- 0.813 mm	6	PCB on WR
53	108.8	416.5	8.55 $\times 10^6$	Y	- 0.610 mm	6	PCB on WR
55	116.5	416.9	9.14 $\times 10^6$	Y	- 0.610 mm	6	PCB on WR
56	125.4	417.0	9.83 $\times 10^6$	Y	- 0.610 mm	6	PCB on WR
57	66.6	414.4	5.28 $\times 10^6$	Y	- 1.016 mm	6	PCB on WR
58	73.1	415.0	5.78 $\times 10^6$	Y	- 1.016 mm	6	PCB on WR
59	56.8	413.9	4.51 $\times 10^6$	Y	± 0.000 mm	6	PCB on WR
60	125.6	416.0	9.88 $\times 10^6$	Y	± 0.000 mm	6	PCB on WR
61	62.8	419.6	4.87 $\times 10^6$	Y	± 0.000 mm	6	PCB on WR
62	73.1	419.2	5.68 $\times 10^6$	Y	± 0.000 mm	6	PCB on WR
63	92.3	419.5	7.16 $\times 10^6$	Y	± 0.000 mm	6	PCB on WR
64	79.7	419.0	6.20 $\times 10^6$	Y	± 0.000 mm	6	PCB on WR
65	100.2	418.1	7.82 $\times 10^6$	Y	± 0.000 mm	6	PCB on WR
66	108.8	418.1	8.50 $\times 10^6$	Y	± 0.000 mm	6	PCB on WR
67	117.3	417.9	9.17 $\times 10^6$	Y	± 0.000 mm	6	PCB on WR
68	79.6	420.4	6.15 $\times 10^6$	N	± 0.000 mm	6	PCB on WR
69	146.6	423.0	11.2 $\times 10^6$	N	± 0.000 mm	6	PCB on WR
70	79.6	420.0	6.17 $\times 10^6$	N	- 1.219 mm	6	PCB on WR
71	146.7	422.4	11.3 $\times 10^6$	N	- 1.219 mm	6	PCB on WR
72	79.6	419.4	6.18 $\times 10^6$	N	+ 1.219 mm	6	PCB on WR
73	146.8	422.4	11.3 $\times 10^6$	N	+ 1.219 mm	6	PCB on WR
74	66.9	412.8	5.34 $\times 10^6$	Y	- 1.016 mm	6	IR on WR
75	73.5	419.5	5.70 $\times 10^6$	Y	- 1.016 mm	6	IR on WR
76	79.7	419.8	6.18 $\times 10^6$	Y	- 1.016 mm	6	IR on WR
77	92.4	419.1	7.18 $\times 10^6$	Y	- 1.016 mm	6	IR on WR
78	56.9	416.6	4.47 $\times 10^6$	Y	- 1.219 mm	6	IR on WR

Run	**P_0 [psia]**	**T_0 [K]**	**Re_m**	**Quiet?**	**Step Height**	**Alpha**	**Note**
79	63.8	416.1	5.02 $\times 10^6$	Y	- 1.219 mm	6	IR on WR
80	73.3	416.7	5.75 $\times 10^6$	Y	- 1.219 mm	6	IR on WR
81	79.9	417.0	6.27 $\times 10^6$	Y	- 1.219 mm	6	IR on WR
82	92.1	416.7	7.23 $\times 10^6$	Y	- 1.219 mm	6	IR on WR
83	80.0	415.7	6.31 $\times 10^6$	Y	- 0.813 mm	6	IR on WR
84	92.4	416.2	7.27 $\times 10^6$	Y	- 0.813 mm	6	IR on WR
85	100.2	416.6	7.87 $\times 10^6$	Y	- 0.813 mm	6	IR on WR
86	108.7	416.4	8.54 $\times 10^6$	Y	- 0.813 mm	6	IR on WR
87	108.8	415.9	8.57 $\times 10^6$	Y	- 0.610 mm	6	IR on WR
88	116.5	416.2	9.16 $\times 10^6$	Y	- 0.610 mm	6	IR on WR
89	125.4	416.7	9.84 $\times 10^6$	Y	- 0.610 mm	6	IR on WR
90	57.0	419.2	4.43 $\times 10^6$	Y	$\pm$ 0.000 mm	6	IR on WR
91	79.8	419.0	6.20 $\times 10^6$	Y	$\pm$ 0.000 mm	6	IR on WR
92	92.5	419.7	7.18 $\times 10^6$	Y	$\pm$ 0.000 mm	6	IR on WR
93	108.9	419.3	8.46 $\times 10^6$	Y	$\pm$ 0.000 mm	6	IR on WR
94	125.3	418.7	9.76 $\times 10^6$	Y	$\pm$ 0.000 mm	6	IR on WR

B. BOLT ENTRY 3 RUN LOG

Run	P_0 [psia]	T_0 [K]	Re_m	Quiet?	Step Height	Alpha	Beta
1	126.4	411.2	10.1×10^6	Y	± 0.000 mm	0	0
2	128.9	416.0	10.1×10^6	Y	+ 1.016 mm	0	0
3	121.4	415.6	9.57×10^6	Y	+ 1.016 mm	0	0
4	112.9	415.5	8.90×10^6	Y	+ 1.016 mm	0	0
5	103.0	415.1	8.14×10^6	Y	+ 1.016 mm	0	0
6	128.8	414.8	10.2×10^6	Y	- 0.305 mm	0	0
7	121.3	415.4	9.57×10^6	Y	- 0.305 mm	0	0
8	113.0	415.7	8.90×10^6	Y	- 0.305 mm	0	0
9	103.1	415.4	8.14×10^6	Y	- 0.305 mm	0	0
10	129.0	414.4	10.2×10^6	Y	± 0.000 mm	0	0
11	121.4	416.5	9.54×10^6	Y	± 0.000 mm	0	0
12	112.8	416.8	8.85×10^6	Y	± 0.000 mm	0	0
13	103.0	416.8	8.09×10^6	Y	± 0.000 mm	0	0
14	129.0	415.6	10.2×10^6	Y	(Polish) ± 0.000 mm	0	0
15	121.0	415.5	9.54×10^6	Y	(Polish) ± 0.000 mm	0	0
16	113.0	415.6	8.91×10^6	Y	(Polish) ± 0.000 mm	0	0
17	102.9	414.6	8.15×10^6	Y	(Polish) ± 0.000 mm	0	0
18	129.0	414.9	10.2×10^6	Y	+ 0.508 mm	0	0
19	121.3	415.2	9.58×10^6	Y	+ 0.508 mm	0	0
20	113.0	415.5	8.91×10^6	Y	+ 0.508 mm	0	0
21	103.0	415.5	8.13×10^6	Y	+ 0.508 mm	0	0
22	130.4	419.6	10.1×10^6	N	(Polish) ± 0.000 mm	0	0
23	129.0	416.4	10.1×10^6	Y	- 0.076 mm	0	0
24	121.3	416.7	9.52×10^6	Y	- 0.076 mm	0	0
25	113.0	416.9	8.86×10^6	Y	- 0.076 mm	0	0
26	103.1	415.8	8.12×10^6	Y	- 0.076 mm	0	0
27	128.9	415.4	10.2×10^6	Y	- 0.152 mm	0	0
28	121.4	415.7	9.57×10^6	Y	- 0.152 mm	0	0
29	112.9	415.5	8.90×10^6	Y	- 0.152 mm	0	0
30	103.1	415.3	8.14×10^6	Y	- 0.152 mm	0	0
31	128.9	413.7	10.2×10^6	Y	+ 1.016 mm	4	0
32	121.4	415.0	9.59×10^6	Y	+ 1.016 mm	4	0
33	112.7	415.0	8.91×10^6	Y	+ 1.016 mm	4	0
34	103.0	414.8	8.15×10^6	Y	+ 1.016 mm	4	0
35	129.0	416.8	10.1×10^6	Y	- 0.305 mm	4	0
36	120.9	416.4	9.50×10^6	Y	- 0.305 mm	4	0
37	112.8	416.1	8.88×10^6	Y	- 0.305 mm	4	0
38	103.0	416.1	8.11×10^6	Y	- 0.305 mm	4	0
39	129.1	414.2	10.2×10^6	Y	± 0.000 mm	4	0

Run	P_0 [psia]	T_0 [K]	Re_m	Quiet?	Step Height	Alpha	Beta
40	121.3	414.9	9.60×10^6	Y	± 0.000 mm	4	0
41	112.7	414.9	8.91×10^6	Y	± 0.000 mm	4	0
42	103.1	415.2	8.14×10^6	Y	± 0.000 mm	4	0
43	129.0	414.5	10.2×10^6	Y	± 0.000 mm	4	0
44	121.4	415.1	9.59×10^6	Y	± 0.000 mm	4	0
45	112.8	415.1	8.92×10^6	Y	± 0.000 mm	4	0
46	107.1	419.7	8.31×10^6	N	± 0.000 mm	4	0
47	103.1	414.7	8.16×10^6	Y	± 0.000 mm	4	0
48	128.9	416.0	10.1×10^6	Y	(Polish) ± 0.000 mm	4	0
49	121.3	416.7	9.52×10^6	Y	(Polish) ± 0.000 mm	4	0
50	112.8	416.6	8.86×10^6	Y	(Polish) ± 0.000 mm	4	0
51	103.0	416.2	8.10×10^6	Y	(Polish) ± 0.000 mm	4	0
52	130.3	420.7	10.1×10^6	N	(Polish) ± 0.000 mm	4	0
53	128.9	415.5	10.2×10^6	Y	+ 0.508 mm	4	0
54	121.3	415.8	9.56×10^6	Y	+ 0.508 mm	4	0
55	112.9	415.0	8.92×10^6	Y	+ 0.508 mm	4	0
56	103.1	415.1	8.14×10^6	Y	+ 0.508 mm	4	0
57	129.0	414.9	10.2×10^6	Y	- 0.152 mm	4	0
58	121.4	415.4	9.58×10^6	Y	- 0.152 mm	4	0
59	112.8	415.3	8.90×10^6	Y	- 0.152 mm	4	0
60	103.1	415.4	8.13×10^6	Y	- 0.152 mm	4	0
61	129.0	414.9	10.2×10^6	Y	- 0.076 mm	4	0
62	121.5	415.2	9.59×10^6	Y	- 0.076 mm	4	0
63	112.8	415.0	8.91×10^6	Y	- 0.076 mm	4	0
64	103.0	415.0	8.14×10^6	Y	- 0.076 mm	4	0
65	120.7	405.1	9.94×10^6	Y	+ 1.016 mm	4	0
66	113.3	406.5	9.27×10^6	Y	+ 1.016 mm	4	0
67	105.6	406.9	8.63×10^6	Y	+ 1.016 mm	4	0
68	96.4	407.1	7.88×10^6	Y	+ 1.016 mm	4	0
69	88.1	406.6	7.21×10^6	Y	+ 1.016 mm	4	0
70	88.1	406.3	7.22×10^6	Y	+ 1.016 mm	4	0
71	120.7	407.1	9.86×10^6	Y	- 0.305 mm	4	0
72	113.6	407.4	9.26×10^6	Y	- 0.305 mm	4	0
73	105.7	407.3	8.62×10^6	Y	- 0.305 mm	4	0
74	96.4	407.3	7.87×10^6	Y	- 0.305 mm	4	0
75	88.1	406.8	7.20×10^6	Y	- 0.305 mm	4	0
76	75.5	408.4	6.13×10^6	Y	- 0.305 mm	4	0
77	75.6	408.2	6.14×10^6	Y	+ 1.016 mm	4	0
78	120.8	409.1	9.78×10^6	Y	± 0.000 mm	4	0
79	113.7	409.5	9.19×10^6	Y	± 0.000 mm	4	0
80	105.7	409.0	8.56×10^6	Y	± 0.000 mm	4	0
81	96.5	408.5	7.83×10^6	Y	± 0.000 mm	4	0

Run	P_0 [psia]	T_0 [K]	Re_m	Quiet?	Step Height	Alpha	Beta
82	88.2	408.2	7.17×10^6	Y	± 0.000 mm	4	0
83	75.5	407.6	6.15×10^6	Y	± 0.000 mm	4	0
84	120.7	408.4	9.80×10^6	Y	(Polish) ± 0.000 mm	4	0
85	113.6	408.2	9.24×10^6	Y	(Polish) ± 0.000 mm	4	0
86	105.7	407.8	8.60×10^6	Y	(Polish) ± 0.000 mm	4	0
87	96.5	407.6	7.86×10^6	Y	(Polish) ± 0.000 mm	4	0
88	88.2	407.4	7.19×10^6	Y	(Polish) ± 0.000 mm	4	0
89	75.5	408.8	6.12×10^6	Y	(Polish) ± 0.000 mm	4	0
90	69.6	404.9	5.73×10^6	Y	(Polish) ± 0.000 mm	4	0
91	125.0	416.5	9.82×10^6	N	(Polish) ± 0.000 mm	4	0
92	120.8	408.8	9.79×10^6	Y	+ 0.508 mm	4	0
93	113.7	408.4	9.23×10^6	Y	+ 0.508 mm	4	0
94	105.7	408.4	8.58×10^6	Y	+ 0.508 mm	4	0
95	96.5	407.7	7.86×10^6	Y	+ 0.508 mm	4	0
96	88.1	408.1	7.16×10^6	Y	+ 0.508 mm	4	0
97	75.5	407.2	6.16×10^6	Y	+ 0.508 mm	4	0
98	120.7	407.7	9.83×10^6	Y	- 0.152 mm	4	0
99	113.7	408.0	9.25×10^6	Y	- 0.152 mm	4	0
100	105.7	408.0	8.60×10^6	Y	- 0.152 mm	4	0
101	96.6	407.8	7.86×10^6	Y	- 0.152 mm	4	0
102	88.1	407.3	7.19×10^6	Y	- 0.152 mm	4	0
103	75.4	406.7	6.17×10^6	Y	- 0.152 mm	4	0
104	120.8	409.4	9.77×10^6	Y	- 0.076 mm	4	0
105	113.7	410.2	9.17×10^6	Y	- 0.076 mm	4	0
106	105.7	410.0	8.53×10^6	Y	- 0.076 mm	4	0
107	96.5	409.8	7.79×10^6	Y	- 0.076 mm	4	0
108	88.2	408.8	7.15×10^6	Y	- 0.076 mm	4	0
109	75.5	408.2	6.13×10^6	Y	- 0.076 mm	4	0
110	129.1	416.0	10.2×10^6	Y	+ 0.508 mm	2	0
111	121.5	416.3	9.55×10^6	Y	+ 0.508 mm	2	0
112	112.9	416.4	8.87×10^6	Y	+ 0.508 mm	2	0
113	103.2	415.9	8.12×10^6	Y	+ 0.508 mm	2	0
114	94.1	415.5	7.43×10^6	Y	+ 0.508 mm	2	0
115	80.6	414.6	6.38×10^6	Y	+ 0.508 mm	2	0
116	64.5	413.9	5.12×10^6	Y	+ 0.508 mm	2	0
117	129.1	414.9	10.2×10^6	Y	- 0.305 mm	2	0
118	121.4	418.0	9.48×10^6	Y	- 0.305 mm	2	0
119	113.0	418.1	8.82×10^6	Y	- 0.305 mm	2	0
120	103.1	417.8	8.06×10^6	Y	- 0.305 mm	2	0
121	94.2	417.1	7.39×10^6	Y	- 0.305 mm	2	0
122	129.1	416.4	10.1×10^6	Y	± 0.000 mm	2	0
123	121.4	416.5	9.54×10^6	Y	± 0.000 mm	2	0

Run	P_0 [psia]	T_0 [K]	Re_m	Quiet?	Step Height	Alpha	Beta
124	112.8	416.1	8.88×10^6	Y	± 0.000 mm	2	0
127	103.2	414.2	8.18×10^6	Y	± 0.000 mm	2	0
128	94.2	415.0	7.44×10^6	Y	± 0.000 mm	2	0
129	80.6	414.6	6.38×10^6	Y	± 0.000 mm	2	0
130	74.4	414.0	5.90×10^6	Y	± 0.000 mm	2	0
131	64.5	413.5	5.13×10^6	Y	± 0.000 mm	2	0
132	130.4	421.2	10.1×10^6	N	± 0.000 mm	2	0
133	129.2	416.3	10.2×10^6	Y	(Polish) ± 0.000 mm	2	0
134	121.5	416.7	9.53×10^6	Y	(Polish) ± 0.000 mm	2	0
135	113.0	416.6	8.87×10^6	Y	(Polish) ± 0.000 mm	2	0
136	103.1	416.4	8.10×10^6	Y	(Polish) ± 0.000 mm	2	0
137	94.1	415.8	7.42×10^6	Y	(Polish) ± 0.000 mm	2	0
138	129.1	415.8	10.2×10^6	Y	(Polish) ± 0.000 mm	2	0
139	130.5	421.5	10.0×10^6	N	(Polish) ± 0.000 mm	2	0
140	129.0	416.5	10.1×10^6	Y	+ 1.016 mm	2	0
141	121.4	415.9	9.56×10^6	Y	+ 1.016 mm	2	0
142	112.9	415.6	8.90×10^6	Y	+ 1.016 mm	2	0
143	103.1	415.0	8.15×10^6	Y	+ 1.016 mm	2	0
144	94.1	414.8	7.45×10^6	Y	+ 1.016 mm	2	0
145	129.1	415.0	10.2×10^6	Y	+ 0.508 mm	2	0
146	129.1	416.3	10.1×10^6	Y	- 0.152 mm	2	0
147	121.4	416.8	9.53×10^6	Y	- 0.152 mm	2	0
148	112.8	416.7	8.85×10^6	Y	- 0.152 mm	2	0
149	103.1	416.4	8.10×10^6	Y	- 0.152 mm	2	0
150	129.0	415.9	10.2×10^6	Y	- 0.076 mm	2	0
151	121.4	416.3	9.55×10^6	Y	- 0.076 mm	2	0
152	112.6	416.0	8.87×10^6	Y	- 0.076 mm	2	0
153	103.0	415.3	8.13×10^6	Y	- 0.076 mm	2	0
154	129.1	415.1	10.2×10^6	Y	+ 0.508 mm	2	0
155	80.6	414.6	6.38×10^6	Y	+ 0.508 mm	2	0
156	129.0	414.3	10.2×10^6	Y	+ 1.016 mm	0	4
157	112.8	414.7	8.92×10^6	Y	+ 1.016 mm	0	4
158	121.3	415.3	9.58×10^6	Y	+ 1.016 mm	0	4
159	103.0	415.2	8.14×10^6	Y	+ 1.016 mm	0	4
160	129.0	416.8	10.1×10^6	Y	- 0.305 mm	0	4
161	112.9	416.8	8.85×10^6	Y	- 0.305 mm	0	4
162	121.4	417.0	9.52×10^6	Y	- 0.305 mm	0	4
163	129.1	416.5	10.1×10^6	Y	± 0.000 mm	0	4
164	112.8	416.3	8.87×10^6	Y	± 0.000 mm	0	4
165	121.4	416.5	9.54×10^6	Y	± 0.000 mm	0	4

Run	P_0 [psia]	T_0 [K]	Re_m	Quiet?	Step Height	Alpha	Beta
166	103.1	416.2	8.11×10^6	Y	± 0.000 mm	0	4
167	129.1	415.5	10.2×10^6	Y	(Polish) ± 0.000 mm	0	4
168	112.8	415.7	8.89×10^6	Y	(Polish) ± 0.000 mm	0	4
169	121.4	415.8	9.57×10^6	Y	(Polish) ± 0.000 mm	0	4
170	130.4	421.4	10.0×10^6	N	(Polish) ± 0.000 mm	0	4
171	129.1	415.6	10.2×10^6	Y	+ 0.508 mm	0	4
172	112.8	415.5	8.90×10^6	Y	+ 0.508 mm	0	4
173	121.4	415.3	9.58×10^6	Y	+ 0.508 mm	0	4
174	129.0	415.2	10.2×10^6	Y	- 0.152 mm	0	4
175	112.9	415.5	8.91×10^6	Y	- 0.152 mm	0	4
176	121.5	415.7	9.58×10^6	Y	- 0.152 mm	0	4
177	129.0	416.1	10.2×10^6	Y	+ 1.016 mm	0	2
178	112.8	416.4	8.87×10^6	Y	+ 1.016 mm	0	2
179	121.4	416.9	9.53×10^6	Y	+ 1.016 mm	0	2
180	103.1	416.5	8.10×10^6	Y	+ 1.016 mm	0	2
181	129.1	415.8	10.2×10^6	Y	- 0.305 mm	0	2
182	114.9	415.8	9.06×10^6	Y	- 0.305 mm	0	2
183	121.4	415.0	9.60×10^6	Y	- 0.305 mm	0	2
184	129.1	415.2	10.2×10^6	Y	± 0.000 mm	0	2
185	113.0	415.3	8.92×10^6	Y	± 0.000 mm	0	2
186	121.4	415.3	9.58×10^6	Y	± 0.000 mm	0	2
187	103.1	415.0	8.15×10^6	Y	± 0.000 mm	0	2
188	130.5	420.6	10.1×10^6	N	± 0.000 mm	0	2
189	129.1	414.7	10.2×10^6	Y	(Polish) ± 0.000 mm	0	2
190	113.0	414.9	8.93×10^6	Y	(Polish) ± 0.000 mm	0	2
191	121.4	415.0	9.59×10^6	Y	(Polish) ± 0.000 mm	0	2
192	129.0	416.6	10.1×10^6	Y	+ 0.508 mm	0	2
193	113.1	413.6	8.99×10^6	Y	+ 0.508 mm	0	2
194	121.4	415.2	9.59×10^6	Y	+ 0.508 mm	0	2
195	129.0	416.5	10.1×10^6	Y	- 0.076 mm	0	2
196	113.0	415.8	8.90×10^6	Y	- 0.076 mm	0	2
197	121.4	415.3	9.58×10^6	Y	- 0.076 mm	0	2

C. 33% SCALE BOLT MODEL DRAWINGS

LEV.	ALTERATION	BY	DATE
-	INITIAL RELEASE	-	-

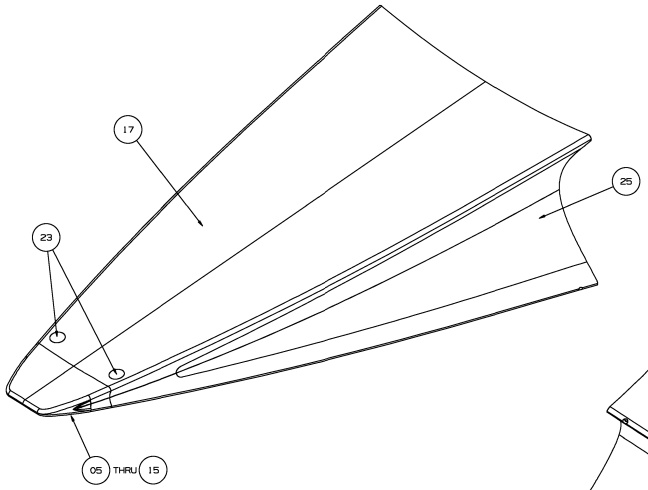

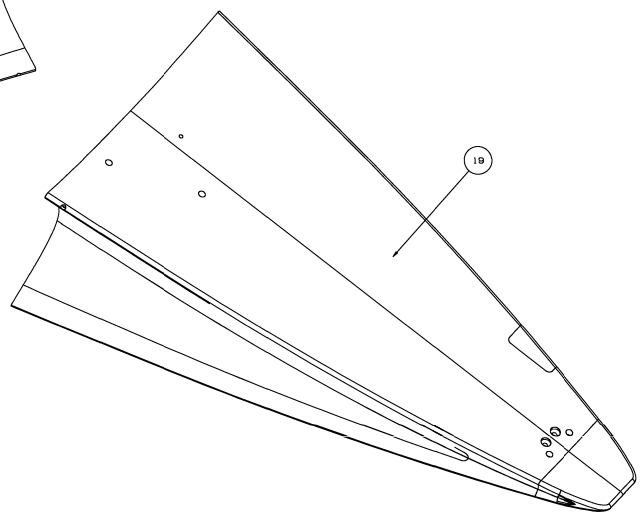

FASTENER SEATING TORQUE VALUES		
#4-40 FHCS	8 IN-LBF	-
#4-40 SHCS	18 IN-LBF	-
#6-32 SHCS	34 IN-LBF	-
#8-32 LHCS	25 IN-LBF	-

ITEM NO.	FASTENER DESCRIPTION	QTY
108	#8-32 LHCS X 3/8" L	4
105	#8-32 LHCS X 5/16" L	12
104	#6-32 SHCS X 3/8" L	4
103	#4-40 FHCS X 5/16" L	2
102	#4-40 SHCS X 5/16" L	2
101	#4-40 SHCS X 3/16" L	2

ITEM NO.	PIN DESCRIPTION	QTY
203	1/8 PULL PIN X 3/8" L	2
202	1/8 PULL PIN X 5/16" L	2
201	1/8 PULL PIN X 1/4" L	4

SYMBOL	DESCRIPTION
○	PART
⬡	FASTENER
□	PIN

OJ MODEL ASSEMBLY

NOT TO SCALE

DASH NO	DESCRIPTION	MATERIAL	QTY
25	GUTTER PANELS	FGX73-P-115	2
23	CUSTOM INSERT	1932500 1-1002-09	2
21	MODS TO BASE	1932500 1-1002-07	1
19	MODS TO LOWER BODY	1932500 1-1002-05	1
17	MODS TO UPPER BODY	1932500 1-1002-03	1
15	NOSE TIP 6	1932500 1-1001-15	1
13	NOSE TIP 5	1932500 1-1001-13	1
11	NOSE TIP 4	1932500 1-1001-11	1
09	NOSE TIP 3	1932500 1-1001-09	1
07	NOSE TIP 2	1932500 1-1001-07	1
05	NOSE TIP 1	1932500 1-1001-05	1
03	STRONGBACK	1932500 1-1001-03	1
01	MODEL ASSEMBLY		1

NOTES

1. NEXT ASSY DWG: 19325001-1000
2. ALL MATL AND HARDWARE TO BE CERTIFIED
3. ALL FASTENERS AND PINS TO BE CERTIFIED UNLESS SPECIFIED
4. ETCH PART NUMBER ON DETAILS
5. ANY DEVIATIONS TO THIS DRAWING MUST HAVE PRIOR ENGINEERING APPROVAL AND BE RECORDED.

DRAWN BY	E. SMALLWOOD	3/6/20
DESIGN ENG	E. SMALLWOOD	3/6/20
APPROVED	G. SHARMA	3/6/20
STRESS		
PROJECT	BOLT MODEL REWORK	
FILE NAME	-	
JOB NO.	19325-001	
DO NOT SCALE DRAWING	SIZE E	

TRI-MODELS, INC.
5191 OCEANUS DR
HUNTINGTON BEACH, CA 92649

FSCM NO. 61522
SCALE 1:1

TRI MODELS, INC.
PURDUE UNIVERSITY
BOLT MODEL REWORK
ASSEMBLY

DRAWING NO. 1932500 1-1000 REV -
SHEET 1 OF 3

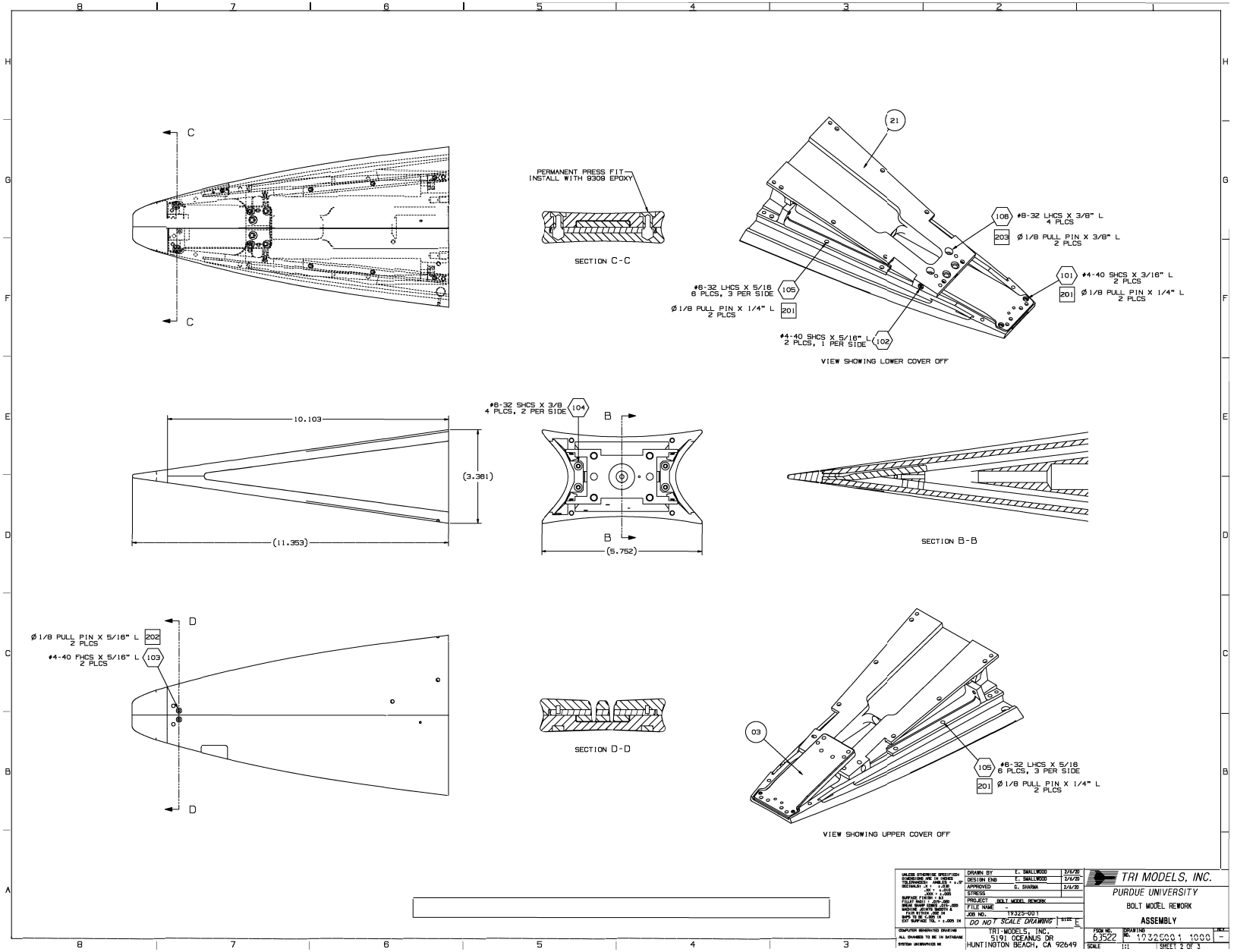
C
C
PERMANENT PRESS FIT
INSTALL WITH 9309 EPOXY
SECTION C-C
21
108 #8-32 LHCS X 3/8" L
4 PLCS
203 Ø1/8 PULL PIN X 3/8" L
2 PLCS
101 #4-40 SHCS X 3/16" L
2 PLCS
201 Ø1/8 PULL PIN X 1/4" L
2 PLCS
#8-32 LHCS X 5/16
6 PLCS, 3 PER SIDE 105
Ø1/8 PULL PIN X 1/4" L 201
2 PLCS
#4-40 SHCS X 5/16" L 102
2 PLCS, 1 PER SIDE
VIEW SHOWING LOWER COVER OFF
10.103
(3.381)
(11.353)
#8-32 SHCS X 3/8 104
4 PLCS, 2 PER SIDE
B
B
(5.752)
SECTION B-B
Ø1/8 PULL PIN X 5/16" L 202
2 PLCS
#4-40 FHCS X 5/16" L 103
2 PLCS
D
D
SECTION D-D
03
105 #8-32 LHCS X 5/16
6 PLCS, 3 PER SIDE
201 Ø1/8 PULL PIN X 1/4" L
2 PLCS
VIEW SHOWING UPPER COVER OFF
DRAWN BY E. SMALLWOOD 2/6/20
DESIGN ENG E. SMALLWOOD 2/6/20
APPROVED G. SHARMA 2/6/20
STRESS
PROJECT BOLT MODEL REWORK
FILE NAME
JOB NO. 19325-001
DO NOT SCALE DRAWING
SIZE E
TRI-MODELS, INC.
5191 OCEANUS DR
HUNTINGTON BEACH, CA 92649
TRI MODELS, INC.
PURDUE UNIVERSITY
BOLT MODEL REWORK
ASSEMBLY
PROJ NO. 6022
DRAWING NO. 19325001 1000
REV -
SCALE 1:1
SHEET 2 OF 3

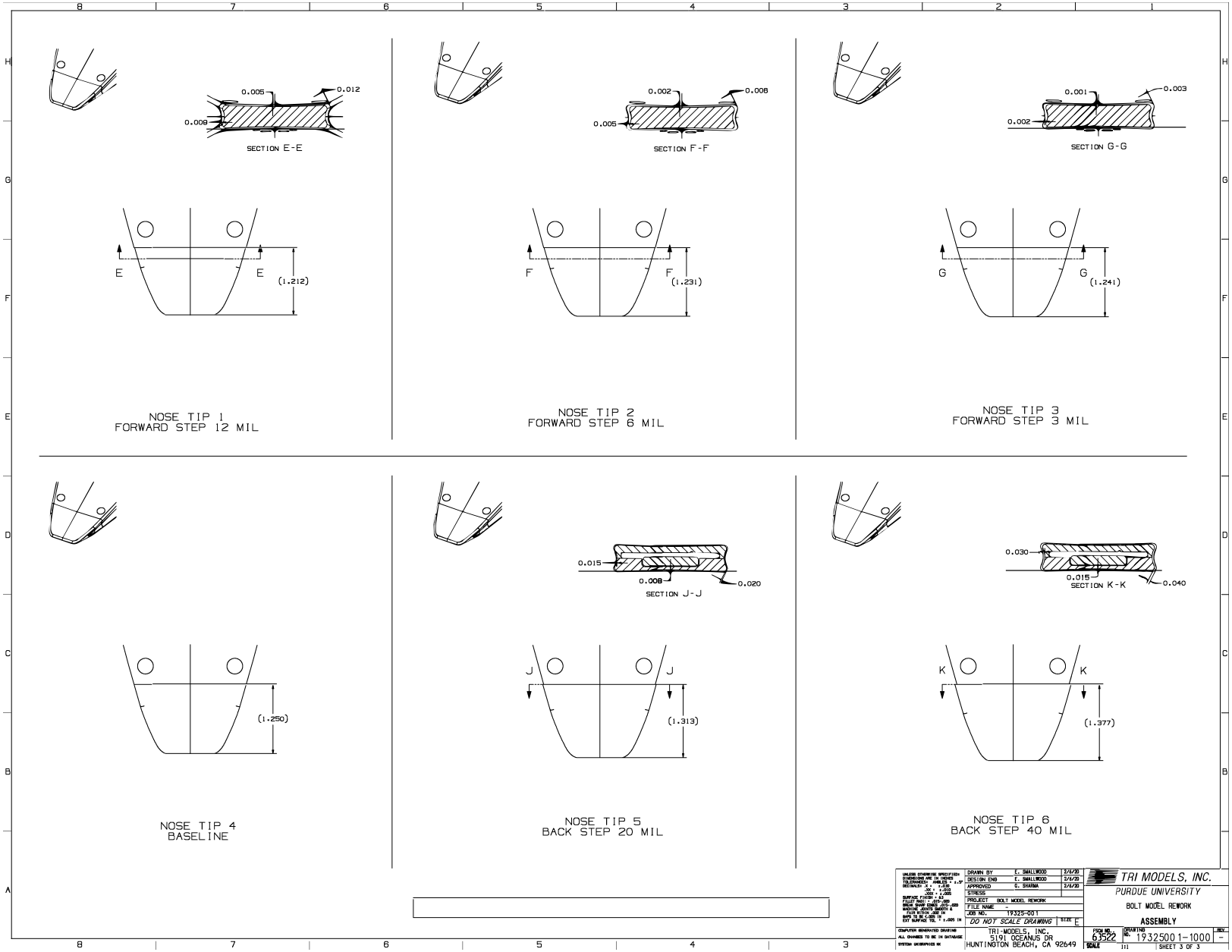
0.005
0.012
0.008
SECTION E-E
E
E
(1.212)
NOSE TIP 1
FORWARD STEP 12 MIL
0.002
0.008
0.005
SECTION F-F
F
F
(1.231)
NOSE TIP 2
FORWARD STEP 6 MIL
0.001
0.003
0.002
SECTION G-G
G
G
(1.241)
NOSE TIP 3
FORWARD STEP 3 MIL
(1.250)
NOSE TIP 4
BASELINE
0.015
0.008
0.020
SECTION J-J
J
J
(1.313)
NOSE TIP 5
BACK STEP 20 MIL
0.030
0.015
0.040
SECTION K-K
K
K
(1.377)
NOSE TIP 6
BACK STEP 40 MIL
DRAWN BY E. SMALLWOOD 3/6/20
DESIGN ENG E. SMALLWOOD 3/6/20
APPROVED C. SHANNA 3/6/20
STRESS
PROJECT BOLT MODEL REWORK
FILE NAME -
JOB NO. 19325-001
DO NOT SCALE DRAWING
SIZE E
TRI-MODELS, INC.
5191 OCEANUS DR
HUNTINGTON BEACH, CA 92649
TRI MODELS, INC.
PURDUE UNIVERSITY
BOLT MODEL REWORK
ASSEMBLY
PROJ NO. 6522
DRAWING NO. 1932500 1-1000
REV -
SCALE 1/1
SHEET 3 OF 3